Master thesis and internship[BR]- Master's thesis : Conceptual Design of the ATHENA X-IFU Dewar Entrance Assembly Hold-down and Release Mechanism[BR]- Integration internship

Auteur : Libert, Célestin
Promoteur(s) : Jacques, Lionel
Faculté : Faculté des Sciences appliquées
Diplôme : Master en ingénieur civil en aérospatiale, à finalité spécialisée en "aerospace engineering"
Année académique : 2024-2025
URI/URL : http://hdl.handle.net/2268.2/23383



Conceptual Design of the ATHENA X-IFU Dewar Entrance Assembly Hold-down and Release Mechanism

Libert Celestin

Thesis presented to obtain the degree of :
Master of Science in Aerospace Engineering

Thesis supervisor :
Jacques Lionel

Academic year: **2024 - 2025**

Acknowledgments

First of all, I would like to sincerely thank Prof. Lionel Jacques for his patience, availability, and valuable guidance throughout these past four months. I am truly grateful for the opportunity to work on this exciting project and to be welcomed into Guilhem's office during this period.

I would also like to thank Guilhem for his advices, patience, and kindness, as well as for all the knowledge he shared with me during my internship at CSL. I feel so grateful to all the people of the Centre Spatial de Liege for the welcoming atmosphere. Working in the thermo-mechanical team for the past four months have been an incredible experience.

Finally, I am deeply thankful to my family for their constant support, and to my friends for their encouragement and presence throughout this journey.

Abstract

This master thesis presents the conceptual design of the Hold-Down and Release Mechanism (HDRM) of the Dewar Entrance Assembly (DEA) door cryo-mechanism of the X-ray Integral Field Unit (X-IFU) aboard the ATHENA space observatory. The HDRM plays a critical role in ensuring the integrity of the cryostat during launch by maintaining vacuum tightness and thus protecting the ultra-thin filter that interfaces with the DEA.

A comprehensive design methodology was implemented, combining analytical modeling in *MATLAB* and numerical simulation using *SolidWorks* to assess the static equilibrium, actuation forces, and kinematic behavior of the HDRM. The Chebyshev four-bar linkage mechanism was selected based on heritage designs from the Herschel observatory, with adaptations to meet the specific kinematic and dimensional constraints. A parametric optimization process has been discussed and implemented to refine the HDRM configuration towards an optimal solution. Thermo-mechanical aspects were considered, and the main actuation requirements were established.

Preliminary finite element analysis and motion simulations were performed to confirm that the kinematic and dimensional requirements were met. Furthermore, experimental campaigns on candidate gasket materials were conducted to evaluate compression forces, leak tightness, and thermal behavior at cryogenic conditions using different samples from two suppliers.

The results demonstrate the feasibility of the proposed HDRM concept in meeting the mission's operational requirements. However, a discussion of the weaknesses and limitations of the conceptual design is also provided. This includes the need for further work on detailed actuator integration, the cryostat cover assembly design, structural integration, and alternative concepts that could be better suited for this application.

Keywords: ATHENA Mission, X-IFU, Space Mechanism Design, Cryogenic.

Contents

List of Figures

List of Tables

List of Acronyms

AIT Assembly, Integration and Testing

ATHENA Advanced Telescope for High Energy Astrophysics

BUNA Nitrile rubber

CAD Computer-Aided Design

CDAM Cover Door Assembly Mechanism

CLAES Cryogenic Limb Array Etalon Spectrometer

CNES Centre National Etudes Spatiale

CR Chloroprene

CSL Centre Spatial de Liege

CTE coefficient of thermal expansion

CTLE Coefficient of linear thermal expansion

CVV Cryostat Vacuum Vessel

DEA Dewar Entrance Assembly

DF Direct-formed

DN Nominal Diameter

ECSS European Cooperation for Space Standardization

EPDM Ethylene-propylene-diene rubber

ESA European Space Agency

FEM Finite element method

FKM Fluorocarbon

FUV Far-Ultraviolet

GA Genetic Algorithm

GAIA Global Astrometric Interferometer for Astrophysics

GSE Ground Support Equipment

HDRM Hold-on and Release Mechanism

HIFI Heterodyne Instrument for the Far Infrared

HOP High Output Paraffin

ICI Ice Cloud Imager

ISO International Organization for Standardization

ISO Infrared Space Observatory

JWST James Webb Space Telescope

LLD Launch Locking Devices

LN2 Liquid Nitrogen

MIRI Mid-InfraRed Instrument

MLI Multi-layer insulation

MWI Micro-Wave Imager

MXS Modulated X-ray Sources

NASA National Aeronautics and Space Administration

NBR Acrylonitrile-Butadiene

NEA Non-explosive Actuator

OSIRIS-REX Origins, Spectral Interpretation, Resource Identification, and Security Regolith Explore

PACS Photodetector Array Camera and Spectrometer

PTFE Polytetrafluoroethylene

REXIS REgolith X-ray Imaging Spectrometer

SIRTF Space Infrared Telescope Facility

SMA Shape Memory Alloy

SNA Separation nut actuator

SPIRE Spectral and Photometric Imaging REceiver

TES Transition Edge Sensors

UARS Upper Atmosphere Research Satellite

X-IFU X-ray Integral Field Unit

WFI Wide Field Imager

Introduction

The Advanced Telescope for High-ENergy Astrophysics (ATHENA) mission, part of ESA's Cosmic Vision 2015–2025 program, focuses on exploring the *Hot and Energetic Universe* theme. This space observatory aims to address key astrophysical questions, such as how ordinary matter assembles into large-scale cosmic structures and how black holes influence their surrounding environments. One of the two primary payloads at the heart of this mission is the X-ray Integral Field Unit (X-IFU), a high-resolution cryogenic imaging spectrometer that operates at extremely low temperatures (down to 50 mK). Encapsulated in a cryostat, the Dewar Entrance Assembly (DEA) incorporates a door cryo-mechanism designed to ensure the sealing of the cryostat and to protect an ultra-thin thermal filter from contaminants or particles that could damage or degrade its performance.

The door cryo-mechanism consists of two main parts: the cover assembly, which includes the door component that seals the cryostat, and the Hold-Down and Release Mechanism (HDRM), which provides sufficient force to lock the door during enclosure, vibration tests, and launch phases. The only comparable design to date is the Herschel cryostat cover mechanism, which utilized a Chebyshev four-bar linkage configuration compatible with the required kinematics imposed by the selected non-explosive separation actuators. However, no other known cover mechanism operates at such low temperatures, and detailed design information regarding the Herschel mechanism is limited. Consequently, the conceptual design of the DEA door cryo-mechanism—particularly the HDRM—is a challenging task. Numerous constraints must be satisfied to fulfill mission requirements, and the limited accessibility of the DEA within the instrument complicates the design by restricting the choice of actuators.

This challenging conceptual design process is presented throughout this thesis. Chapter 1 describes the mission context and design requirements. Chapter 2 provides an overview of main cover mechanism designs implemented in previous space missions and introduces other relevant mechanisms, highlighting the specific challenges associated with thermo-mechanical designs. Chapter 3 presents the initial design of the cover assembly, defines the HDRM-related design parameters used in the conceptual design, and reassesses key calculations, such as the required actuation torque. The core of this thesis begins with Chapter 4, which develops the parametric analytical model of the HDRM and discusses its validation. Chapter 5 covers the optimization process of the HDRM, including the selection of the optimization method and the final optimized configuration. Chapter 6 details the material selection for bearings and washers, presents preliminary thermo-mechanical tolerance calculations, and discusses the HDRM's actuation components.

Following this, Chapter 7 presents and discusses the current conceptual design, providing a preliminary motion analysis and a finite element method (FEM) study of the mechanism. Finally, Chapter 8 shifts focus from the HDRM design to present preliminary experimental tests performed on 40 mm nominal diameter (DN40) gaskets from different materials and suppliers. This experimental chapter lays the groundwork for future improvements of the cover design and verifies the order of magnitude of the compression force, which represents the dominant term in HDRM force characterization. A global conclusion and perspectives for future work are provided at the end of the thesis.

Objective

The objectives of this master's thesis are:

- Develop a hold-on and release mechanism (HDRM) conceptual design, more specifically:
  - Develop an analytical parametric model and validate it.
  - Perform a parametric optimization of the model.
  - Discuss the optimized configuration.
  - Select materials for the bearings and assess the contact stress, design the tolerance with respect to the thermo-mechanical constraints.
  - Present the final iteration and discuss the weaknesses and lacks of the provided design.
  - Propose a preliminary motion analysis and FEM study to ensure the mechanism fulfills the requirements.
- Assess preliminary computation for the cover assembly in prevision of the future design work to be made.
- Perform experimental tests on DN40 gaskets of different materials and discuss the experimental results.

Chapter 1

Mission Context

1.1 The ATHENA Mission

What are the cosmic processes that drive the assembly of ordinary matter into the large-scale structures we observe across the Universe? How do black holes grow, evolve, and influence their cosmic environment? These fundamental questions are part of the *Hot and Energetic Universe* theme of the primary scientific pillars guiding the European Space Agency's second large-class mission within its Cosmic Vision 2015–2025 program [14]. Space-based observations in the X-ray band is necessary to investigate these energetic phenomena since most baryonic component of the Universe is locked up in hot gas at temperatures of the million degrees order of magnitude, and because the extreme energetics of the processes close to the event horizon of black holes [15].

The ATHENA[1] mission proposal calls for spatially-resolved X-ray spectroscopy and deep wide-field X-ray spectral imaging with performance greatly exceeding the current observatories such as ESA's XMM-Newton spacecraft (launched in December 1999) [16], NASA's Chandra observatory (launched in July 1999) [17], or the Astro-H mission (launched in February 2016) [18].
The payload of the current design compromises three main elements [15]:

1. A single X-ray telescope with a focal length of 12 m and an effective area ($2\,m^2$ at 1 keV).
2. The X-ray Integral Field Unit (X-IFU), an advanced actively shielded X-ray micro-calorimeter spectrometer, using Transition Edge Sensors (TES) cooled at cryogenic temperatures (50 mK).
3. The Wide Field Imager (WFI), a Silicon Active Pixel Sensor camera with a large field of view, high count rate and moderate resolution spectrometric capabilities.

1.1.1 The X-IFU Instrument

The X-IFU is a cryogenic imaging spectrometer, providing spatially-resolved high-spectral resolution X-ray spectroscopy over a 5 arcminute equivalent diameter field of view [1].

The instrument is structured in a succession of bath temperature level to reach progressively the 50 mK. Figure 1.1 gives an overview of the actual configuration of the instrument, still currently being designed. Different V-groove radiators cool down the different levels of the instrument. Five filters restraints the incident photons energy to the targeted ones. The detectors are located within a cryostat cooled at 50 K.

The detection principle is based on the supra-conducting properties of the TES arrays cryo-cooled to

[1] Formerly since 2023, the mission have been rescoped to evolve into the *NewAthena* mission. However, through this report, the older mission name will be conserved for clarity.

50 mK. X-ray photons incident to the detector locally hit the surface of the array, which leads to an increase of the temperature. The raise of temperature is such that the supra-conduction property is locally lost, and it dissipates electricity. This loss is measured which permits to characterize the incident photon's energy [19].

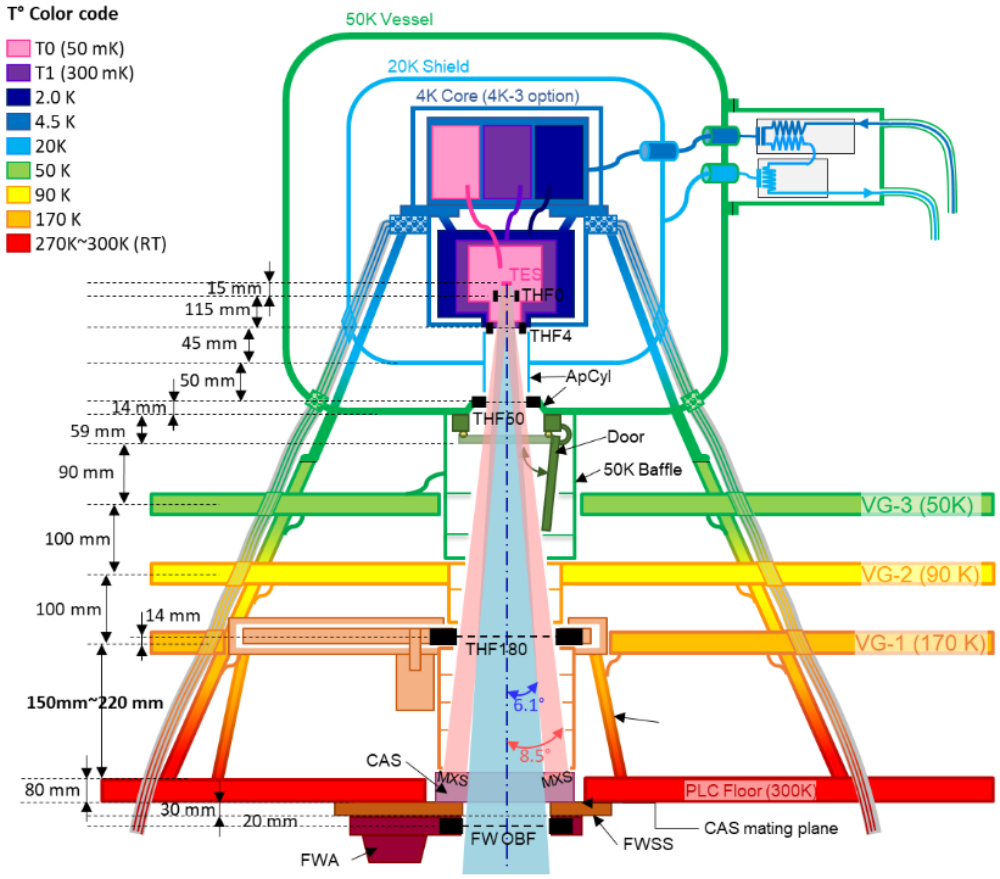

Figure 1.1: Dewar Entrance Assembly (DEA) localization within the X-IFU instrument environment [1].

1.1.2 The Dewar Entrance Assembly

The Dewar Entrance Assembly (DEA) is a contribution of Centre Spatial de Liege (CSL) and comprises a 50 K baffle, a cover assembly and its release mechanism, the 30 nm aluminum filter (THF50) and its carrier. The DEA outer shell is passively cooled at 50 K thanks to the V-grooves [20]. Figure 1.2 shows the computer-aided design (CAD) of the actual design configuration. For the external overview, the baffle component is hidden for clarity.

The ultra-thin layer of aluminum is supported by 45 nm of polyimide and the filter is reinforced mechanically by a hexagonal stainless steel mesh. Even if reinforced, the THF50 remains highly fragile and even steady air motion can damage it. The dewar will be launched under vacuum to solve this problem.

The dominant material in the DEA is aluminum, particularly on the filter carriers to match the material of the filters frames and of the rest of the dewar [21]. Since the temperature will vary significantly from room temperature at the beginning of the mission to cryogenic conditions for the science operations, all the component's dimensions will slightly decrease. The choice of almost uniform material composition of this subsystem aims to avoid thermal loads addition during this transition of temperature conditions.

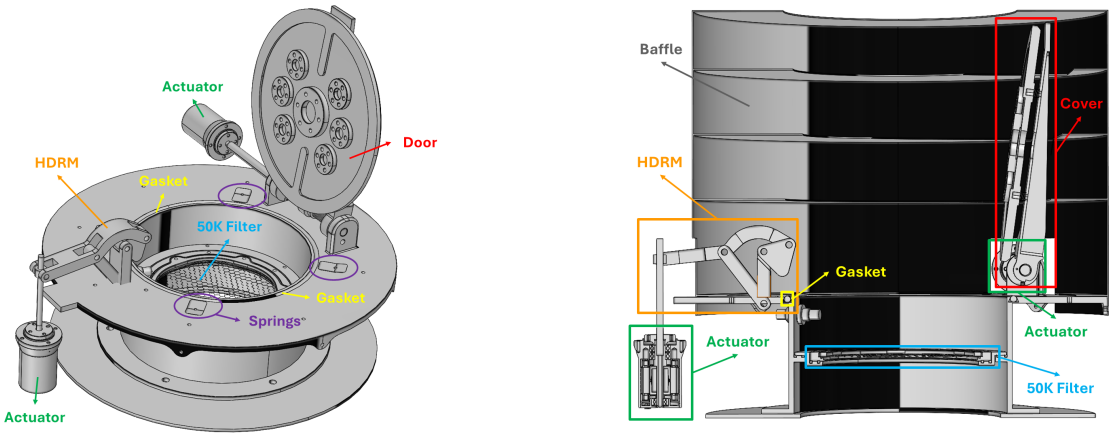

(a) External overview.

(b) Cut internal view.

Figure 1.2: Computer-aided design (CAD) of the actual DEA design configuration.

The dewar is launched under vacuum to protect the filter, meaning that the door has to be leak-tight at ambient temperature. The sealing is ensured thanks to a nominal diameter of 160 mm (DN160) gasket. Once in orbit, the dewar will first passively cool down before opening the door. The tightness is no more mandatory once the launch phase fulfilled. The cover assembly has to open in cold conditions, which means that the gasket may sticks to the door. This problem is counter-balanced by sheet springs located along the gasket circumference, but it adds another force to balance during the seal [20].

The cover accommodates a series of Berylium windows to enable X-ray transmission at high energy. One window is foreseen at the center plus six on the circumference for the three nominal and three redundant modulated X-ray sources (MXS) [20].

A hold-on and release mechanism (HDRM) is integrated to provide the required launch lock force to conserve the seal, and has a compliant kinematic to move out of the door opening motion trajectory. The actuation should be motorized due to the difficulty to access to the dewar once integrated to the entire instrument. The Chebyshev four-bar linkage family has been selected based on to the Herschel heritage [2]. The primary reason is that most actuators require linear motion, and this linkage family is designed to approximate such motion. Another reason is that the launch lock force required to maintain the compression rate of the seal, and guarantee the tightness of the cryostat, is important (around $1.5 \rightarrow 2.5$ kN). Motorized actuators for space application only deliver torques of the order of magnitude of 500 mN m, and providing an important torque for a continuous period of time would consume a lot of electrical power, and consequently dissipate a lot of heat in the vicinity of the DEA.

1.2 Scope of the Master Thesis

This master thesis project focuses on the design of the hold-on and release mechanism. Based on previous studies, the idea is to develop and optimize a design compliant with the current constraints and interfaces specified by the Centre National d'Etudes Spatiales (CNES). Analytical modeling of the mechanism using *MATLAB* as well as numerical modeling tools as *SolidWorks* will be employed. An experimental validation of the static forces of the mechanism using a breadboard design will also be provided to correlate the obtained results.

Additionally, since there are lots of uncertainties, experiment protocols will be discussed and developed. Particularly, the compression force of different joint material candidates (DN40 for these preliminary ex-

perimental tests) and leak rate will be evaluated.

Therefore, the following written report is presenting first the context of the mission and the problem characteristics. A state-of-the-art is provided to enforce the past challenges that similar design had to overcome. Then, preliminary calculation are detailed in Chapter 3 about the actual cover configuration presented before. The next chapters concerning the HDRM configuration are the core of the work achieved with the analytical code development in Chapter 4 with its validation, the optimization tool implementation in Chapter 5. After that, the conceptual design of the HDRM is detailed in Chapter 6 and preliminary analysis are presented in Chapter 7. Chapter 8 is slightly independent of the core of this report and presents the experimental tests sequence performed in parallel with the HDRM design activity. Finally, a conclusion and perspectives of future work are presented in Chapter 9.

1.3 Mission Phases

The mission phases of the DEA are following the conventional conduct of space mission. After the assembly of the instrument, the closing of the Dewar during the assembly, integration and testing (AIT) phase takes place, which includes vibratory tests, cryogenics thermal cycling tests and opening tests. Once the spacecraft has fulfilled the validation tests, the launch is considered (hot case), distinguishing the ascent phase close to sea level and the end, already in orbit. At this point of the mission, the dewar starts passively cooling down, until it reaches 50 K. Then starts the cruise phase until the Lagrange point L_2 orbit insertion. Once the final orbit established, the science operations starts. At this point of the mission, the release of the cover have already been completed (the release is the cold case) and the DEA is at 50 K. Figure 1.3 summarizes the mission phases with their temperature and pressure conditions[2].

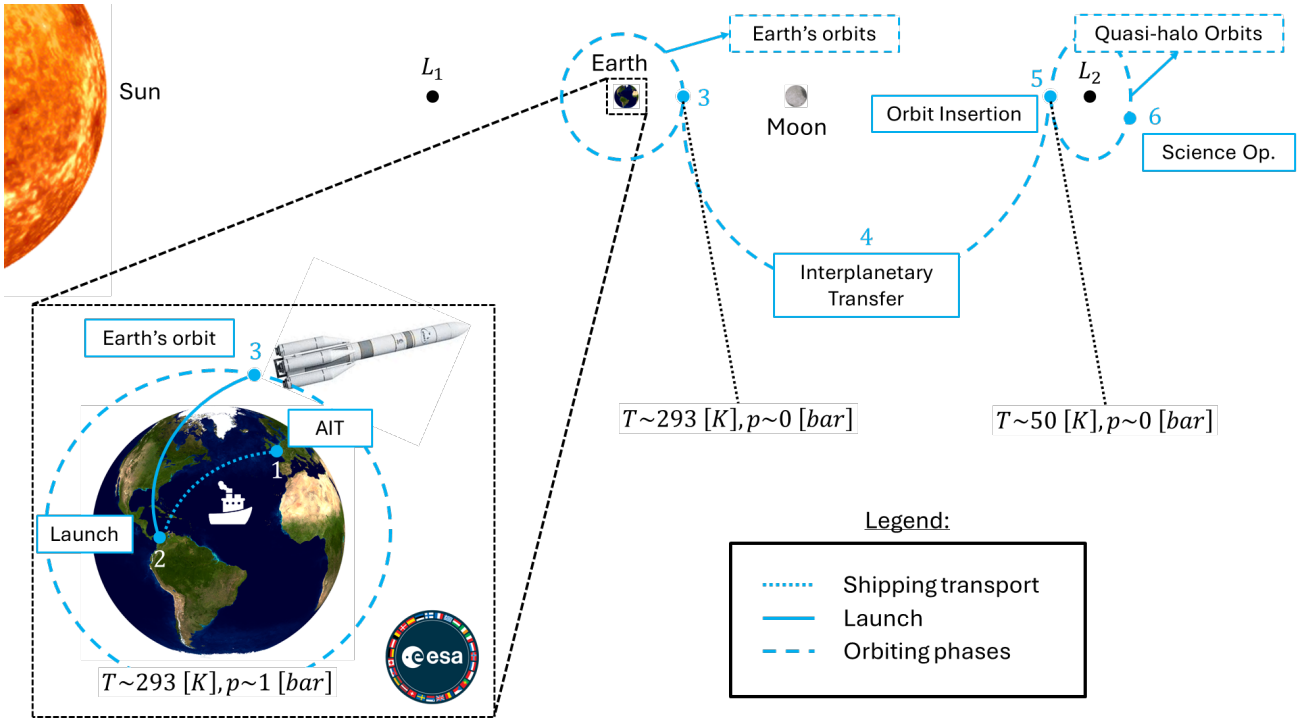

Figure 1.3: Mission phases and environmental conditions for the Dewar Entrance Assembly (DEA).

[2]The scale of the Solar System is not respected for clarity. The orbit trajectories are also qualitatively represented.

1.4 Requirements

The requirements are defined based on current preliminary definition of the X-IFU and Dewar, still under design. At this preliminary stage of the design, the interfaces between the DEA, the mechanism, the cryostat and the V-groove are not yet well-defined since the instrument is still currently being designed.

1.4.1 Functions

Since the 50 K filter is fragile enough to be damaged by any dust or particles, the main function of the door cryo-mechanism is the protection of the filter during the mission phase, including AIT. During the ground and launch phases, it shall maintain vacuum within the cryostat. Preventing air-leakage from outside is critical for the launch phase because of the fragility of the filter. A filter health check should be integrated to the cover assembly to detect any damage to the filter during AIT.

The door mechanism should also successfully open the cryostat cover. Since it is a single point failure for the instrument, high reliability is required. The validation by proof-of-concept and breadboard demonstrations should be provided to assess the design assembly is compliant to all requirements in every situation (including failure case).

1.4.2 Mechanical

The door mechanism interfaces with a base-plate interfacing with the 50 K Dewar, assumed to be in aluminum. It also possibly interfaces with the baffle for the open phase and/or during the release.

The mechanism should avoid any collision with any local part of the spacecraft and should not produce any particles that could damage the filter or degrade its performances. The mechanism should fit into a box of height that is maximum 55 mm below (bounded by the cryostat) the vertical location of the cover, and maximum 80 mm above (bounded by the V-groove). Figure 1.4 shows the different interfaces location with respect to the HDRM and the cover assembly within the DEA. The actuators selected should entirely fit within these dimension requirements. The restrictions are due to the cryostat and the V-groove components located around the DEA baffle. The aperture of the entrance is 150 mm in diameter.

The mechanism should be able to close again after release during ground testing. Actuated closing method should be preferred since the Dewar is not easy to reach within the whole instrument.

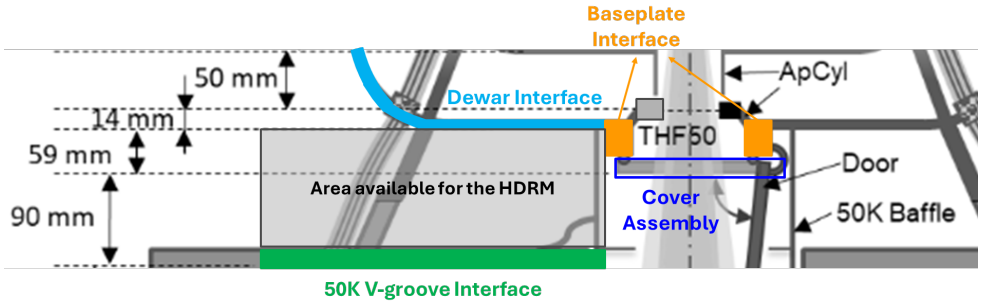

Figure 1.4: Overview of the dimensional constraints and interfaces with the DEA, based on Figure 1.1.

1.4.3 Thermal

The door mechanism should operate at 50 K at the release phases (during AIT and before science operations), and should minimize the heat losses through the cover.

The cooling is achieved passively from the end of the launch (Earth's orbit) to the end of the interplanetary transfer phase. The cryogenic tests performed during the AIT should reproduce the same cooling rate. The mechanism should maintain high reliability after thermal cycling. Backlash should be dimensioned appropriately to be compliant with both hot and cold case.

If the motorized actuation is selected, the mechanism should ensure that the overall thermal dissipation during actuation does not perturb the equilibrium of the Dewar. Conduction through electrical harness of the actuators, occurring over the whole mission lifetime and not only during actuation, should also be minimized.

1.4.4 Optical

The door mechanism should include a potential connection to filter health check Groung Support Equipment (GSE). There are not any sensors that are considered for this mechanism. The door also hosts Berylium filter for in-flight and on-ground calibration, even if the door is closed. When the door is open, the door and the mechanisms should not generate straylight.

1.5 Conclusion

The mechanism has two main state: closed (locked cover) and opened. The main design driver in terms of filter protection are the launch phase on ground (if there is a leak, all the filters would be broken) and the ground vibration tests performed during the AIT for which vibration levels are always higher due to margin. The main mission driver for the opening phase is the cryogenic testing phase because of gravity. This last driver is particularly challenging since the DEA is difficult to reach within the instrument. The cover requires to be closed after each release test, preferably without manual intervention.

Also, the thermal cycling is expected to be critical for the joint. In addition to the uncertainty due to the cryogenic temperatures, the cycling from room to cryogenic temperatures during the AIT phase may be problematic for the preservation of the sealing properties of the joint. Such uncertainties will require a lot of tests to assess the behavior of these component at such cold conditions considering that during the mission, there is only one cool down.

Chapter 2

State of the art

Along humanity's space journey, many spacecraft required door mechanisms that fulfills requirements such as contamination protection, vacuum sealing, etc. Even if these family of mechanisms is fairly common, the recent instrument requirements impose more complex constraints, such as operating at cryogenic temperatures or remaining within short dimensional bounds while resisting to high load magnitudes. And the designs of dewar door mechanisms operating at cryogenic temperatures are not common, and design details are rarely presented.

In this context, the state-of-the-art section will describe some relevant designs, or part of complete designs, that would be close to the characteristics, constraints and main challenges that will constitute the current conceptual design. More specifically, the section should detail several design features and highlight key aspects with respect to the DEA.

2.1 Dewar Door Mechanism Designs

2.1.1 Herschel Cryostat Cover Mechanism

The Herschel Space Observatory is an European Space Agency (ESA) mission launched the 14th May 2009 with the Planck observatory from Kourou. The spacecraft's science payload is constituted of 3 instruments:

- the Photodetector Array Camera and Spectrometer (PACS) instrument, a short wavelength camera and spectrometer (covering $55 \rightarrow 210\,\mu m$).
- the Spectral and Photometric Imaging REceiver (SPIRE) instrument, a long wavelength camera and spectrometer (two detector arrays covering $194 \rightarrow 325\,\mu m$ and $315 \rightarrow 672\,\mu m$).
- the Heterodyne Instrument for the Far Infrared (HIFI) instrument, a very high resolution heterodyne spectrometer.

Both PACS and SPIRE instruments are using bolometer detector arrays, which require a 300 mK cryogenic environment. This 'cold' part of the spacecraft is located inside a Cryostat Vacuum Vessel (CVV), enclosed by the Cryostat Cover Mechanism Assembly [22].

Cryostat Cover

The Cryostat Cover is maintaining high-vacuum inside the Cryostat at cryogenic temperature (70 K). It is a single point of failure for the mission. A conical 3 mm thick aluminum cover uniformly tightens the 300 mm o-ring Viton joint. Since the Viton sealing is deformed to 20% of compression set, support poles made of Vespel SP1 material to avoid metal-to-metal contact. Its upper area interfaces with a preload

lever (10 kN) by a ball bearing. Heat shield multi-layer insulation (MLI) with cooling loop are integrated to maintain the cover between 25 → 90 K and mitigate the parasitic heat load through the closed cover.

Then, 2 aluminum hinges support the cover via the lever in the closed configuration. The shaft material is stainless steel. 4 redundant torsional springs are used to provide the actuation torque required to release the cover. Moreover, to overcome a potential sticking of the joint on the cover surface, 4 titanium kick springs (around 462 N at 70 K each) equally distributed along the cover circumference are included.

Finally, a simple end stop device is included to slow down the release motion of the cover at the end of the opening. It has to be replaced after each release (successfully tested at 60 K) [2].

(a) Cover mechanism overview.

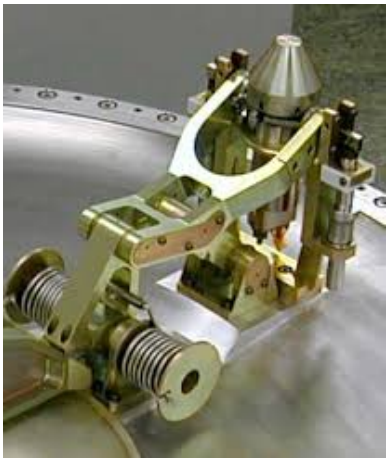

(b) HDRM overview.

Figure 2.1: Herschel cryostat cover mechanism overview, from Janu et al. [2].

Hold-On and Release Mechanism

The hold-on and release mechanism (HDRM) is a specific four-bar linkage compliant for the required kinematic, composed of 3 main pieces. The knee is a triangular piece in contact with the preload lever. It is equipped of a Teflon (PTFE) woven fiberglass liner at the contact interface to avoid cold welding. A lever piece interfaces with the knee, a straight leg piece and the separation nut. Due to the non-explosive actuators, the motion of the connection to the beam system requires a linear translational motion, parallel to the release bolt axis. The device was cryogenic compatible after application of some changes for this case:

- Most non-metallic materials were removed, because they broke under cryogenic conditions and produce debris;
- The shape of the threaded segments was adapted to avoid singular load peaks at the release campaign.

At the knee fixation, an additional hinge is included with 2 torque spring actuators to rotate the knee and permit the release of the cover. Vespel links are used to avoid metal to metal contact in bearings [2].

Non-pyrotechnic Separation Nut Actuators

The non-explosive separation nut actuator (SNA) has an internal thread divided into three movable segments. A bolt can be screwed into the thread, ensuring to provide an axial load of 42 kN. Once the

activation current has been applied, the separation nut disengages the segmented thread, which releases the preloaded bolt [23]. Since the actuator has operational temperatures between 123 and 403 K, which is not covering the cryogenic temperatures of Herschel mission, it had to be modified for cryogenic use, and was cryogenic compliant after some changes, as detailed earlier [2].

(a) External overview. (b) Cut internal view.

Figure 2.2: SNA device description, adapted from Galbiati et al. [3].

Already used for the ESA mission GAIA for example, Galbiati et al. [3] discusses the life testing activities of the Eaton 9421-1600-001 SNA, used on the Launch Locking Devices (LLD) of the Micro-Wave Imager (MWI) and the Ice Cloud Imager (ICI) instruments of the MetOp SG Satellite. According to Galbiati et al., the release event was always damaging the bolts during their release tests. The weakest part of the bolts threads material were plastically deformed due to the high load provided at the release. This expected behavior consequences to change the bolt after each release at 33 kN. In addition, due to the accumulation of deformation of other components of the actuator after several release tests, the pull out force capability was lowered to 40.5 kN instead of 42.2 kN (design value).

Vespel S-Line Materials

The DuPont Vespel SP materials are condensation type polyimide, with no observable glass transition temperature of melting point below a decomposition temperature (> 673 K). In common with most polymers, the materials exhibit anisotropy differences in properties, but machined parts from ISO shapes usually do not show this effect [12].

Direct-formed parts are produced with pressure applied unidirectionally, resulting in some anisotropy. The highest strength and elongation, and lowest thermal expansion are then found in the direction perpendicular to the pressing direction in most parts.

Different types of Vespel are provided by the manufacturer, corresponding to different applications [12]:

- The SP-1 is designed for mechanical and electrical parts at elevated temperatures (typically for valve seats, seal, insulators, etc). It was used for the seal contact of the cover of the Herschel mission [2].
- The SP-21 is well-adapted for lubricated or non-lubricated, low friction and wear applications (typically for valve seats, seals, bearings, washers, seal rings, etc). The graphite it contains ensure long term thermal stability.
- The SP-22 is used where low thermal expansion is more important than strength (typically for bearings, washers, etc).

- The SP-211 is also well-adapted for low friction and wear applications (typically for bearings, washers, etc). It has the lowest static friction.
- The SP-3 is designed for friction and wear applications in vacuum or inert gases (typically for bearings, piston rings and seals).
- The SP-2515 is used for wear against aluminum. It has a lowe coefficient of friction in dry environments. Its low coefficient of thermal expansion is low and matches the aluminum one.

2.1.2 CLAES Instrument Aperture Door Mechanism

The Cryogenic Limb Array Etalon Spectrometer (CLAES) is one of a complement of instruments on the NASA Upper Atmosphere Research Satellite (UARS) which will study atomospheric photochemistry, energy input, and dynamics following a 1991 launch. This mission has to collect stratospheric sciences data, while the CLAES instrument specifically measures infrared signatures of gas traces from 10 to 60 km above the Earth [24].

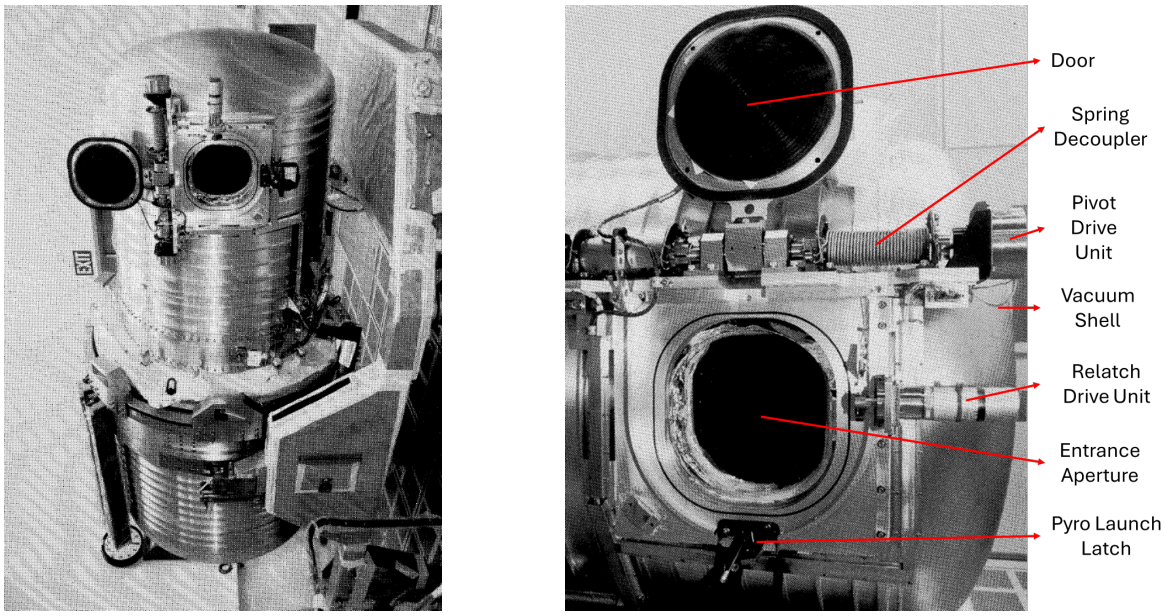

(a) Instrument overview. (b) Door mechanism overview.

Figure 2.3: Overview of the CLAES instrument, reproduced from Stubbs [4].

The instrument is an assembly of two major components: the instrument package and the cryostat, which maintains the instrument package under cryogenic conditions. Operating at 185 K, the door assembly is constituted of a blackbody calibration source assembly, pivot mechanism, hinge bearing assembly, launch latch mechanism, door stop assembly and re-latch mechanism. The door is machined out of a solid block of 6061-T651 aluminum, coated with Magnaplate HCR at the sealing surface, which is a surface enhancement coating that improves the corrosion resistance and the hardness of aluminum and aluminum alloys [25]. This coating is used to prevent sticking of the Viton O-ring seal (hardening and lubricating aluminum surfaces).

The heart of the door mechanism is the redundant pivot mechanism, which consists of duplicate drive trains connected to opposing ends of the door hinge shaft. Both trains are composed of a drive unit (integral two degree stepper motor with 100:1 harmonic drive and a helical spring decoupler). The sleeve

bearing are made of DuPont Vespel SP-3, ensuring low outgassing and low friction coefficient. As a redundant feature of the mechanism, in case of total failure of the drive components, firing the pyro launch latch will allow the spring decouplers to automatically open the door. This requires a door stop assembly in that case to ensure the cover will stop without damaging its surroundings [4].

2.2 Review of Similar Space Mechanisms

2.2.1 Space Infrared Telescope Facility (SIRTF)

The Space Infrared Telescope Facility (SIRTF) is a deep-space Sun orbiting observatory that features a 0.85 m aperture telescope at 5.5 K, and 3 science instruments with focal plane detectors cooled to 1.5 K. To achieve such cryogenic temperature, a cryostat encloses the instruments. The aperture door provides a vacuum seal and is constituted of a gold-coated window to enable short wavelength end-to-end optical testing prior to launch [26]. This single shot mechanism operates between 105-210 K. The design had to operate over a wide range of temperature, even at room temperature for the initial acceptance tests. The material had to carefully be selected to match the coefficients of thermal expansions. In addition, the door have to maintain seal over 18 months of system testing prior to launch and must reseal after thermal cycling without external adjustments. Series of deployments at 95 K have been performed successfully. A light-tight photon shutter is located between the aperture and the instrument to minimize the parasitic heat load through the aperture [27].

2.2.2 Infrared Space Observatory (ISO) Spacecraft

The Infrared Space Observatory (ISO) essentially consists of a large liquid-helium cryostat, a telescope with a 60 cm diameter primary mirror and four scientific instruments. A cover closes the cryostat on the ground and is constituted of two windows which transmit visible radiation. To support instrument testing, the cover carries an infrared source which can irradiate the instruments. Additionally, the cover's innermost radiation shield can be cooled below 5 K with a liquid-helium flush, providing a low thermal radiation background. Secured by a clampband, it would be ejected about 14 days after the launch, when the spacecraft outgassed sufficiently [28].

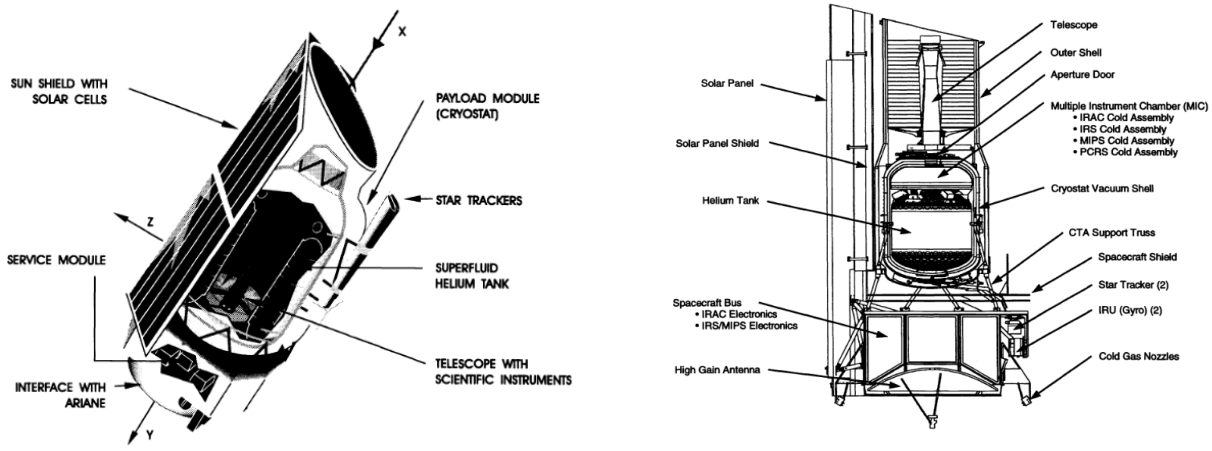

(a) ISO Spacecraft [28]. (b) SIRTF Spacecraft [27].

Figure 2.4: Overview of the ISO and SIRTF spacecraft.

2.2.3 REgolith X-ray Imaging Spectrometer (REXIS) Deployable Radiation Cover

The REgolith X-ray Imaging Spectrometer (REXIS) is a student collaboration in the context of NASA New Frontier mission which aboard the Origins, Spectral Interpretation, Resource Identification, and Security Regolith Explorer (OSIRIS-REX) spacecraft. The instrument contains a one-time deployable radiation cover that opens using the TiNi EBAD's Frangibolt, a shape memory alloy actuator, with two torsion springs. The actuator is constituted of CuAlNi shape memory alloy cylinder that provides around 2.45 kN of force to fracture the fastener in tension during actuation. The mechanism rotates about Vespel SP-3 bushings. Poron 4701-40 bumper tabs are included to reduce the impact of the door opening [29].

Shape Memory Alloy (SMA) Actuator

Many release mechanisms are being designed using the shape-memory alloy Nitinol, which is an alloy comprised primarily of nickel and titanium [30]. The principal behavior of such materials is that they return to the same shape each time they are heated above a certain temperature, referred to as their transition temperature. The increase of temperature produces an elongation which provide the actuation force [31].

The most commonly used Nitinol-based release mechanism, like TiNi Aerospace's Frangibolt used in the REXIS mechanism, is the Frangibolt, which uses a precompressed Nitinol cylinder elongating upon heating. This stretches a bolt until it fails in tension [32]. This actuator family device can support and release loads from 3.78 kN to 116.5 kN [33]. Its operational temperature is 208 K to 353 K [34]. Typically, it consumes around 10 to 30 W [35]. Finally, the actuation time depends on the supply voltage and its initial temperature [31].

2.2.4 ALICE Enclosure Entrance Assembly

ALICE is a lightweight, low-power, and low-cost imaging spectrograph optimized for cometary far-ultraviolet (FUV) spectroscopy. The double-delay line detector is enclosed in a vacuum chamber with a front door that was successfully and permanently opened during the early commissioning phases of the mission flight. The entrance assembly is constituted of a door release mechanism, torsion spring released by a dual-redundant pyrotechnic actuator. The front door has to maintain vacuum within the detector chamber ($< 10^5$ Torr) and to protect the detector from contamination. During instrument integration and test, the door was successfully released numerous times and manually reset. In addition, a built-in MgF_2 window port that transmits UV light (> 1200 Å). The window is used to test the detector while the door is closed, and constitutes also a redundancy solution in case of failure of the opening [36].

2.2.5 MIRI Contamination Control Cover

The James Webb Space Telescope (JWST), launched in December 2021, is constituted of four scientific instruments, including the Mid-InfraRed Instrument (MIRI). This instrument has been equipped with a contamination control cover, operating at cryogenic temperatures (7 [K]). The cover has to protect the instrument against external particular or molecular contamination and during coronographic observation. Even if the function of the cover is different from the cover mechanism to be designed, the actuator and its associated gearbox are particularly relevant to present since they were supposed to work under cryogenic conditions [37].

The cover opening is performed by one of the two independent 2-phase stepper motors from CDA Intercorp. The duration of the opening is around one minute. As the cover represents a single point of failure, it has been designed to be one failure tolerant, explaining the redundancy of the stepper motor actuators. The gearbox that equips the 2-phase stepper motors from CDA Intercorp has a gear ratio of $100:1$. Since the instrument operates at cryogenic temperatures, the thermal losses due to the motorized actuation

needed to be minimized. The gearbox design permits to decrease significantly the current and the voltage required to actuate the cover and mitigate thermal dissipation [37].

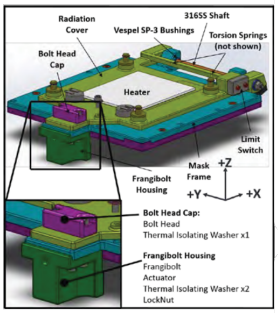

(a) REXIS cover mechanism [29].

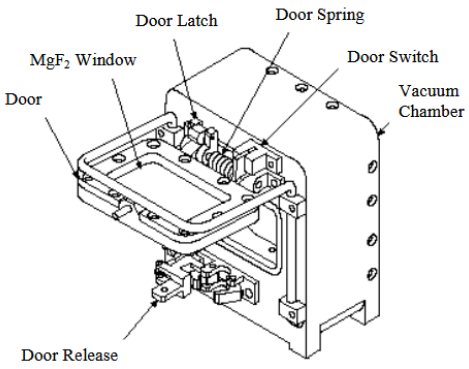

(b) ALICE cover mechanism [36].

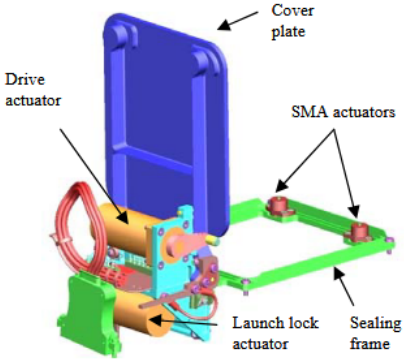

(c) MIRI cover mechanism [37].

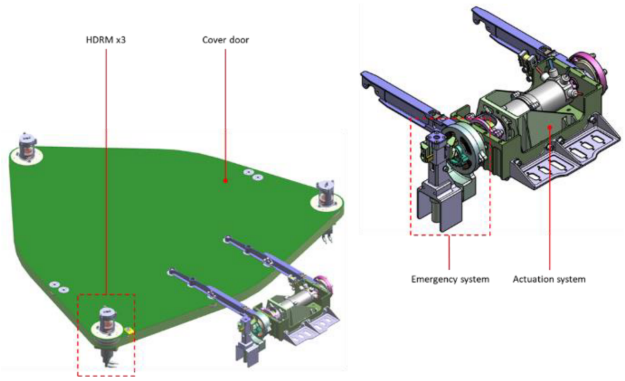

(d) CDAM [38].

Figure 2.5: Various cover mechanism overviews.

2.2.6 Space Telescope Actuated Door Mechanism

The main objective of the novel Cover Door Assembly Mechanism (CDAM) designed, manufactured and qualified by OHB Italia is the protection of the instrument against sunlight, and mitigate the contamination from dust particles during the AIT and storage phases. The 1 m diameter cover door is rotated by a stepper gear motor from Phytron GmbH for 270 deg. The stepper motor is equipped with a 200:1 harmonic drive.

The HDRM is constituted of 3 separation nuts from Cooper Interconnect with conic shape contact area. Sensors are included to assert the open and closed phase configurations of the cover, and 2 redundant potentiometers are provided to measure the intermediate angular positions. An emergency opening system is also included in case of motorized actuator failure. When activated, a High Output Paraffin (HOP) actuator piston compresses its spring and moves an unhook pin. It gradually releases the torsion spring in a controlled, step-by-step motion through a toothed mechanism. This rotation applies torque to the door panel, forcing it open permanently. The system first decouples the gearmotor using an unhook lever released at the same time as the HOP actuator expansion. This prevent the jammed reduced from resistive spring motion [38].

PhySpace Stepper Motor

The Phytron PhySpace motor represents a standard stepper motor series for space applications. Already used in numerous space applications such as Juno for the mirror rotation in Ultraviolet Imaging Spectrograph, BepiColombo with the MERTIS instrument or the EnMAP mission. The motor series provide stepper motor from 3.8 mN m to 500 mN m of holding torque for the biggest actuator model. Customizations such as tailored gearbox, cryogenics compliance (up to 4 K) or lightweight upgrade are possible by contacting directly Phytron GmbH [39].

High Output Paraffin (HOP) Actuators

High Output Paraffin (HOP) Actuators use constrained volumetric expansion of a highly refined polymer at a specific transition temperature to produce large hydrostatic pressure and deliver actuation force. The polymer can be varied to change actuation temperature [40].

HOP actuators have been used in a wide variety of applications, typically launch restraints, cover opening systems, etc. Current paraffin formulations have operational temperature from 278 to 373 K, but it depends on the polymer used [34, 41]. Tibbitts' paper test results [42] indicate that HOP thermal actuators are appropriate for utilization in adaptive systems requiring high displacement, accurate positioning within a control bandwidth of 5 Hz or less. Typical power consumption ranges from 5 to 20 W, mass between 35 and 100 g and an actuation force from 0.022 to 1.55 kN [41]. Paraffin actuators usually take 30 s or more to achieve full actuation. This actuation time is dependent on the supply voltage and its initial temperature, just like SMA actuators [31].

2.3 Summary and Conclusion

Regarding the literature, even if numerous cryostats have been already designed for many different space applications from Earth's atmosphere characterization to space observatories, the designs of door cryomechanism at cryogenic temperatures around 50 K are rare.

Since every space mechanism induces risks of critical failure for the mission, or for the operability of some instruments, solution that required no mechanism were often preferred especially earlier as it was the case for the ISO mission. Some mission like the REXIS cover or the SIRTF mission contained a relevant design but were operating under hotter cryogenic conditions. Other designs had a completely different objective like it was the case for the cover of the MIRI instrument, which aimed to protect the detector from contamination, requiring cold surface temperature to facilitate the adhesion of moisture. The necessity to design instruments that measures under colder cryogenic conditions is recently possible, like it have been the case for the Herschel cryostat cover mechanism design. However, available design information about this cover mechanism was very limited.

Regarding the material selection of similar past missions, anodized aluminum is widely used for its lightweight and its mechanical properties. The fact that the materials retract significantly at such temperatures impose some constraints on the other selection of materials. The Vespel S-line materials are widely used for the bearings, even for earlier mission such as CLAES. The Viton material used for the O-ring seal in the Herschel requires some investigation due to lack of data.

Considering now the actuators, Figures 2.6 shows examples of some actuators presented through this entire chapter. Table 2.1 compares 5 family of relevant actuators in terms of mass, shock level, reusability, cryogenics compliance and power required. This non-exhaustive table provides a rough idea of the order of magnitude of major features of the devices considered. HOP actuator principle is complex to adapt to cryogenic conditions since it would require to have a polymer that could provide the volumetric

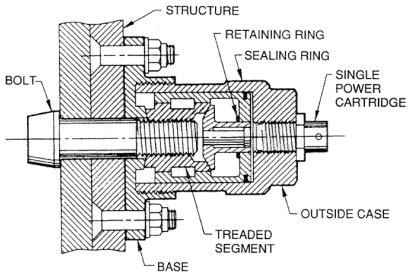

(a) Pyrotechnic separation nut [40].

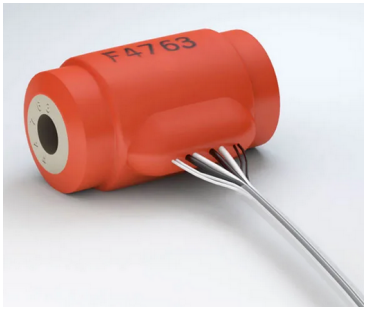

(b) TiNi SMA [35].

(c) PhySpace Motor [39].

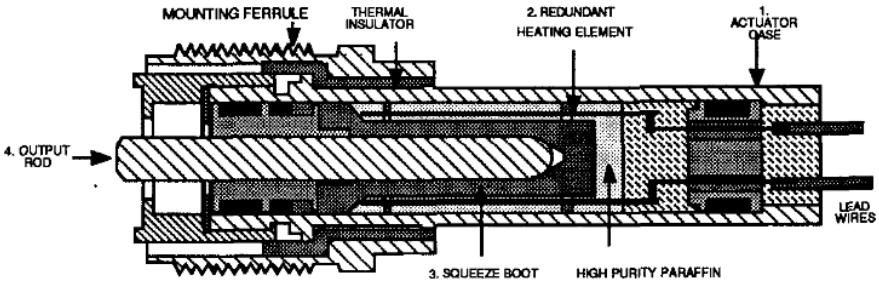

(d) HOP actuator [41].

Figure 2.6: Various actuator families overview.

expansion in very cold conditions, where usually almost every polymeric materials become brittle [43]. Pyrotechnic actuators require almost no power and are lightweight component, but the release is violent and may produce debris [31]. The SMA actuators are interesting but require more power to generate the heat and permit to reach the actuation force required. A manual intervention using the associated reset tool is necessary between each use. The non-explosive actuator were used on Herschel's design. After some changes, the device was compliant with cryogenic temperatures. However, it requires manual intervention to reset the device since it's a one-shot actuators. Finally, the motorized actuators (stepper motor considered only here) are heavy components and consume significant amount of power, but it depends on the acceleration profile shape and the current applied. Gearbox can be used to decouple the torque delivered, typically around 100 or 200:1 ratio actually. However, the power consumed will drive the size of the electrical cables, and would be critical for the thermal equilibrium since the cables constitutes a thermal bridge from a hotter part of the spacecraft. The time of actuation during which the heat produced continuously is also critical to quantify because the energy dissipated will perturb the thermal equilibrium of the surroundings.

	SMA [31, 35]	**HOP** [31, 41]	**Pyrotechnic** [31, 40]	**NEA** [3]	**Motorized** [39]
Mass [kg]	< 0.20	< 0.15	< 0.10	< 0.25	> 0.50
Shock Level	Very low	Low	High	Medium	Very low
Reusability	Yes	No	No	No	Yes
Cryo-compatible	Possible	No	Possible	Yes	Yes
Power [W]	$\sim 10 \rightarrow 30$	$\sim 5 \rightarrow 20$	~ 0	~ 0	$\sim 2 \rightarrow 10$
Actuation Time [s]	$\sim 8 \rightarrow 15$	> 30	< 0.01	< 0.025	> 1

Table 2.1: Comparative table for different families of actuators.

To conclude, the main relevant design of cover cryo-mechanism is the Herschel door mechanism design. Other relevant designs such as the CLAES mission, the SIRTF telescope or the ISO spacecraft are presented for the similarity of their application, even if the operating temperatures are not the same. Some other mechanisms are also presented such as the ALICE enclosure entrance mechanism, the MIRI cover mechanism, the REXIS instrument or the Space Telescope Actuated Door because of the relevance of small part of their constituting components, or to better understand the challenges and design choice of cover assembly more generally.

It outcomes that redundancy of such design is critical to maximize the robustness of the space mechanism design. Many validation and compliance tests for every single component included to minimize the risk of complete failure of the design. In addition, since there are a lot of uncertainties on the sealing joints, experimental test sequences will be required to clarify the behavior of different joint materials at cryogenic conditions.

Chapter 3

Cryostat Cover Preliminary Design

The cryostat cover assembly detailed design is not in the scope of this master thesis. However, since the HDRM design is driven by the dimensions of each component of the cover, the kinematic of the assembly and the static equilibrium, this first section aims to detail the actual status of the cover assembly design and derive the driving features that will be used to design the HDRM. In addition, some preliminary computation concerning the actuation force, the actuator choice and acceleration profile, and the heat generation during the actuation phase will be also assessed to identify the major challenges that will be encountered for the future design optimization of this part of the DEA.

3.1 Cover Assembly Actual Design

The actual configuration of the cover assembly is considered from the CAD model presented in Figure 1.2. The dimensions and the mass properties (including the mass moment of inertia) are computed using *SolidWorks*.

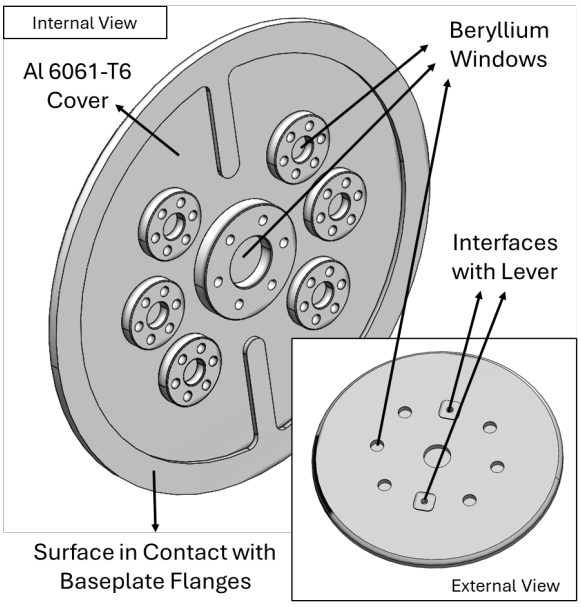

(a) Door actual design.

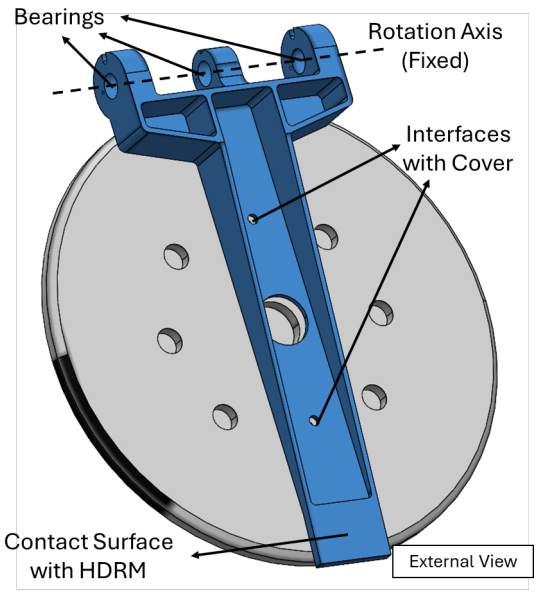

(b) Lever actual design.

Figure 3.1: Actual configuration of the cover assembly, based on the CAD model presented in Figure 1.2.

3.1.1 Door

The actual door design, represented in Figure 3.1, is a flat disk composed of 7 Beryllium windows used to check the filter health during the AIT. The outer surface of the disk will be in contact with the flange (will act as an end stop for the compression) of the baseplate in closed configuration. The DN160 gasket will therefore be compressed inside its groove, pushing against the door. The door is 177 mm in diameter and it overall mass is actually evaluated to 0.202 kg.

3.1.2 Compression Springs

The compression springs have the function to ensure the sealing force provided is uniformly distributed on the cover circumference. They should be located at the interface between the cover and the lever. The current configuration is not yet including that part of the design and remains as a part of the future work to be achieved.

3.1.3 Lever

The actual lever design, represented in Figure 3.1, is a complex shape beam that links the actuation shaft located along the rotation axis with the door that seals the cryostat. It interfaces also with the HDRM during the launch lock, in contact at its tip. The lever is 190 mm long, 30 mm wide and its overall mass is actually evaluated to 0.037 kg.

3.1.4 DN160 Gasket

The gasket's behavior is not well characterized due to lack of documentation, especially at cryogenic conditions. Its constitutive material should be carefully selected in order to be compliant with the AIT cycling test sequence. For this reason, preliminary experimental tests will be performed and presented to evaluate the compression force of the gasket and its leak performances before and after exposure to cryogenic conditions. Tests set-up description and results are discussed in Chapter 8.

At this stage of the design, the gasket is assumed to be made in Viton (fluorocarbon material) as it was the material selected for the Herschel door cryo-mechanism design [2]. Assuming a target compression rate of 20%, the compression force range for a 70 Shore hardness extends between 1.75 and 7 $\mathrm{N\,mm^{-1}}$ [10]. Due to high uncertainties, the resistance of the joint is firstly considered at 7 $\mathrm{N\,mm^{-1}}$ and will be better characterized by experimental measures.

3.1.5 Safety Opening Devices

Some adhesion of the gasket could be observed at cryogenic conditions. The actual design includes 4 spring sheets distributed along the door circumference to compensate this. Due to high uncertainty, the design of such springs has to be investigated after better characterization of this adhesion phenomena. Alternative to kick springs design should be investigated, like passive components that could have a smaller coefficient of thermal expansion (CTE) than the aluminum, in order to provide a kick-out force only under cryogenic conditions. This remains also as a part of the future work to be achieved.

3.2 Static Equilibrium

The static equilibrium aims to compute the HDRM force required to maintain the tightness of the door against the gasket. It is also used to evaluate the reaction force at the shaft location in order to assess the bearing material will not deform plastically. It is derived in 2 steps: first, the static equilibrium is

computed on the door only to compute the seal force that should be transmitted by the lever; then, the static equilibrium is computed on the lever to compute the HDRM force.

3.2.1 Door

The mission phase that will drive the design is the enclosure during the AIT phase. Indeed, the cover mechanism has to provide the compression force required without the pressure gradient helping to tighten the gasket. The forces involved for the door are the followings:

- The gravity of the entire cover assembly, $\vec{F}_g$;
- The pressure force due to vacuum inside the cryostat, $\vec{F}_p$;
- The vibration force, $\vec{F}_{vib}$[1];
- The gasket reaction force due to compression, $\vec{F}_{j,cp}$;
- The gasket adhesion force (only under cryogenic conditions), $\vec{F}_{j,ad}$;
- A potential kick-springs force (depending on the design choice), $\vec{F}_{ks}$.

Figure 3.2 shows graphically the static equilibrium assessed on the door component. The sealing force $\vec{F}_s$ is the force applied from the lever that should compensate the other forces.

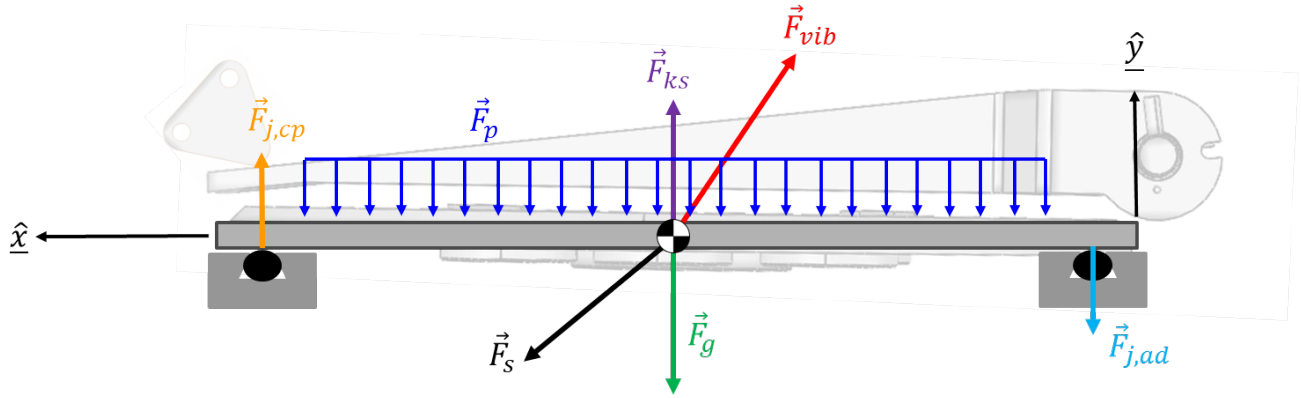

Figure 3.2: Static equilibrium schematic of the door, part of the cover assembly.

Since the driving phase is the enclosure during the AIT phase, the cover mechanism operates at room temperature, meaning that no adhesion force should be considered nor vibration forces. The kick-spring components still require to be designed consistently, and some alternatives should be investigated. It is assumed that the device only compensate the cryogenic adhesion of the gasket at cryogenic conditions and not at room temperature. Therefore, the kick-springs force can be assumed to be 0. Finally, the worst case that could happen during the AIT is the enclosure of the cryostat since the mechanism should tighten the gasket without the help of the pressure gradient due to vacuum. The gravity for these computation is assumed to be positive (oriented upward and not downward). That being said, the static equilibrium over the door is expressed as follows:

$$\begin{aligned} F_{s,x} &= 0 \\ F_{s,y} &= F_{j,cp} + F_g \end{aligned} \tag{3.1}$$

[1]Due to margins, the vibration force should be more important than what the cover assembly will be subjected to during the launch. The vibration force level is provided by preliminary analysis made by the CNES and equals $F_{vib,y} = F_{vib,x} = 30 \cdot g = 0.294\,\text{kN}$ where $g = 9.81\,\text{m}\,\text{s}^{-2}$ is the Earth's gravity acceleration.

The gravity force of the entire cover assembly is computed according to the CAD model values provided earlier and equals $F_g = m \cdot g = 2.34\,\text{N}$ where $m = 0.239\,\text{kg}$ is the mass of the door and the lever.

Considering now the gasket reaction force to the compression, the gasket behavior is not well characterized. As a first approximation, Viton joint (fluorocarbon material) is considered as it was the gasket selected for the Herschel mission [2]. Assuming a target compression rate of 20%, the compression force range for a 70 Shore hardness extends between 1.75 and $7\,\text{N}\,\text{mm}^{-1}$ [10]. Due to high uncertainties, the resistance of the gasket is firstly considered at $R_{FKM} \approx 7\,\text{N}\,\text{mm}^{-1}$ and should be better characterized by experimental measures. The gasket reaction force is therefore estimated by $F_{j,cp} \approx \pi D_{FKM} \cdot R_{FKM} = 3.52\,\text{kN}$ where $D_{FKM} = 160\,\text{mm}$ is the nominal diameter of the gasket.

The static equilibrium becomes:

$$\begin{aligned} F_{s,x} &= 0\,\text{kN} \\ F_{s,y} &= F_{j,cp} + F_g = 3.53\,\text{kN} \end{aligned} \tag{3.2}$$

3.2.2 Lever

The static equilibrium of the lever will be derived similarly, considering the torque equilibrium to compute the HDRM force, and the net forces to compute the shaft reaction force. Figure 3.3 shows graphically the static equilibrium assessed on the lever component. The forces involved for the lever are the followings:

- The gravity of the entire cover assembly, $\vec{F}_g$;
- The vibration force, $\vec{F}_{vib}$;
- The shaft reaction force, $\vec{F}_{shaft}$;
- The seal force applied on the door, $\vec{F}_s$;
- The HDRM force applied at the tip of the lever, $\vec{F}_{hdrm}$.

Evaluated with *SolidWorks*, the distance $x_d = 177\,\text{mm}$ is the door diameter, $x_{hdrm} = 10\,\text{mm}$ is the distance of contact between the HDRM and the lever, $x_{shaft} = 6.68\,\text{mm}$ (the center of the door is located 95.18 mm away from the shaft center axis) and the overall length of the lever is equal to $L = 190\,\text{mm}$.

Assuming that the HDRM force is applied vertically and considering the gravity as positive force (head downward orientation), the static torque equilibrium is computed as follows[2], considering the shaft as rotation point (fixed):

$$\frac{L}{2} \cdot F_{vib,y} + \left(x_{shaft} + \frac{x_d}{2}\right) \cdot F_{s,y} + \frac{L}{2} \cdot F_g - (L - x_{hdrm}) \cdot F_{hdrm,y} = 0 \tag{3.3}$$

The HDRM force is finally computed by rearranging Equation 3.3 as follows:

$$F_{hdrm,y} = \frac{\frac{L}{2} \cdot F_{vib,y} + \left(x_{shaft} + \frac{x_d}{2}\right) \cdot F_{s,y} + \frac{L}{2} \cdot F_g}{(L - x_{hdrm})} = 2.02\,\text{kN} \tag{3.4}$$

The static equilibrium (net forces) over the lever is expressed as follows:

$$\begin{aligned} F_{shaft,x} &= F_{s,x} = 0\,\text{kN} \\ F_{shaft,y} &= F_{s,y} + F_g - F_{hdrm,y} = 1.51\,\text{kN} \end{aligned} \tag{3.5}$$

[2]The sign convention used for the torque equilibrium defines positive torques anticlockwise.

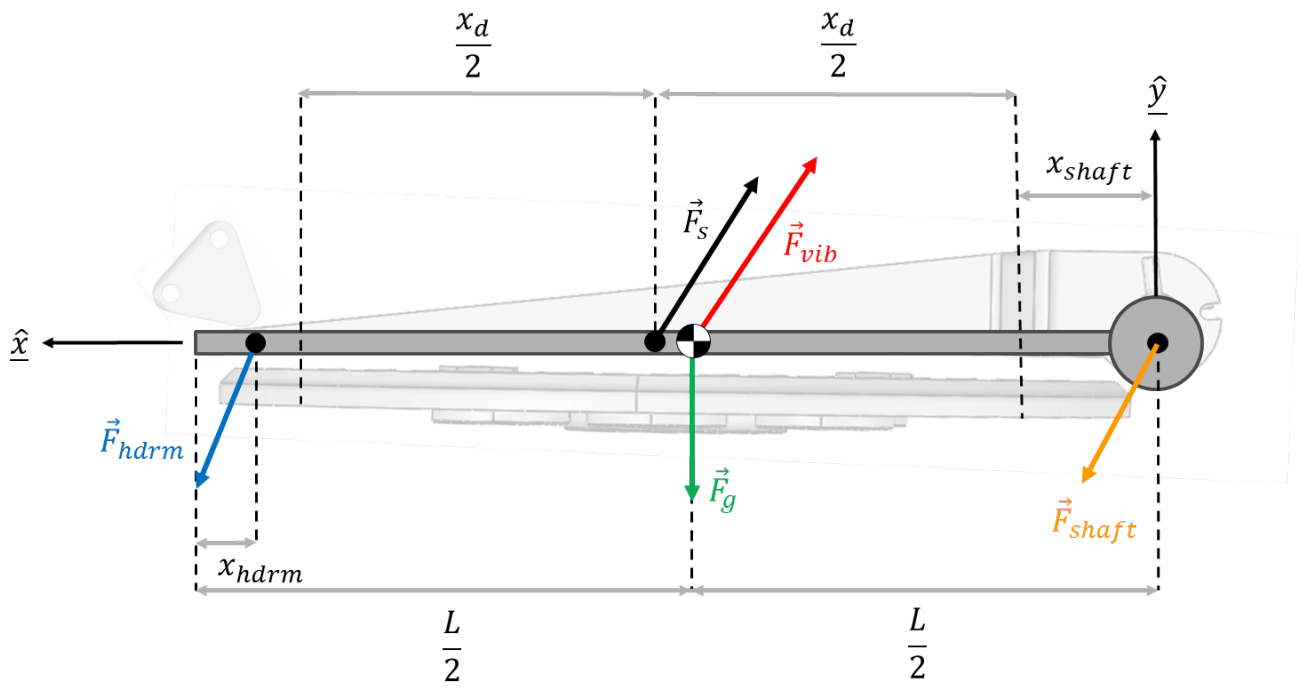

Figure 3.3: Static equilibrium schematic of the lever, part of the cover assembly.

3.3 Actuation

The design static forces being estimated for the vibration test sequence (driving mission phase), the actuation torque can be computed according the the ECSS Standards [11]. The mission phases considered for the release are the space-orbit release sequence and the release tests that will be performed during the AIT.

3.3.1 Actuation Torque

The actuation torque required to open the cryostat cover assembly is computed by considering the ECSS Standards, with the theoretical factors described in Table 3.1. The measured factor will be considered for the release operation during the cryogenic tests (AIT phase). The reason is that the tests are made in a controlled environment and lower uncertainties are therefore considered.

Resistive torque (or force) contributors	**Symbol**	**Theoretical Factor**	**Measured Factor**
Inertia	I	1.1	1.1
Spring	S	1.2	1.1
Magnetic effects	H_M	1.5	1.1
Friction	F_R	3.0	1.5
Hysteresis	H_Y	3.0	1.5
Others (e.g., Harness)	H_A	3.0	1.5
Adhesion	H_D	3.0	3.0

Table 3.1: Minimum uncertainty factors for actuation function [11].

According to ECSS Standards [11], the minimum actuation torque T_{min} shall be derived by the following:

$$T_{\text{min}} = 2 \cdot (1.1 \cdot I + 1.2 \cdot S + 1.5 \cdot H_M + 3.0 \cdot F_R + 3.0 \cdot H_\gamma + 3.0 \cdot H_A + 3.0 \cdot H_D) + 1.25 \cdot T_D + T_L \quad (3.6)$$

where I is the resistive inertial torque applied to a mechanism subjected to acceleration in an inertial frame of reference (e.g. spinning spacecraft, payload or other), T_D is the inertial resistance torque caused by the worst-case acceleration function specified by the customer at the mechanism level, and T_L is the deliverable output torque, when specified by the customer. Table 3.1 specifies the minimum uncertainty factors that can be adapted within the Equation 3.6. Note that the safety factor are not needed for the on ground tests.

The resistive inertial torque I can be neglected since the spacecraft nor the payload are not spinning. In addition, since the current design does not include any springs (the sheet spring should be replaced by a passive safety release device) and is not subjected to any magnetic effect nor hysteresis, Equation 3.6 is rearranged as follows:

$$\begin{aligned} T_{\text{min}} &= 2 \cdot \left(1.1 \cdot \cancel{I} + 1.2 \cdot \cancel{S} + 1.5 \cdot \cancel{H_M} + 3.0 \cdot F_R + 3.0 \cdot \cancel{H_\gamma} + 3.0 \cdot \cancel{H_A} + 3.0 \cdot H_D\right) + 1.25 \cdot T_D + \cancel{T_L} \\ &= 2 \cdot (3.0 \cdot F_R + 3.0 \cdot H_D) + 1.25 \cdot T_D \end{aligned} \tag{3.7}$$

where T_L is neglected since no deliverable output torque is specified by CNES and H_A is also neglected since no additional effect are considered.

Inertia Torque

The inertial resistive torque in worst case acceleration T_D requires to evaluate the inertia of the whole cover assembly and the rotational acceleration profile. First, the mass moment of inertia of the cover assembly is computed using the CAD model in *SolidWorks*. Figure 3.4 shows the considered part of the CAD model, and the axis considered in the software, since they are not defined the same way. Therefore, the mass moment of inertia taken at the center of mass of the entire cover assembly equals $I_{CoM,yy} = 0.37\,\text{g} \cdot \text{m}^2$.

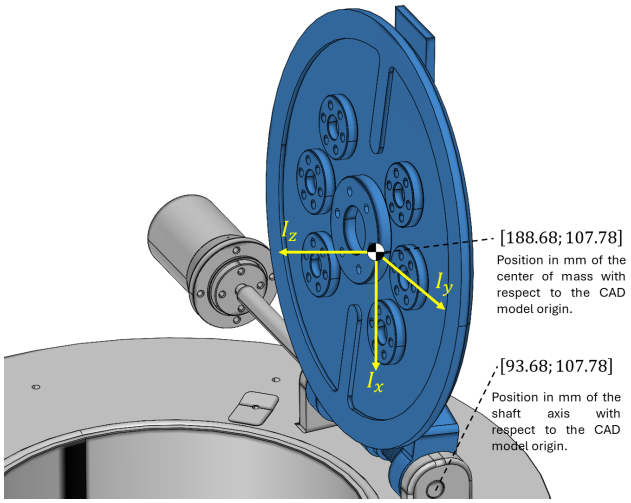

Figure 3.4: CAD model of the cover assembly, with the moment of inertia axis defined in *SolidWorks*.

Since the rotation is performed along the shaft axis, the Parallel-axis Theorem [44] is used to computed the mass moment of inertia of the current rotational motion:

$$I_{yy} = I_{CoM,yy} + md^2 = 2.48\,\text{g} \cdot \text{m}^2 \tag{3.8}$$

where I_{CoM} is the mass moment of inertia taken at the center-of-mass of the body, m is its mass and d is the distance between the center-of-mass and the rotational axis considered.

Second, a sinusoidal acceleration profile is selected assuming that the cover assembly should open within $\Delta t = 60\,\text{s}$ at an angular range of $\Delta\theta = 120\,\text{deg}$. The angular position over the time is therefore expressed as:

$$\theta(t) = \frac{\Delta\theta}{2}\left(1 - \cos\left(\frac{\pi t}{\Delta t}\right)\right) \tag{3.9}$$

The acceleration is derived by twice differentiate the angular displacement and its maximal value is evaluated, which results as the followings:

$$\ddot{\theta}(t) = \frac{\Delta\theta}{2}\left(\frac{\pi}{\Delta t}\right)^2 \cos\left(\frac{\pi t}{\Delta t}\right) \Rightarrow \ddot{\theta}_{\text{max}} = \frac{\Delta\theta}{2}\left(\frac{\pi}{\Delta t}\right)^2 = 0.0029\,\text{s}^{-2} \tag{3.10}$$

Finally, the inertial resistive torque is evaluated as follows:

$$T_D = I_{yy} \cdot \ddot{\theta}_{\text{max}} = 7.2 \cdot 10^{-6}\ \text{N m} \tag{3.11}$$

Friction Torque

The static loads derived earlier will be used to compute the friction torque. Computing the resultant force of the shaft reaction forces, and assuming Vespel/Aluminum contact at the bearings ($\mu_s \simeq 0.15$) [12], the friction torque is estimated as follows:

$$T_{F_R} = (\mu_s F_{shaft}) \cdot \frac{d_{shaft}}{2} = 0.906\,\text{N m} \tag{3.12}$$

where $F_{shaft} = 2.03\,\text{kN}$ is the resultant reaction force on the shaft, $d_{shaft} = 8\,\text{mm}$ is the diameter of the shaft, provided by the CAD model.

Adhesion Torque

The adhesion of the cover to the o-ring joint due to cryogenic conditions has a lot of uncertainties. As a first approximation, the adhesion is assumed to be compensated exactly by a safety release device (e.g. kick springs, passive thermo-component, etc.) that should be designed.

Actuation Torque

According to the ECSS standards, the minimal torque required to actuate the release of the cover assembly is computed by Equation 3.6 and equals:

On ground test:	In-orbit:
$T_{\text{min}} = 0.906\,\text{N m}$	$T_{\text{min}} = 5.436\,\text{N m}$

(3.13)

3.3.2 Actuator Choice

The PhySpace stepper motor of Phytron [39] is the actual choice of actuator to open the cover assembly. The electrical consumption for the opening operation is critical to be assessed because the power consumed is dissipated into heat that could significantly perturb the thermal balance of the cryostat and on the DEA surroundings. The actuation time is set to 60 s, and since the current $I = 600\,\text{mA}$ and resistance $R = 4.6\,\Omega$ for the 50 mN actuator, are provided by the manufacturer's datasheet, the electrical power consumed during the actuation is estimated to:

$$P = \left(I^2 \cdot R\right) = 1.656\,\text{W} \tag{3.14}$$

Finally, since the actuator torque equals 50 mN, a gearbox device is required to reach the ECSS torque computed in Equation 3.13. The gearbox ratio is required to be larger than 109 : 1, which is totally acceptable since previous design already included gearbox with ratio typically varying between $100 \rightarrow 200$: 1. However, the friction within the gearbox should be carefully evaluated since this will be a non-negligible additional heat source. This remains as a part of the future work to be achieved with the cover design.

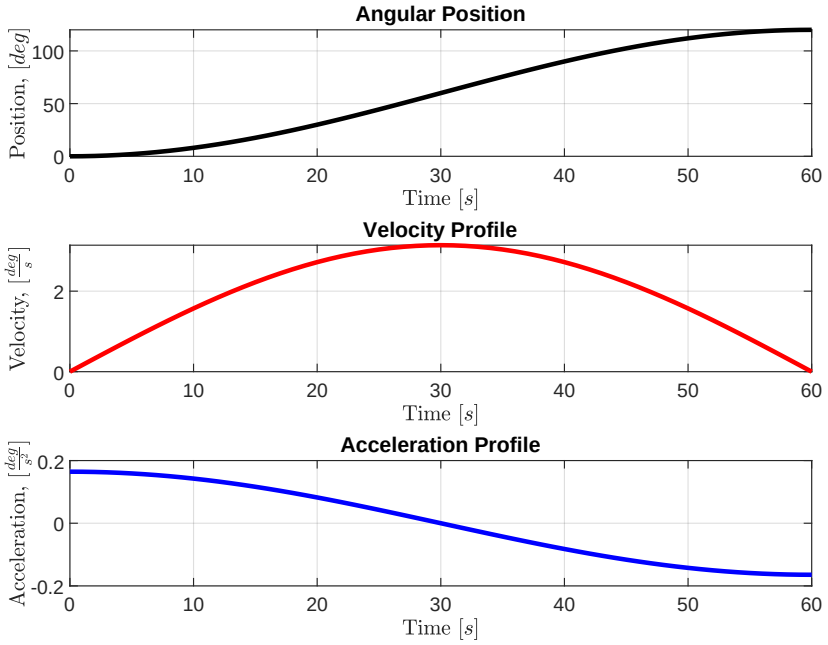

Figure 3.5: Position, velocity and acceleration profiles of the door opening.

3.4 Conclusion

To conclude this preliminary summary of the actual cover design, the CAD model is used to derive all the characteristics of the cover (mass, dimensions, etc.) that are needed to design the HDRM. Since the design of the cover is not central in the scope of this master thesis, a lot of parts should already be considered and have been neglected for the HDRM design. The adhesion force of the gasket to the cover surface is assumed to be perfectly balanced by a passive safety release (replacing the kick springs) which also needs to be designed. The shape of the cover provided by the CAD model is also not definitive and should be closer to a dome to withstand the pressure gradient. Moreover, the interface between the door and the lever should include springs to redistribute uniformly the seal force along the gasket circumference. Finally, even if the actuator choice is set, a more accurate evaluation of the heat generated during the opening operation should be made, and strategies to evacuate these thermal loads should be presented.

Chapter 4

Hold-on and Release Mechanism Modeling

The HDRM is a critical part of the cover assembly mechanism, since it locks the door during the launch phase to maintain the tightness of the gasket. The selection of linkage family is related to the Chebyshev four-bar linkage family. They are several reason that justifies this design choice:

1. The Herschel configuration used a specific Chebyshev four-bar linkage compliant with its own kinematic constraints.
2. The dimensional constraints along the vertical axis are limiting the choice of configuration. Indeed, with only 80 mm above the baseplate and 55 mm below, the HDRM is almost forced to be horizontally oriented.
3. The motorized actuation imposed by the requirements can only provide small actuation force or torque. Since the required HDRM force computed in Section 3.2.2 is around 1 kN, the linkage should provide an attenuating arm-lever to inhibit the force transmitted during the launch lock phases and minimize the actuation force required to initiate the release motion of the HDRM. Also, the greater the actuation force, the more current to power the actuator is, which could generate a lot of thermal losses that could perturb the thermal balance of the dewar.
4. A wide range of actuators family require a linear motion. Since the motorized actuator should work using a worm screw, a linear path is also required in this design case.

This chapter derives first the parametric HDRM model analytically. Then, the static equilibrium is assessed to evaluate the loads at each link (point) of the mechanism. This will be used to computed a force ratio between the HDRM force required and the actuation force. Finally, the validation of the analytical model is discussed using the *SolidWorks* software.

4.1 HDRM Parametric Model

The main purpose of this section is to describe the parametric model of the HDRM implemented in *MATLAB* from analytical kinematic and static equations. More particularly, the section introduces the analytical equations implemented to build the parametric analytical code.

4.1.1 Chebyshev Four-bar Kinematic

The Chebyshev linkage mechanism is a four-bar linkage converting a rotational motion into an approximate linear motion [45]. Figure 4.1 represents the classical configuration of the linkage. The red points represent the moving articulation of the mechanism while the black points remain fixed. The dashed lines represent the related motion of the point F with respect to the point C. All the pieces considered are assumed to be rigid bodies.

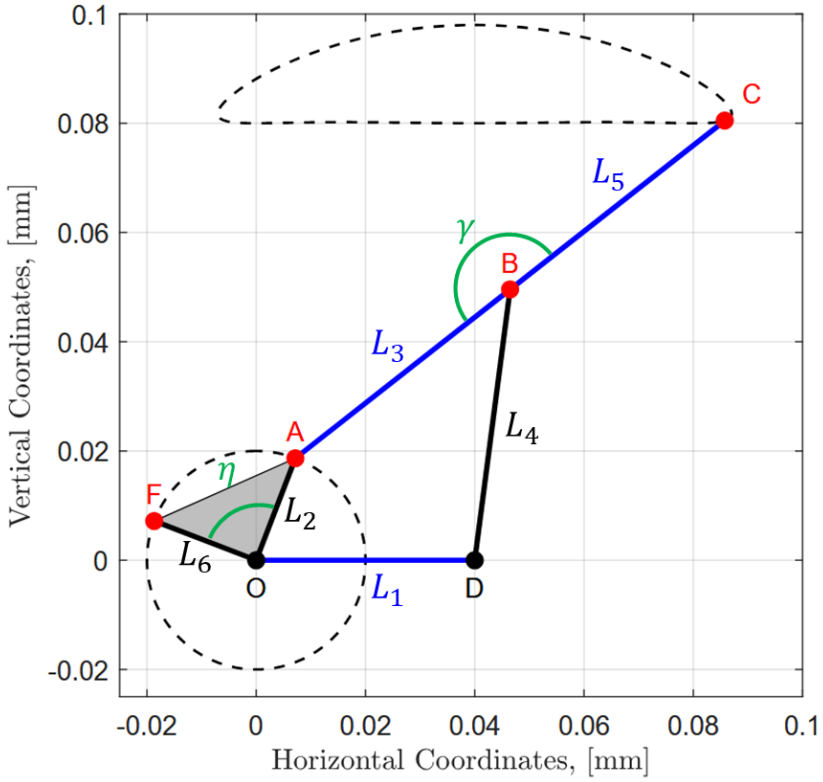

Figure 4.1: Classical configuration of the Chebyshev four-bar linkage.

The first moving piece is the knee, represented by the points A, F and O. The second moving piece is a lever bar represented by the points A, B and C. The third moving piece is an oscillating leg represented by the points B and D. The last bar is represented by the points O and D, which are fixed. A total of 9 geometrical parameters are considered to describe the linkage's behavior, which are defined as follows:

- The length $L_{OD} \equiv L_1$;
- The length $L_{BD} \equiv L_4$;
- The angle $\angle AOF \equiv \eta$;
- The length $L_{OA} \equiv L_2$;
- The length $L_{BC} \equiv L_5$;
- The angle $\angle ABC \equiv \gamma$;
- The length $L_{AB} \equiv L_3$;
- The length $L_{OF} \equiv L_6$;
- The angle $\angle \hat{x}OD \equiv \psi$;

One can note that the angle $\angle \hat{x}OD$ is not shown in Figure 4.1 since the points O and D are aligned with the horizontal axis for this theoretical configuration. The variable angle $\angle AO\hat{x} \equiv \theta$ is the angle describing the rotational motion of the knee piece. This motion is entertaining the other piece of the mechanism, and the output motion that is aimed to be designed to be compliant with the required kinematic is the motion of the point C.

The points $O : (x_O, y_O)$ (origin of the inertial frame of reference) and $D : (x_D, y_D)$ are fixed, and their positions are expressed as follows:

$$\begin{aligned} x_O &= 0 & x_D &= L_{OD} \cdot \cos(\psi) \\ y_O &= 0 & y_D &= L_{OD} \cdot \sin(\psi) \end{aligned} \tag{4.1}$$

The kinematic of the points $A : (x_A, y_A)$ and $F : (x_F, y_F)$ are modeled using polar coordinates as follows:

$$\begin{aligned} x_A &= L_{OA} \cdot \cos(\theta) & x_F &= L_{OF} \cdot \cos(\theta + \eta) \\ y_A &= L_{OA} \cdot \sin(\theta) & y_F &= L_{OF} \cdot \sin(\theta + \eta) \end{aligned} \tag{4.2}$$

The kinematic of the point $B : (x_B, y_B)$ is computed based on the position of the points D and A and their distance $L_{AD} \triangleq \sqrt{(x_A - x_D)^2 + (y_A - y_D)^2}$, as follows:

$$\begin{aligned} x_B &= \frac{(x_A + x_D)}{2} + \frac{L_{AB}^2 - L_{BD}^2}{2L_{AD}^2} \cdot (x_D - x_A) - \frac{(y_D - y_A)}{2} \sqrt{2\frac{L_{AB}^2 - L_{BD}^2}{L_{AD}^2} - \frac{\left(L_{AB}^2 - L_{BD}^2\right)^2}{L_{AD}^4} - 1} \\ y_B &= \frac{(y_A + y_D)}{2} + \frac{L_{AB}^2 - L_{BD}^2}{2L_{AD}^2} \cdot (y_D - y_A) - \frac{(x_A - x_D)}{2} \sqrt{2\frac{L_{AB}^2 - L_{BD}^2}{L_{AD}^2} - \frac{\left(L_{AB}^2 - L_{BD}^2\right)^2}{L_{AD}^4} - 1} \end{aligned} \tag{4.3}$$

Finally, the kinematic of the point $C : (x_C, y_C)$ is computed from the point B. In order to derive it, let's defined an intermediary angle Ω between the horizontal direction $\hat{x}$ and the segment L_{AB}. Since alternate (internal) angles have distinct vertex points and lie on opposite side of the parallel segments considered, the angle between the horizontal direction and the segment L_{BC} is defined as:

$$\angle \hat{x}BC \equiv \Omega - \gamma = \arctan\left(\frac{y_A - y_B}{x_A - x_B}\right) - \gamma$$

Therefore, the position of the point C is described by the following equation:

$$\begin{aligned} x_C &= x_B + L_{BC} \cdot \cos\left(\arctan\left(\frac{y_A - y_B}{x_A - x_B}\right) - \gamma\right) \\ y_C &= y_B + L_{BC} \cdot \sin\left(\arctan\left(\frac{y_A - y_B}{x_A - x_B}\right) - \gamma\right) \end{aligned} \tag{4.4}$$

At this stage of the implementation, the rigid bodies constraints need to be checked in order to keep only the physically acceptable motion of the entire mechanism.

4.1.2 Linear Path Detection Algorithm

The detection of linear path over the motion of the point C should detect not only horizontal or vertical linear segments, but also oblique segments. The use of direct gradient comparison is not well suited for such application, especially for vertical segments since their slope tends to infinity (will numerically explode).

The approach used concern the scalar product between two vectors, considering a reference vector at the starting point of the potential linear segment. Figure 4.2 illustrates the detection principle implemented. The red points are points outside the linear path detected (scale not respected in this scheme). The two blue points are the starting points of the linear segments, while the green ones are the succession point that stays within the specified tolerance compared to the reference segment.

Considering the unit vectors of both starting segment and current point segment (linking the first point of the supposed linear path), the angle between both vector is expressed as:

$$\vec{v}_i \cdot \vec{v}_j = \|\vec{v}_i\| \|\vec{v}_j\| \cos(\alpha) \Leftrightarrow \alpha = \arccos \frac{\vec{v}_i \cdot \vec{v}_j}{\|\vec{v}_i\| \|\vec{v}_j\|} \tag{4.5}$$

Then, to express the difference of position of the current point C_j compared to the segment $C_i C_{i+1}$, the distance between C_i and C_j is derived and multiplied by the sinus of the angle to get this difference, and compare it to the tolerance $\epsilon_{\max}$ specified by the algorithm:

$$\epsilon = \|\vec{v}_j\| \sin(\alpha) \leq \epsilon_{\max} \tag{4.6}$$

One can note that the linear path should have a minimal step length (one step corresponds to 1 degree of rotation of the point A). If this is not the case, the segment is rejected and the algorithm continues.

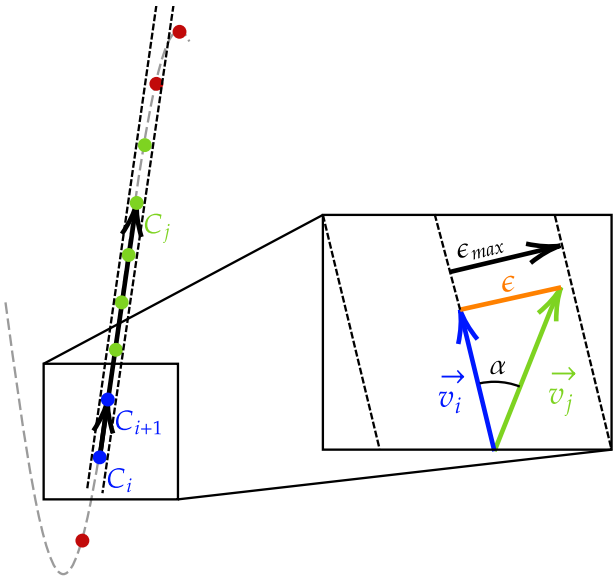

Figure 4.2: Geometry of the linear path detection principle implemented.

Once all the linear path segments of the point C motion are detected, the indices of the maximal and minimal angles θ are obtained, and will be used for the compliance check of the kinematic with respect to the cover's opening motion and for the static computations.

4.1.3 Opening Kinematic Constraint Formulation

During the launch lock phase of the mission, the function of the HDRM is to provide the necessary force to cancel the opening force exerted by the cover lever and remain sealed. But once the release campaign starts, the knee should opens enough to avoid any contact with the motion of the cover lever. The contact point F of the knee on the cover lever is indeed not exactly located at the tip. This requirements needs to be implemented and will be a strong driver of the discrimination of all the configuration considered. Figure 4.3 presents the geometry of the problem. The lever length is represented by the segment $L_{O'T}$. The gray dashed lines are showing the motion path of both tip points T and F. The knee piece is represented by the triangle $\triangle AOF$.
The contact point is defined with the angle θ_{cl} which is the largest angle θ of the mechanism within the angular range corresponding to the linear motion of the point C. The idea is to check that the angular range $\Delta\theta \equiv \theta_{cl} - \theta_{op}$ is larger that the minimum angle between the contact point F and the intersection point F' between the motion circle of the cover lever and the motion circle of the contact point.

The intersection point F' is computed using the *circcirc* built-in function in *MATLAB* [46]. The only accepted configuration are the ones that have the contact point below and on the left side of the fixed point O. From this assumption, the minimum angular range required to safely open the door is expressed as follows:

$$\Delta\theta_{\text{min}} = \arccos\left(1 - \frac{L_{FF'}^2}{2L_{OF}^2}\right) \leq \Delta\theta \tag{4.7}$$

4.1.4 Static Equilibrium

The aim of this section is to express the static equilibrium system over the entire HDRM and to compute the actuation force required to counter balance the launch lock force the knee should balance to remain static. The equilibrium equation will be derived first by considering each piece of the HDRM, and then by

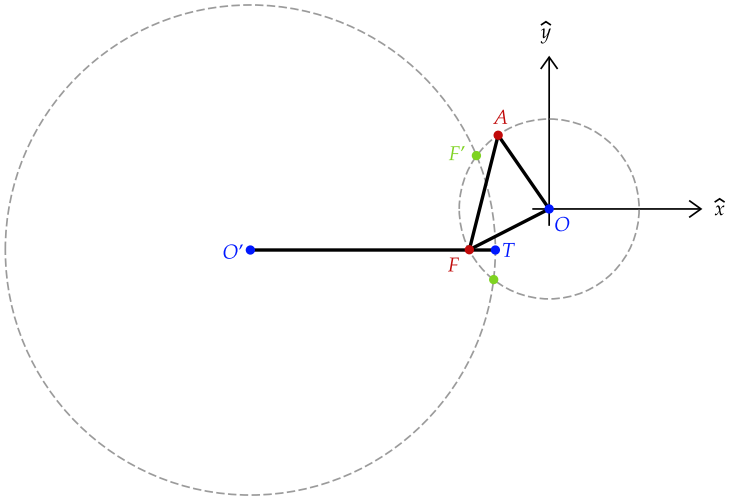

Figure 4.3: Geometry of the opening kinematic constraint problem.

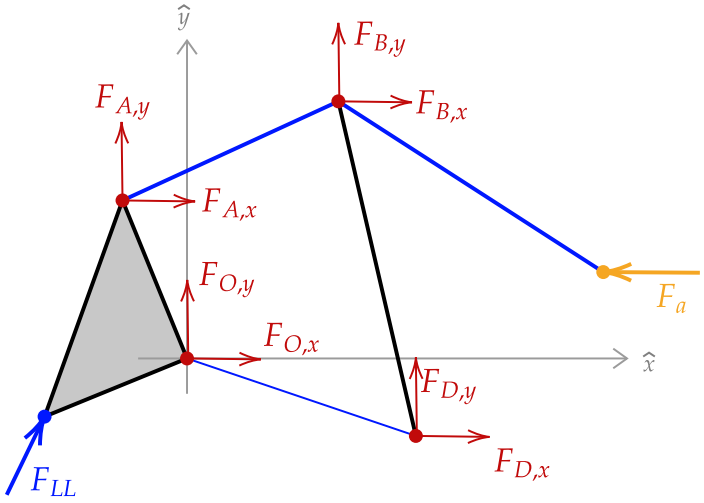

Figure 4.4: Static equilibrium schematic of the HDRM.

considering the overall system. Figure 4.4 shows the overall static equilibrium forces involved. The color of the links enable to distinguish the different pieces of the mechanism. The fixed bar $O \rightarrow D$ is a fictive link.

The system is assumed purely 2 dimensional. The forces along $\hat{x}$ and $\hat{y}$ only are considered, and the moments along the $\hat{z}$ axis are considered. One can note that the moment are positive counter clock-wise. Let's consider the knee piece's static equilibrium first. The forces considered are acting on the knee. F_O is the force acting from the fixed hinge to the knee; F_A is the force acting from the lever bar to the knee; $F_{LL} \equiv F_{hdrm}$ is the force acting from the cover lever to the knee. The static equations (for the forces along $\hat{x}$, $\hat{y}$ and for the moments along the $\hat{z}$) can be derived as follows:

$$\begin{aligned} 0 &= F_{LL,x} + F_{O,x} + F_{A,x} \\ 0 &= F_{LL,y} + F_{O,y} + F_{A,y} \\ 0 &= (y_O - y_F) \cdot F_{LL,x} + (y_O - y_A) \cdot F_{A,x} + (x_F - x_O) \cdot F_{LL,y} + (x_A - x_O) \cdot F_{A,y} \end{aligned} \tag{4.8}$$

Next, the lever bar is considered. The force are acting on the lever, and the signs need to be carefully defined. F_A is the force acting from the lever to the knee. Consequently, $-F_A$ is the force acting from the knee to the lever. F_B is the force acting from the leg to the lever; $F_C \equiv F_a$ is the actuation force acting from the actuation transmission to the lever. The static equations are then derived by the same way as for the first piece (the link A is taken as reference point for the moment):

$$\begin{aligned} 0 &= -F_{A,x} + F_{B,x} + F_{C,x} \\ 0 &= -F_{A,y} + F_{B,y} + F_{C,y} \\ 0 &= (y_A - y_B) \cdot F_{B,x} + (y_A - y_C) \cdot F_{C,x} + (x_B - x_A) \cdot F_{B,y} + (x_C - x_A) \cdot F_{C,y} \end{aligned} \tag{4.9}$$

After, the leg piece is considered. The forces are acting on the leg. $-F_B$ is the force acting from the lever to the leg and F_D is the force acting from the fixed hinge to the leg. The static equations are then derived similarly (the link D is taken as reference point for the moment):

$$\begin{aligned} 0 &= -F_{B,x} + F_{D,x} \\ 0 &= -F_{B,y} + F_{D,y} \\ 0 &= (y_D - y_B) \cdot F_{B,x} + (x_B - x_D) \cdot F_{B,y} \end{aligned} \tag{4.10}$$

Finally, the overall equilibrium enables to derive the 3 last equations required to enclose the problem. The force considered are acting on the overall HDRM. The static equations are then derived similarly (the fixed hinge O is taken as reference point for the moment):

$$\begin{aligned} 0 &= F_{LL,x} + F_{O,x} + F_{D,x} + F_{C,x} \\ 0 &= F_{LL,y} + F_{O,y} + F_{D,y} + F_{C,y} \\ 0 &= (y_O - y_F) \cdot F_{LL,x} + (y_O - y_C) \cdot F_{C,x} + (y_O - y_D) \cdot F_{D,x} + \\ &\quad (x_F - x_O) \cdot F_{LL,y} + (x_C - x_O) \cdot F_{C,y} + (x_D - x_O) \cdot F_{D,y} \end{aligned} \tag{4.11}$$

One can note that the system should not give a unique solution. An additional constraints of the system needs to be applied to have a full rank matrix. Rearranging the equations into a matrices system gives the following system of equation to solve:

$$\begin{bmatrix} 1 & 0 & 1 & 0 & 0 & 0 & 0 & 0 & 0 & 0 \\ 0 & 1 & 0 & 1 & 0 & 0 & 0 & 0 & 0 & 0 \\ 0 & 0 & -y_A & x_A & 0 & 0 & 0 & 0 & 0 & 0 \\ 0 & 0 & -1 & 0 & 1 & 0 & 1 & 0 & 0 & 0 \\ 0 & 0 & 0 & -1 & 0 & 1 & 0 & 1 & 0 & 0 \\ 0 & 0 & 0 & 0 & y_A - y_B & x_B - x_A & y_A - y_C & x_C - x_A & 0 & 0 \\ 0 & 0 & 0 & 0 & -1 & 0 & 0 & 0 & 1 & 0 \\ 0 & 0 & 0 & 0 & 0 & -1 & 0 & 0 & 0 & 1 \\ 0 & 0 & 0 & 0 & y_D - y_B & x_B - x_D & 0 & 0 & 0 & 0 \\ 1 & 0 & 0 & 0 & 0 & 0 & 1 & 0 & 1 & 0 \\ 0 & 1 & 0 & 0 & 0 & 0 & 0 & 1 & 0 & 1 \\ 0 & 0 & 0 & 0 & 0 & 0 & -y_C & x_C & -y_D & x_D \\ 0 & 0 & 0 & 0 & 0 & 0 & 0 & 1 & 0 & 0 \end{bmatrix} \begin{bmatrix} F_{O,x} \\ F_{O,y} \\ F_{A,x} \\ F_{A,y} \\ F_{B,x} \\ F_{B,y} \\ F_{C,x} \\ F_{C,y} \\ F_{D,x} \\ F_{D,y} \end{bmatrix} = \begin{bmatrix} -F_{LL,x} \\ -F_{LL,y} \\ y_F \cdot F_{LL,x} - x_F \cdot F_{LL,y} \\ 0 \\ 0 \\ 0 \\ 0 \\ 0 \\ 0 \\ -F_{LL,x} \\ -F_{LL,y} \\ y_F \cdot F_{LL,x} - x_F \cdot F_{LL,y} \\ 0 \end{bmatrix} \tag{4.12}$$

For the configurations that have a linear path oblique, the horizontal at the point C is decomposed into a component aligned with the direction of the linear path and a component that is perpendicular to this direction. This is computed by considering the average slope between the opening and the closing point from which the angle is deduced. Therefore, the unknown vector $\vec{\boldsymbol{F}}$ is adapted to this after solving this system of equation as follows:

$$\begin{aligned} \vec{F_7} &= F_{C,x} \cdot \cos(\alpha) \equiv F_{C,x} \\ \vec{F_8} &= F_{C,x} \cdot \sin(\alpha) \equiv F_{C,y} \end{aligned} \tag{4.13}$$

where $\alpha = \arctan\left(\frac{y_{C,op}-y_{C,cl}}{x_{C,op}-x_{C,cl}}\right)$ is the angle between the average direction of the linear motion and the horizontal axis, the average being computed considering the position of the point C in the closed and in the opened configuration.

4.2 HDRM Model Validation

The next logical step is the validation of the analytical modeling. This step is critical to ensure the code is functional and ready to be wrapped into an objective function before using optimization algorithms to investigate the best configuration possible for given constraints.

The software that will be used to validate the results is *SolidWorks 2024* (using the *Motion Analysis* and *Simulation* add-ins). In parallel, a breadboard of a configuration is built and an experimental set-up is made in order to compare both the analytical and numerical results to experimental ones. However, due to circumstances, the experimental test is not presented in this report.

The Chebyshev four-bar linkage modeled in the previous section considers a set of 9 parameters. For the validation, 4 different sets have been considered:

- The classical Chebyshev four-bar linkage configuration;
- The Herschel's four-bar linkage configuration, roughly estimated from Janu et al. [2];
- A configuration that is not restrained in term of revolution of the knee;
- A configuration that is restrained in term of revolution of the knee.

The parameters of each configuration are presented in Table 4.1, where the length parameters are expressed in mm and the angle parameters are expressed in deg.

	L_{OD}	L_{OA}	L_{AB}	L_{BD}	L_{BC}	L_{OF}	η	γ	ψ
Classical	40.0	20.0	50.0	50.0	50.0	20.0	090	180	0.0
Herschel	115.1	72.3	59.5	74.7	55.6	45.2	090	140	0.0
A	30.0	15.0	37.5	37.5	37.5	15.0	090	270	0.0
B	85.4	44.7	51.3	65.5	55.6	45.2	108	310	0.0

Table 4.1: Recapitulatory table of the 4 validation configurations considered and their 9 parameters.

These four configurations are geometrically represented in Figure 4.5. The knee piece is represented as a gray shaded triangle. The lever piece is represented in blue as well as the fixed virtual piece. The leg is represented in black. The motion of the points C and F are represented both in dashed lines.

4.2.1 Chebyshev Four-bar Kinematic

The validation of the results considers only the motion of the point C of each configuration. Figure 4.6 compares the numerical results with the analytical one, for each considered configuration.

The analytical trajectories computed match to the numerical computed using *SolidWorks Motion Analysis*, except for the configuration B where a significant difference is observed around a singular point of the mechanism.
More quantitatively, Table 4.2 shows the average absolute error $\bar{\epsilon}$, the root mean square (RMS) error ϵ_{RMS} and the maximum absolute error ϵ_{max}. One can observe that the errors for configuration that permits full

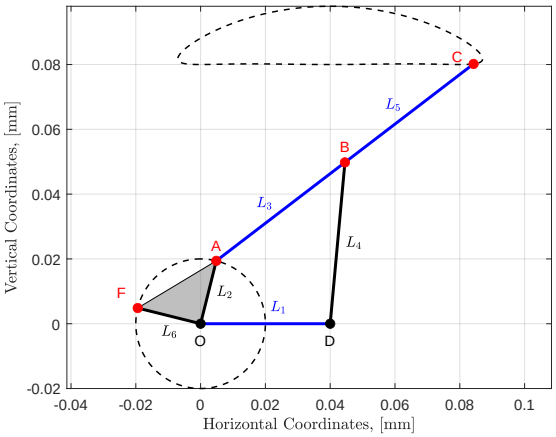

(a) Chebyshev classical configuration.

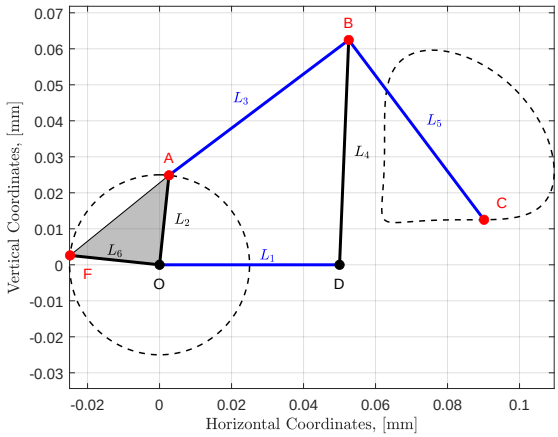

(b) Configuration *A*.

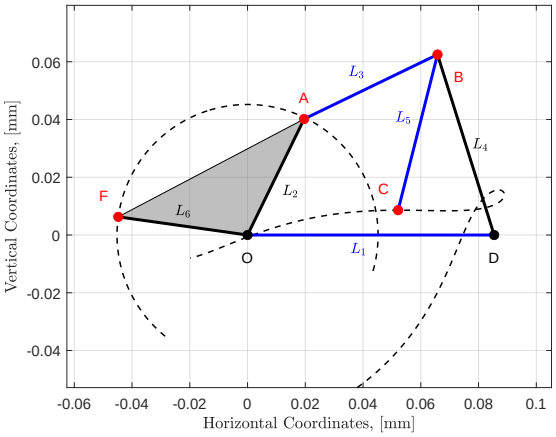

(c) Configuration *B*.

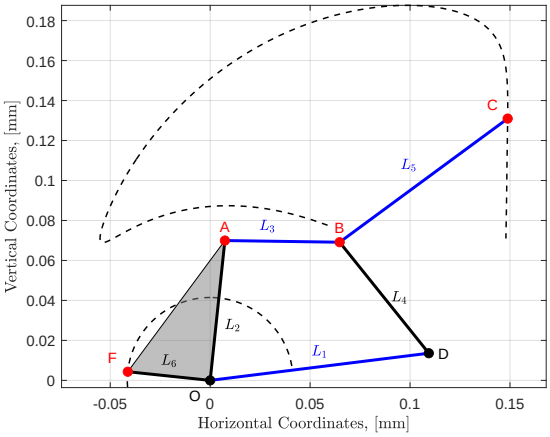

(d) Herschel configuration.

Figure 4.5: Representation of the four configurations considered for the kinematic validation.

	$\bar{\epsilon}$ [mm]	ϵ_{RMS} [mm]	ϵ_{max} [mm]
Classical	0.006	0.007	0.016
Herschel	0.055	0.071	0.189
A	0.012	0.015	0.036
B	0.010	0.011	0.037

Table 4.2: Errors made with the analytical code compared to the *SolidWorks Motion Analysis* results.

revolution motion are really accurate (below 0.01 mm). On the other hand, the results are still accurate for the Herschel configuration, which is not complete in terms of revolution. The accuracy is however 5 to 10 times decreased, but remains below the 0.30 mm. But for the configuration *B*, the accuracy is highly degraded around the small loop in the path. The reason might be that the big difference between the software and the analytical code is that the pieces have real dimensions, and are considered as rigid bodies. Since the code only compute the points coordinates over angular step and verify that the length between each points remains the same. For *SolidWorks*, since the piece motion is made by considering its entire volume, this might results in some differences, especially around the singular points of the mechanism. Another source of potential error in that case is the path measure by the *SolidWorks Motion Analysis*,

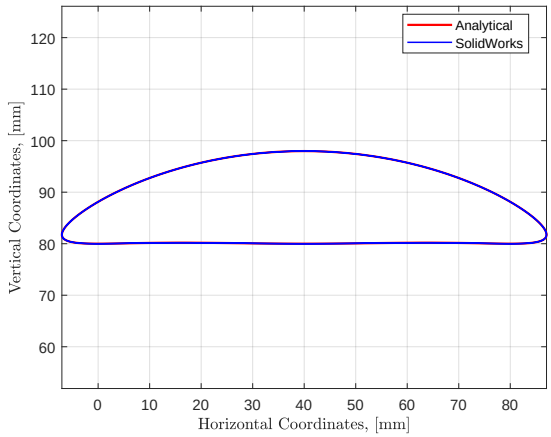

(a) Chebyshev classical configuration.

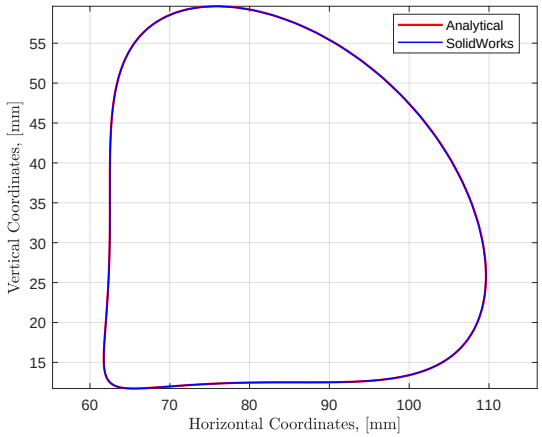

(b) Configuration *A*.

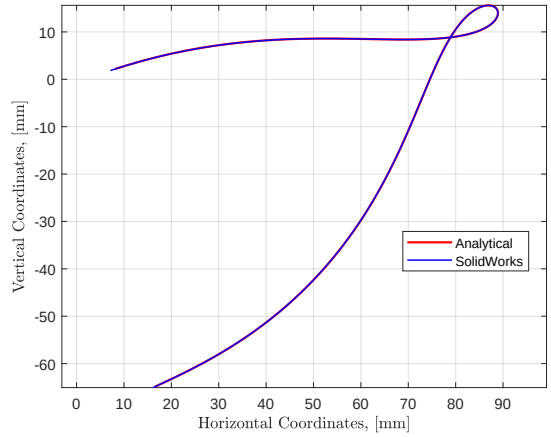

(c) Configuration *B*.

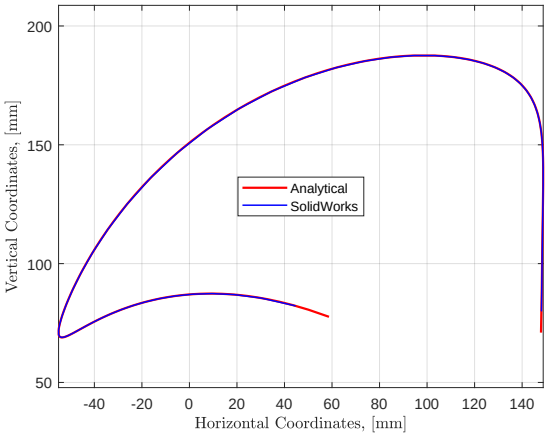

(d) Herschel configuration.

Figure 4.6: Comparison of the point *C* kinematic computed analytically in *MATLAB* and computed numerically by *SolidWorks Motion Analysis*.

which is processed by considering the motion of the center of the pin corresponding to the point *C*.

4.2.2 Static Equilibrium

The static equilibrium validation in closed configuration is slightly more delicate since the modeling using any software requires to represent what the analytical code is computing with its assumptions. Indeed, the software will always display a result, and the difficulty is to interpret them, and assess that the software is actually providing a close representation to what is aimed to model. The aim of this section is to validate the force ratio computed analytically since it will be critical for the choice of optimum configuration for the optimization process.

Since the basis of static equilibrium is slightly the same for *SolidWorks Simulation* or for *NX Siemens*, the numerical representation of the configuration being modeled already in *SolidWorks*, the same software will be used to assess the static validation of the *MATLAB* code. In addition, since the numerical modeling also states assumptions, an experimental validation is planned with the configuration *A* to assess the force ratio of both analytical and numerical model are close to the reality.

Numerical Modeling

The analytical model in the static equilibrium computations assumes a perfectly plane mechanism, where each constituting piece is a rigid body (meaning that the length of each link should remain constant). The forces are assumed punctual, and located at the coordinates of each point of the mechanism.

Figures 4.7 presents the numerical model used to validate the static. The fixed piece is excluded from the analysis. The hinges O and D are assumed fixed. The articulation A and B are modeled using *pin* connections object to enable the rotation bu not any translation. The point F where the HDRM is supposed to be applied is modeled as a *slider* surface (which is clamping any vertical motion). The force is not directly applied on the point F since it appears after a few attempts that applying a punctual *remote load* at specific location (determined with the analytical code) was the most accurate. The magnitude of the punctual load is taken from the analytical code and the resultant force on the slider surface in F is compared to the HDRM force inputted to the analytical code.

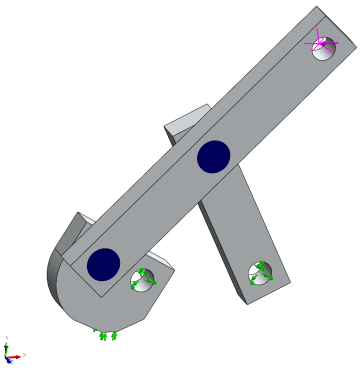

(a) Chebyshev classical configuration.

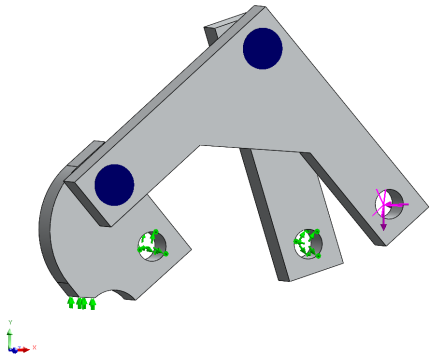

(b) Configuration A.

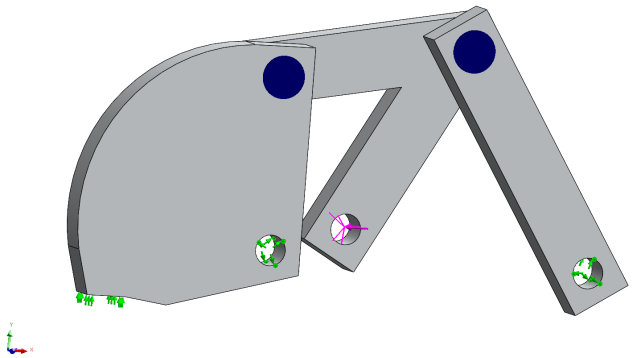

(c) Configuration B.

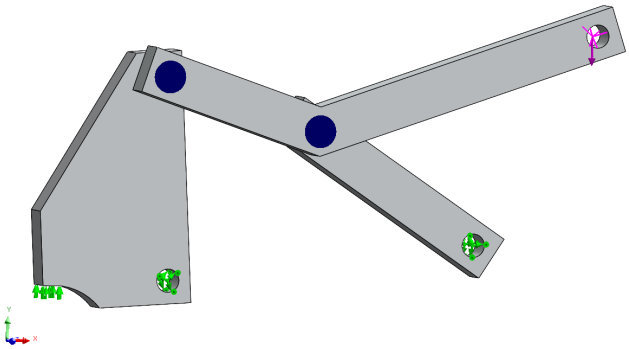

(d) Herschel configuration.

Figure 4.7: Representation of the four configurations considered for the kinematic validation.

Validation Results

The force ratio $F_{\text{ratio}} \equiv \frac{F_{hdrm}}{F_{act}}$ is computed considering the ratio of the HDRM force F_{hdrm} over the actuation force F_{act}. Table 4.3 presents the results of the *SolidWorks* model and compare the force ratios of each configuration considered with the analytical equivalent one.

One can observe that the difference is non-negligible for the Classical configuration and for the Herschel configuration.

	Force Ratio		ϵ_{abs} [−]	ϵ_{rel} [%]
	Analytical	SolidWorks		
Classical	0.3858	0.4134	0.028	6.688
Herschel	0.7247	0.6111	0.114	18.589
A	1.0190	1.0659	0.047	4.406
B	0.6722	0.6590	0.013	1.995

Table 4.3: Errors made with the analytical code compared to the *SolidWorks Simulation* results.

Even if the errors are significant for some configurations, the order of magnitude of the force ratio is nearly the same. The experimental measure of the force ratio on the configuration *A* could enforce the validation of the analytical code. However, due to some delay, the breadboard pieces[1] will not arrive on time and the experimental measures will not be performed in this version of the report.

4.3 Conclusion

To conclude this section about the HDRM modeling, the kinematics was analytically first derived considering the classical Chebyshev four-bar linkage configuration. After the implementation of the linear path detection code and the kinematic constraints for the release of the knee, the statics was derived. Starting from the HDRM force computed in Sections 3.2.1 and 3.2.2, the force ratio was computed. Once the parametric code was built, the validation of the code have been presented. This section enforced the reliability of the code providing accurate results, which is critical to assess the optimization process would work properly. The kinematics is validated with accurate result (less than 0.1 mm for the less accurate case). The statics is less accurate due to the conversion between perfectly planar motion into three dimensional numerical model. However, the force ratio remains is the same order of magnitude, but experimental measures should be done to enforce this validation.

[1] The drawings of the prototype are provided in the Appendices. In addition, the calibration tests description and results are also presented in the same section. Indeed, since the CSL has only one dynamometer device, an alternative method to evaluate the force is considered using the deflection of a cantilever beam.

Chapter 5

Optimization

The parametric model of the HDRM counts 9 distinct parameters that could affect the geometry of the HDRM, its linear path delivered and the actuation force required to conserve the static behavior during the launch phase and vibration phases. Since the force ratio between the HDRM force and the actuation force should be minimized without violating the kinematic and dimensional constraints, optimization of the HDRM configuration appears to be the logical next design step.

Therefore, this section first briefly describes different optimization algorithms considered as candidate for the optimization implementation. Then, the choice of optimization process is presented and discussed. Finally, the HDRM optimized configuration result is presented and discussed.

5.1 Optimization Method Descriptions

The general optimization workflow is given in the *MATLAB* documentation [47], with recommendations on the usage of each type of solver. First, the choice of the solver is made according to the type of problem considered. Next, the objective function and constraints functions should be implemented with respect to the syntax of the *Global Optimization Toolbox* algorithm implemented in *MATLAB*. After setting appropriate optimization options, the solver is run and the result is examined. Any unsatisfactory result leads to variation of the options before reiterating the process.

The aim of the optimization is to find the best solution to a defined problem according to its constraints and to the objective of the optimization. The proof of convergence to a global optimum is not easy to provide. Some algorithms provided by the *Global Optimization Toolbox* have no convergence proof yet, such as `Particleswarm` or `Genetic Algorithm` (ga) solvers. In fact, for discontinuous objective function problems, the convergence is never assessed and this is a real problem. Are the possible results outputted from any optimization processes the best obtainable solution or is there even better one?

5.1.1 Using Local Solver with Numerous Different Inputs

The `fmincon` is a nonlinear programming solver. It is a gradient-based method designed to work on objective and constraints functions that are continuously differentiable. When the problem is infeasible, `fmincon` attempts to minimize the maximum constraint value. The solver finds the local minimum of a

problem specified by the followings:

$$\min_{x} \quad f(x) \text{ s.t.} \quad \begin{cases} c(x) \leq 0 \\ c_{eq}(x) = 0 \\ A \cdot x \leq b \\ A_{eq} \cdot x = b_{eq} \\ lb \leq x \leq ub \end{cases} \tag{5.1}$$

where A is a real matrix and b a real vector representing linear inequality constraints, A_{eq} is a real matrix and b_{eq} a real vector representing linear equality constraints, lb and ub are vectors representing lower and upper bounds, and c and c_{eq} are arrays that represents nonlinear inequality and equality respectively. The solver also takes an objective function, a vector of initial values for the variation parameters x_0 and a nonlinear constraints function that wraps the nonlinear constraints c and c_{eq} [48].

Since the solver is designed to work with continuous objective and constraints functions, it is by definition not well-suited for the optimization of the HDRM configuration. Indeed, most of the time, it does not converge to a feasible solution that satisfies every nonlinear constraints, which are:

- The configuration should be compliant with all the kinematic and dimensional constraints (quasi-linear path sufficiently long to ensure the opening without collision with the door, and stay within the height available, without violating the height of the interfaces of the V-groove or the cryostat). If the boolean flag `valid` equals 0 (meaning `False`), $c_{eq} = 1$ while the satisfaction of the constraint (`valid` equals 1) leads to $c_{eq} = 0$.
- The configuration should provide enough place for the motorized actuator and its potential gearbox. `fmincon` attempts to satisfies $c(x) \leq 0$. The projection of the linear path until reaching the bottom or the upper interface defines a distance that should be positive.

However, some inputs vector x_0 can allow the tool to converge to a local feasible solution. Therefore, the idea of this first optimization process is to consider a large set of initial vector x_0, to loop over them by calling each time the `fmincon` solver and save the feasible local solution identified. It is based on the fact that the objective functions has feasible and non-feasible local optimum that have an influence region (basins of attraction) on their local surroundings. The solver may be stuck in some region due to a local optimum that is not feasible for a given initial vector. Hence, considering different initial vectors within the considered bounds may be efficient to identify different acceptable solution.

The remaining problem is that the solutions identified are only local optimum and not global ones. Even if discrimination criteria (such as the force ratio and the available place to put the actuator in the continuity of the linear path) are applied to rank them, the algorithm does not ensure the global optimum is reached within the provided bounds.

5.1.2 Global Search and Multistart Algorithms

The solvers `GlobalSearch` and `Multistart` attempt to locate a solution that minimize the objective function value. Both algorithm start a local solver, like`fmincon` for example, from multiple start points [49]. The idea is to use multiple starting point to sample different basins of attraction. Theses gradient-based methods have been fast convergence proven for smooth (continuously differentiable) objective functions. While the `GlobalSearch` solver removes many start points heuristically because they offer low potential of feasible convergence solution, `Multistart` runs all the starts points or combination of them to identify the global optimum [47].

The `GlobalSearch` solver has the same approach as proposition of process discussed with the solver

`fmincon`. Since it rejects also a lot of starting point that could be potential feasible solution seeds, the `Multistart` solver is preferred. However, due to the discontinuous objective function implemented, the convergence to a global optimum is not assessed. Indeed, the solution highly depends on the inputs vector given as parameter to the solver.

5.1.3 Pattern Search Algorithm

The `Pattern Search` algorithm starts from an initial guess x_0 with an initial step size positive. The process evaluates at each iteration the objective function at a set of surrounding points around the current one. These points are determined by applying basic operations on vectors from a pattern. When a better point is found, the reference point for the search stage is changed, and possibly increases the step size. If no improvement is found, the step size is reduced. The algorithm reduces its step size until reaching a critical size indicating the convergence of the method [50].

This non gradient-based algorithm has been proven to converge to local optimum, but its rate of convergence is slower than gradient-based methods [51]. For this algorithm, the *MATLAB* documentation recommends to use several initial points x_0 in the case of non-smooth problem [52]. Again, the problem remains the same: the algorithm does not ensure the global optimum is reached within the provided bounds.

5.1.4 Surrogate Optimization

A surrogate is a function that approximate another time-consuming objective function. The idea is to evaluate a function that takes significantly less time to output a result. It minimizes the result of this simplified function before evaluating the improvement made with the approximation output [53]. The algorithm balances the optimization process between solution exploration and time consumption. It also has been proven to converge to a global solution for continuous objective functions on bounded domains [54]. It converges slower than gradient-based solvers and the solver generally stops by reaching a function evaluation limit (or any other limit specified in the options) [55]. Since the current design problem is non-smooth, the documentation also recommends to use several initial points [52].

5.1.5 Quasi-Monte Carlo Algorithm

The Quasi-Monte Carlo method is a pseudo-probabilistic problems solver using low-discrepancy sequences (uniformly distributed) [56]. For a given random variable f (a given function), the Monte Carlo algorithm estimate for the expected value $E(f)$ is obtained by taking N independent distributed random samples $a_1, ..., a_N$ such as:

$$E(f) \approx \frac{1}{N} \sum_{n=1}^{N} f(a_1, ...a_n) \tag{5.2}$$

For large sample numbers, thanks to the law of large numbers, this procedure converges almost surely [56]. The main difference with the classical Monte Carlo method is the use of pseudo-random distribution sequences [57]. Figure 5.1 illustrates the difference between the distribution of points using pseudo-random sequences like Monte Carlo algorithms uses, and using a low-discrepancy sequence generation such as Halton or Sobol sequences. The first 10 points are represented in red, the next points until the 100^{th} point are colored in blue, and the following points until the 256^{th} point (arbitrary choice of number of points) are represented in green.

The Halton sequence use different prime bases to form successively finer uniform partitions of the given unit interval in each dimension specified [58]. The Sobol sequence uses a base of 2 (source of the likely symmetrical pattern shown in Figure 5.1) to form successively finer uniform partitions of the unit interval,

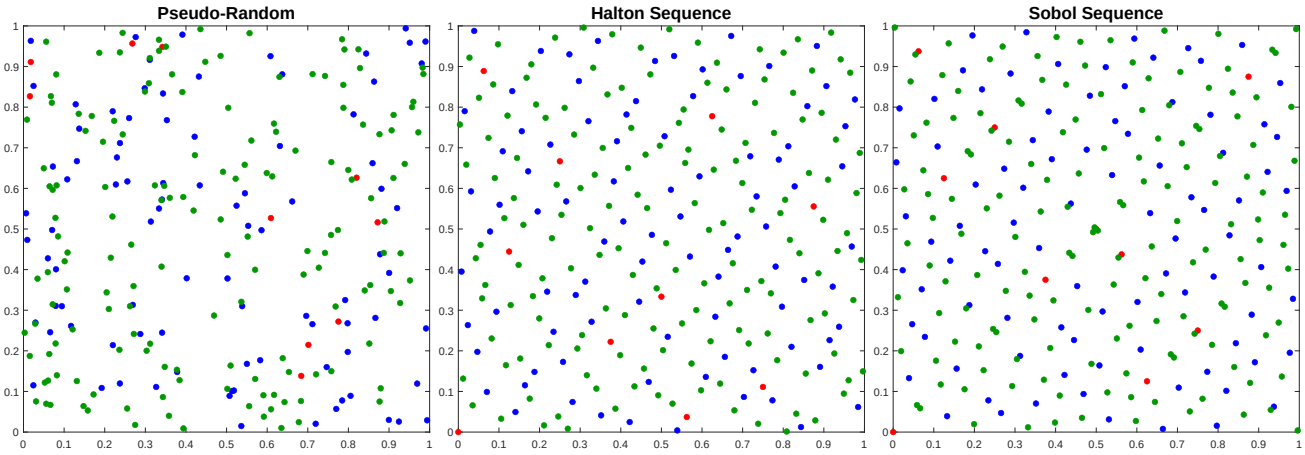

Figure 5.1: Comparison of the Halton, the Sobol and Pseudo-random sequence generations in $(0,1) \times (0,1) \in \Re^2$.

before reordering the coordinates in each dimension [59]. Both sequences provide a fine uniform partition of the given interval in each dimension with sufficiently high number of point generated.

5.1.6 Optimization Algorithm Choice

Reaching a global optimum is not an easy task, even for smooth problem. For the current design problem, the constraints (kinematic and physical) are limiting the field of acceptable solution, which consequences in a highly non-smooth problem definition. For such non-linear problem, ensuring a global solution is found is difficult, and could be the subject of a complete dedicated work to rigorously proof it.

This objective of the optimization process is getting an acceptable HDRM configuration that satisfies all the constraints and provide low force ratio rather than getting the best possible one. A configuration that transmits $10 \rightarrow 50\,\text{N}$ at the actuation point is typically what should be obtained.

A first (direct) approach would implement a code that will generate a set of local optimum solution feasible, using the `fmincon` local solver for a large set of inputs. Next, the `Pattern Search` local solver and the `Surrogate` algorithm will be used both with the set of local optimal solution to identify the best configurations within the ones considered during the first step. The initial large set of input should cover almost the entire field of the boundary conditions provided in order to assess that the final optimized solution is likely the best solution that could be identified within the bounds and according the the nonlinear constraints considered. However, the first issue for this approach is the execution time due to the large set of parameters required to characterize the model. This could be time consuming, only considering angles variation and fixed length parameters (around $8 \rightarrow 16\,\text{hours}$ depending on the increase step). If the 6 other parameters were also varying, considering an increment of $0.5 \times x_{lb}$[1] the lower bound parameters for example, this should require to execute $14^9 = 2 \cdot 10^6$ time the loop over the 3 angle parameters, which took for the fastest execution even obtained 5 h (the execution time depends a lot on the initial parameters given which could facilitate or not the fast convergence of `fmincon`). And this is not a problem of code efficiency since the only part of the code that takes time to be executed is the plot generation, disabled for the optimization loop.

[1] As mentioned in previous Section 4.2 the lower bound parameters (c.f. Table 4.1), the classical Chebyshev four-bar linkage has specific proportional length parameters ($L_{OD} = 2a$, $L_{OA} = L_{OF} = a$, $L_{AB} = L_{BD} = L_{BC} = 2.5a$, a being a length parameter). In order to be able to detect other potential similar proportionality between the length parameters, the increment of $0.5 \times x_{lb}$ seems reasonable.

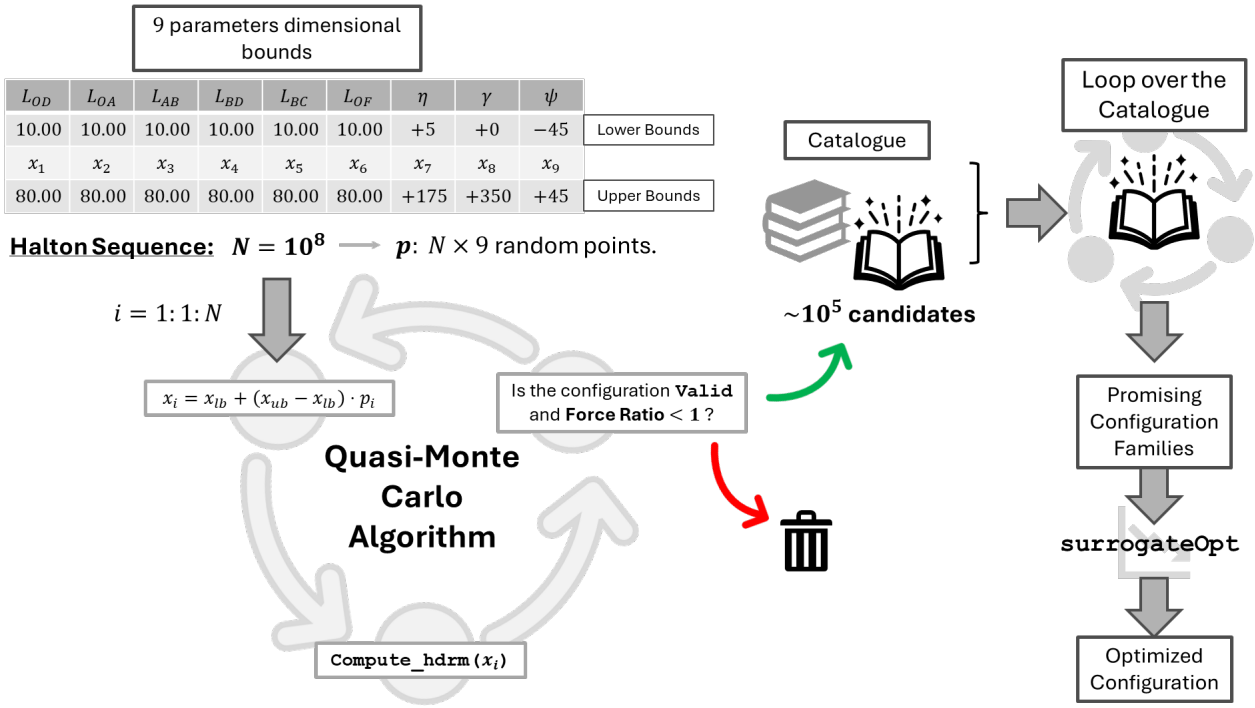

Figure 5.2: Proposed optimization approach workflow.

Since the direct approach does not permit to find the best configuration in a reasonable time, the selected optimization approach is based on the Quasi-Monte Carlo algorithm, and is illustrated in Figure 5.2. The idea is to generate a sample of $N \times 9$ random numbers between 0 and 1 using the Halton sequence generation. The random parameters are then generated at each iteration from the lower and upper bounds values, and the code indicates the force ratio computed and if the configuration is acceptable regarding the constraints. If this is the case, the parameters are saved in an array structure. The next iteration comes next and reiterate the same process until the N vector of points have been considered.

The post-processing starts then with the reading of the overall array structure that keeps in mind every sequence of parameters acceptable from the early stage of the code development. Each recently saved configuration is evaluated with a rounding of each length parameters (rounding to the millimeter) and for each angle (rounding to the degree). The idea of this step is to verify the configuration is still compliant with the constraints after a slight perturbation of its parameters. The compliant configuration are added to the overall array structure. Finally, a loop over the overall array is identifying the most promising families of configuration and build a set of parameters that will be injected to the `surrogateOpt` algorithm that should return the optimum configuration. Again, at the end of this last step, a rounding should be made to ensure the optimum configuration remains compliant with the constraints.

5.2 HDRM Optimization

The optimized HDRM configuration parameters provided by the optimization process are presented in Table 5.1. This configuration is obtained by selection from the entire data set of acceptable solutions and `surrogateOpt` converges also to this solution. One can note that the angle ψ equals 1, but for simplicity of the future assembly it will be set to 0 because it does not vary significantly the final force ratio either the linear path geometry.

	L_{OD}	L_{OA}	L_{AB}	L_{BD}	L_{BC}	L_{OF}	η	γ	ψ
Opti	51	26	21	20	23	46	120	293	$1 \rightarrow 0$

Table 5.1: Optimized configuration parameters: lengths in mm, angles in deg.

On Figure 5.3, the configuration has a large margin of angular amplitude after the minimum angular amplitude required to reach (point green). Since the closed configuration is a singular point of the mechanism (points A, B and D aligned), the closed angle should be slightly smaller to ensure the motion will start in the expected direction. This should not be a problem since the angular range provided is large enough to be able to release safely the HDRM. This will be reassessed during the CAD modeling of the optimized configuration.

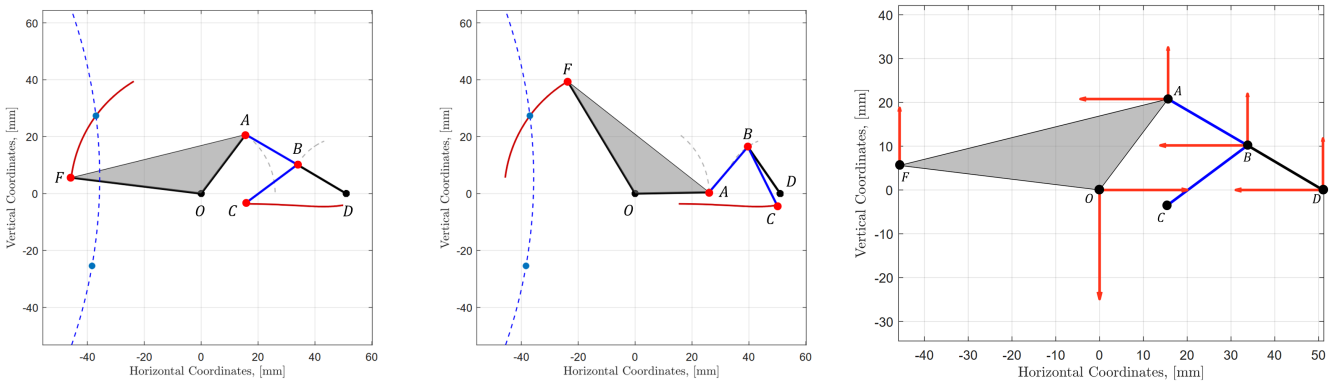

(a) Kinematic motion (closed and opened). (b) Static equilibrium.

Figure 5.3: Optimized configuration geometry overview based on the analytical code.

Finally, the static equilibrium at closed configuration is presented in Table 5.2. The load on the point A is the load applied by the lever on the knee (negative for the knee equilibrium, positive for the lever); the load on the point B is applied by the lever on the leg (positive on the lever equilibrium, negative for the leg); the load on point C is the load applied by the actuation transmission to the lever; the loads on the points O and D are the loads applied by the fixed hinge to the knee and the leg respectively; the load on the point F is the load applied by the cover lever to the knee. One can see that the static equilibrium is assessed on every single piece of the HDRM.

Points	$\hat{x}$ [kN]	$\hat{y}$ [kN]	**Resultant** [kN]
O	+3.809	−4.739	6.080
A	−3.809	+2.239	4.418
B	−3.787	+2.239	4.399
C	−0.022	+0.000	0.022
D	−3.787	+2.239	4.399
F	+0.000	+2.500	2.500

Table 5.2: Analytical static equilibrium in closed configuration.

The force ratio achieved by this optimized configuration is $F_{\text{ratio}} = \frac{F_C}{F_F} = 0.009$. This is possible because most of the force is transmitted to the fixed hinge in D.

5.3 Conclusion

To conclude this section, the current parametric model of the HDRM, and the associated design constraints makes the optimization process difficult since the problem is highly non-linear. The usual global optimization solver such as `GlobalSearch` or `Multistart` are not well-suited to solve such problem. The local solver `fmincon` could be used by considering variation within the domain defined by the dimensional boundary conditions, but since the parametric model is described by 9 different parameters, it would take too much time to compute. A pseudo-probabilistic approach has been considered with the Quasi-Monte Carlo algorithm. The Halton sequence is used to generate a large set of low-discrepancy parameters between the boundary conditions. This permits to reach an acceptable optimum in a reasonable computation time.

The optimized configuration has been validated even after some rounding of the parameters to ensure the configuration is still acceptable even if it slightly moved, and for cost reasons (the more accurate, the more expensive it is). The angle ψ has been set to 0 instead of 1 for future assembly simplicity.

Finally, for the static equilibrium, the force ratio achieved is 0.009 and the maximum load computed in closed configuration is at the fixed hing of the knee piece, which has a resultant of 6.1 kN. This will be important for the bearing dimension and the material selection since it would produce a large contact pressure stress at this hinge.

Chapter 6

Conceptual Design

6.1 Material Selection

The material selection of the main pieces of the mechanism is straightforward. Since the cryostat, and filter interface of the DEA and the baffle will be constituted of aluminum (6061-T6 alloy), the material of the door mechanism (cover and HDRM) should also be the same aluminum. The reason is the thermal expansion due to the variation of temperature both during the tests sequences and the operational phase will cause the piece to shrink. In order to avoid the addition of thermal constraints due to difference of shrinking or to thermal cycling, the same aluminum will be used for the main pieces of the HDRM and the cover.

However, metal-to-metal contact should also be avoided, in order to prevent cold welding. The materials of the component such as screws, pins, hinges, and any other small piece that fulfills similar function should be selected. At the same time, the materials selected should be able to withstand significant loads (typically $4 \rightarrow 6\,\text{kN}$). The backlash dimensioning is also critical, to ensure the mechanism will be able to move at cryogenic conditions.

Therefore, this section aims to provide a materials selection for bearings and washers that should constitute the articulations of the HDRM. Hence, it will first present the thermal behavior of the aluminum 6061. Then, a comparison of different compatible (matching nearly the coefficient of thermal expansion of the aluminum) materials for these components and discuss their general properties. Moreover, friction coefficient should also be low enough to mitigate the frictional loads to avoid reaching important actuation force including ECSS margins. Finally, the contact at the bearings will be theoretically modeled using the *Hertzian Stresses* theory to assess the load applied to some materials is not deforming plastically the component.

6.1.1 Aluminum 6061 Thermal Behavior

Since the main pieces of the mechanism will be made of aluminum 6061-T6 alloy, the thermal expansion at 50 K will be critical in the choice of materials and in the backlash dimensioning. Figure 6.1a shows the evolution of the coefficient of thermal expansion of the aluminum 6061 using the experimental data[1] from Arp et al. [60] in the full blue line, and the linear approximation based on the CTLE (acceptable between 218 and 373 K) provided by Dunn et al. [61] in dashed line. Figure 6.1 shows also the comparison between the aluminum linear CTE and Vespel materials equivalent one.

The CTE decreases with the temperature meaning that it is not constant with temperature. Consid-

[1] The curve fitting performed is based on the empirical equation provided by the National Institute of Standards and Technology (NIST), which references Arp. et al. as the source of experimental data (URL Link: `https://trc.nist.gov/cryogenics/materials/materialproperties.htm`).

ering a variation of temperature from room temperature (293 K) to 50 K, temperature dependent CTE should therefore be considered to assess the thermal contraction of the aluminum pieces of the mechanism. Since no reliable data have been found, the linear CTE at room temperature will be used for different materials compared to the (rough) approximation of the aluminum 6061 to have an order of magnitude of the behavior of a material to elongate more or less than the aluminum. This remains a limitation of the current conceptual design.

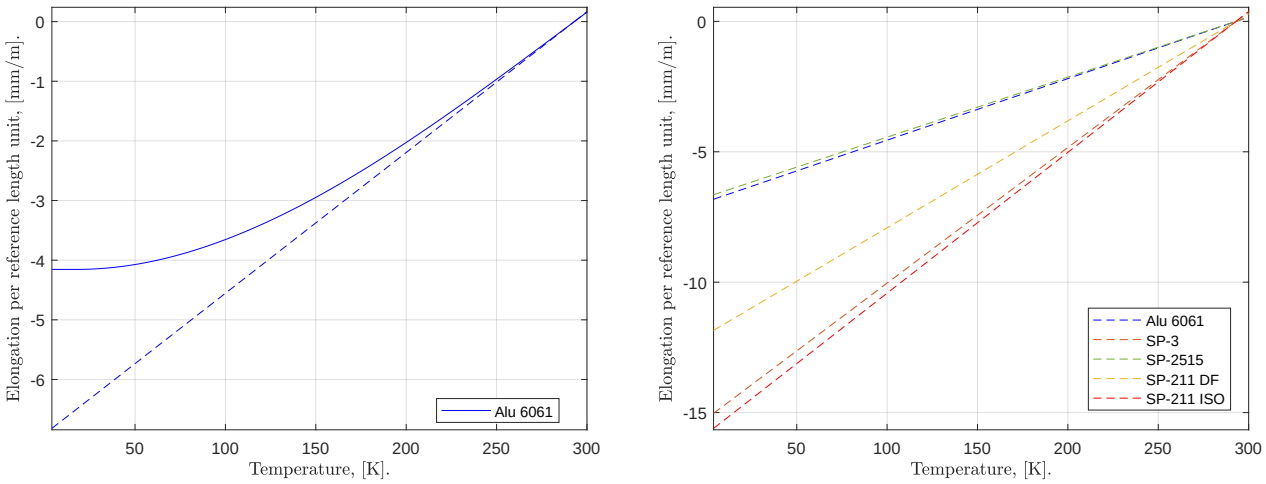

(a) Al 6061. (b) Vespel materials.

Figure 6.1: Length variation per reference length unit due to temperature gradients for (a) Al 6061 and (b) Vespel materials.

6.1.2 Hertz contact stresses

The HDRM is constituted of 3 moving pieces: the knee, the lever and the leg. Each piece is linked each other by pins. It is critical to ensure the material constituting these articulations will not be damaged due to high contact pressures during the static phases. ECSS standards recommend to consider the worst case for such considerations [11]. The stress at the mating surfaces of curved bodies in compression are called *Hertz contact stresses*. The theoretical contact between curved surfaces is generally a point or a line. Even these contact areas are small due to deflections, the corresponding compressive stresses could be high such that fatigue failures tend to be produced [5, 62]. Figure 6.2 shows the usual geometry for cylinder-cylinder contacts adopted in the literature.

The maximal contact pressure between a cylinder and a cylindrical groove is expressed by Shigley et al. [6] as follows:

$$p_{\max} = \frac{2F}{\pi b \cdot L} \text{ with } b \equiv \sqrt{\frac{2F}{\pi L} \cdot \frac{\frac{1-\nu_1^2}{E_1} + \frac{1-\nu_2^2}{E_2}}{\frac{1}{d_1} \pm \frac{1}{d_2}}} \tag{6.1}$$

where b the contact modulus (or half contact width) expressed in m, ν is the Poisson's ratio (dimensionless) of both contacting bodies 1 and 2, d is their diameter[2] expressed in m, and E is their Young's modulus expressed in Pa, F is the load applied to the bodies expressed in N and $L = 20\,\text{mm}$ is the contact length.

[2]The $+$ sign is considered in the case of cylinder-cylinder contact, while the $-$ sign is considered for cylinder-cylindrical groove contact. Hence, the $-$ sign is considered in this case.

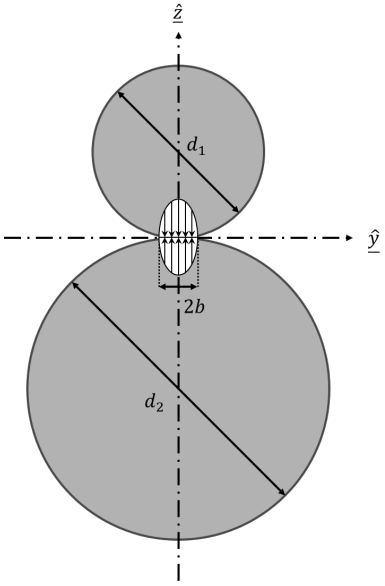

Figure 6.2: Hertz contact stress geometry for cylinder-cylinder contact, adapted from [5, 6].

Vespel S-line Materials

The Vespel S-Line materials have promising candidate materials, such as the SP-211 for its low friction coefficient, the SP-3 which is designed for vacuum friction application in bearings typically and the SP-2515 because of its matching coefficient of thermal expansion with the aluminum one [12].

Table 6.1: Vespel materials properties for different composition, provided by DuPont [12].

Properties [Units]	**SP-3**	**SP-2515**	**SP-211**	
	ISO	DF	DF	ISO
Young's Modulus [MPa]	3275	6340	–	–
Poisson's Ratio [MPa]	0.35	–	–	–
Compressive Stress [MPa]				
at 1% strain	34.5	–	14.5	20.7
at 0.1% offset	–	–	27.6	37.2
Friction coefficient [–]				
static	–	–	0.20	0.20
$PV = 0.875\,[\text{MPa} \cdot \text{m/s}]$	0.25	0.21	0.12	0.12
$PV = 3.5\,[\text{MPa} \cdot \text{m/s}]$	0.17	0.33	0.08	0.08
Coefficient of linear expansion $[10^{-6}\text{K}^{-1}]$	52	23, (54)[a]	41	54

[a] The measure in parentheses corresponds to the measured value parallel to the forming direction. All the other direct-formed (DF) properties are measured perpendicular to the forming direction.

Table 6.1 summarizes relevant properties of different type of Vespel materials. The suitability of a material for a bearing application is evaluated using the PV measure, which stands for pressure (P) and sliding velocity (V) [12]. It determines the limit of a material to deal with friction loads. The failure point is usually manifested by an abrupt increase of wear rate of the bearing material.

One can note that the datasheet provided by DuPont is not complete, particularly for cryogenic conditions. The coefficient of friction, as well as all the other properties of each material are subjected to more or less variation in cryogenic conditions that could be critical for the design. Therefore, this remains

uncertain at this stage of the design, and experimental tests sequence should be performed to validate their behavior at cryogenic temperature and to estimate their properties in such environment.

Figure 6.1b shows the length variation in millimeter per unit of meter due to thermal expansion of the Vespel material candidates considered for the bearings, compared to the CTE of the aluminum. Even if the variation values are not representative of the reality, the variation length are estimated by considering the aluminum one for which an empirical curve is available, multiplied by the CTE ratio of the aluminum with the compared Vespel material. This assumes that each material behavior at cryogenic conditions is likely similar to the aluminum.

Considering the (rough) approximation on the CTE (assumed constant), the SP-2515 has the closest thermal behavior to the aluminum in only one direction. Indeed, this material has not isotropic properties. Since the CTE is nearly the same for the other direction than the other materials, the manufacturing process should be carefully considered to only have this larger expansion of the material in the direction of the height axis of the cylinder in order to avoid too much backlash at cryogenic conditions.

Table 6.2: Contact stress evaluation between Vespel SP-2515 and aluminum for different configurations.

	Hertz pressure, $p_{\max}$ [MPa]	**Contact width**, $2b$ [mm]	**Von Mises stress**, σ_e [MPa] SP-2515	Al 6061
$M08$[a], $L = 20$[b]	51.10	7.47	27.64	27.98
$M16$, $L = 20$	33.28	11.5	18	18.22
$M24$, $L = 20$	21.21	18	11.47	11.61
$M08$, $L = 40$	44.63	4.28	24.14	24.44
$M16$, $L = 40$	22.45	8.5	12.14	12.29
$M24$, $L = 40$	15	12.7	8.11	8.21

[a] The bearing diameter is noted MXX with M is the thread metric designation and XX indicates the nominal diameter in mm.
[b] The length $L = 0.020\,\text{m}$ is the height of the contact cylinder.

However, since polyimide materials such as Vespels have low Young's modulus, they are subjected to deform plastically more easier than metals. According to Table 5.2, the maximal load within the bearing reaches 6 kN, with is certainly too much for such materials. The maximal contact pressure is computed considering the SP-2515 materials for different diameter and bearing lengths. Table 6.2 presents the results with the Von Mises stresses of the Vespel bearing and the aluminum bore, the Hertz maximal pressure and the contact width $2b$ estimated. One can see that for the smaller diameter of bearing the contact stress is greater the compressive maximum stress. Even for wider diameters and longer bearings, the bearing load is such that the contact width is usually estimated on half the diameter, meaning that the material is already deforming plastically. Therefore, it appears that the Vespel materials for bearings are too soft to handle the bearing loads provided by the HDRM.

Bronze Alloy Materials

Bronze alloys are copper alloys in which the major addition is neither zinc nor nickel (most commonly aluminum, silicon, lead, tin) [13]. Different bronzes are usually produced for different applications:

- Tin (Cu-Sn-P) bronzes (C50100[3], C52480, etc.) are used as strip for electrical products, corrosion-resistant bellows, diaphragms and springs washers.

[3] Under the Unified Numbering System (UNS) for Metals and Alloys, coppers and copper alloys are designated by five-digit

- Leaded (Cu-Sn-P-Pb) tin bronzes (C53400, C54400, etc.) are frequently used for sleeve bearings, thrust washers, cam followers and similar parts.

- Aluminum (Cu-Al) bronzes (C60800, C64210, etc.) have a very wide range of applications, from marine hardware, shaft and pump to valve components for handling seawater, heavy-duty sleeve bearings and machine-tool ways.

- Silicon (Cu-Si) bronzes (C64700, C66100, etc.) are used for hydraulic fluid lines, high-strength fasteners, wear plates, and marine and pole-line hardware.

The common properties of these copper alloys is that they have a high strength, good fatigue resistance, easily machinable and have excellent corrosion resistance. They might have a relatively high strength-to-weight ratio and usually requires a reliable lubrication.

The following part aims to discuss about potential bronze alloy candidates for the HDRM bearings. In order to do that, bronze alloy taken from the main classification family presented above will be considered, and other copper alloy (beryllium-copper and nickel-aluminum bronze for their use in aircraft's landing-gear bearings) will be compared and a selection will be made if they are compliant with the requirements.

The requirements for this preliminary selection states that the bearing material should not plastically deform under the Hertz contact stress computed for the worst-case bearing load (6 kN). Consequently, its contact width should not be too large ($< 25\%$ of the bearing diameter). The thermal behavior should be close to the aluminum's thermal behavior to avoid mismatch after cooling to 50 K. The density is also considered and should be minimized as much as possible.

Copper Alloy	**Young's Modulus** [GPa]	**Yield Strength** [MPa]	**Poisson Ratio** [−]	**Density** [kg/m^3]	**CTE, linear** 10^{-6} [/K]
C51100	110	552	0.341	8860	17.8
C52480	110	710	0.330	8770	18.4
C54400	103	434	0.321	8890	17.3
C60800	121	185	0.325	8170	18.0
C64200	110	241	0.330	7700	18.0
C17200	130	205	0.300	8250	17.0

Table 6.3: Thermo-mechanical properties of different copper alloys, from Davis et al. [13].

Table 6.3 presents some thermo-mechanical properties of copper alloys that could be used in bearings. The C51100 and C52480 are Tin bronze alloys; the C54400 is a leaded tin bronze alloy; the C60800 and C64200 are aluminum bronze alloys; and the C17200 is a beryllium-copper alloy (used in landing-gear bearings).

Considering first a bearing length of 10 mm, all the candidates have a contact width that is above 25% of the bearing diameter (even for a 24 mm diameter bearing). On the other hand, if a bearing length of 30 mm, all the candidates are acceptable. Since the yield strength is provided and not the compressive strength, this last bearing length will be considered for the bearings. Therefore, since the linear CTE of

numbers preceded by the letter *C*. The five-digit codes are based on, and supersede, an older three-digit system developed by the U.S. copper and brass industry. The older system was administered by the Copper Development Association (CDA), and alloys are still sometimes identified by their *CDA numbers*. The UNS designations are simply two-digit extensions of the CDA numbers to accommodate new compositions [13]

the aluminum equals $23.6 \cdot 10^{-6}$ K^{-1}, the copper alloy considered that have the linear CTE the closest to the aluminum is the C52480 Tin bronze alloy.

6.1.3 Bearing Materials

Considering the C52480 Tin bronze alloy as bearing material (M08, bearing length of 30 mm), the Hertz maximal contact pressure computed by Equation 6.1 equals 135.8 MPa for a contact width of 1.87 mm, for the worst case of bearing load (6 kN). The volume of one bearing is $1.5 \cdot 10^{-6}$ m^3, and the estimated mass of this component equals 0.013 kg.

To avoid metal-to-metal contact between the bearings and the aluminum pieces, coatings should be considered. Particularly, the friction coefficient between the coating and the hole should be as small as possible since it effects directly the actuation force required by the HDRM.

Lubrication

Lubrication is probably not interesting in this application. The first reason is that the HDRM is moving relatively slowly and for a short time. Since the HDRM should move at room temperature for the enclosure and at cryogenic temperatures for the release phase, and for contamination reasons, liquid lubricant should be prohibited [31]. Solid lubricants could be used if necessary. One can imagine using a small layer of Vespel between the bronze bearings and the aluminum holes. This could also solve the metal-to-metal contact problem. However, this has to be considered in more details in further analysis and remain a limitation of the current conceptual design.

6.1.4 Washer Materials

The washers should be placed between on the articulation of the HDRM, between each piece to avoid metal-to-metal contact. Since the loads in this direction (perpendicular to the HDRM plane considered for the parametric model), and because of friction should be minimized with the aluminum, Vespel materials are considered for this application. In particular, the SP-2515 is selected because of its linear CTE which match the aluminum one.

6.2 Tolerance Dimensioning

Dimensioning backlashes within the HDRM is critical since it should operate both at room temperature (for the enclosure) and at cryogenic conditions (for the opening). The tolerance dimensioning process is based on the ISO286-1 norm [7].

Figure 6.3 describes the geometry of tolerance principles. The upper tolerance limit (SE, se) is defined as the difference between the maximum diameter allowable and the nominal diameter (represented by the dashed red vertical line. The lower difference limit (IE, ie) is defined as the difference between the minimum diameter and the nominal diameter. Capital letters are used to define holes related quantities while the small letters are used for the shaft related quantities.
Different classes of tolerance modes are possible, with different degree available depending on the accuracy targeted. Figure 6.4 shows the tolerance interval placement with respect to the nominal dimension for the shafts and the holes. For example, 16 B 11 corresponds to a nominal diameter of 16 mm, with a tolerance interval positive for the hole and negative for the shaft, and a quality level of 11 (around 110 µm of accuracy). The quality level of the tolerance is provided by tables from [7].

The actual tolerance problem involves a huge thermal contraction and requires therefore a large backlash

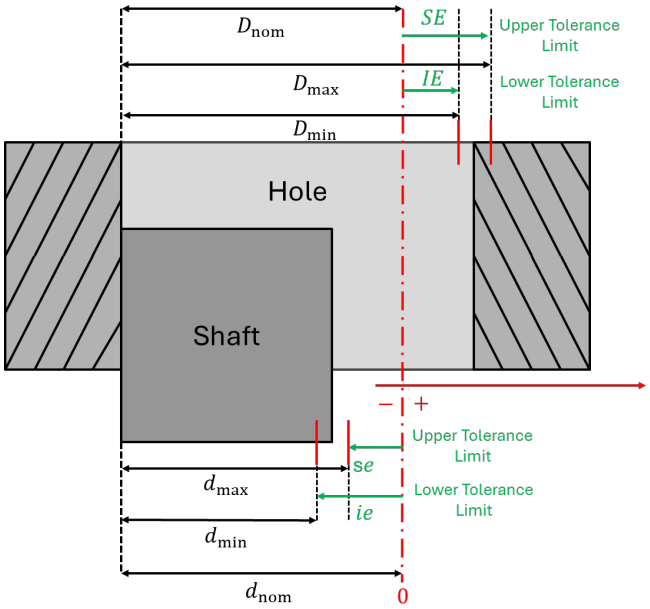

Figure 6.3: Tolerance geometry definition, based on the ISO 286-1 norm [7].

to ensure the mechanism will operate. Since the bearings nominal diameter is 8 mm (M08), the tolerance interval placement for the shafts are *c* or *d* and for the holes is *H*. The available degree of accuracy are 9 (around 36 µm for 8 mm diameter) and 11 (around 90 µm for 8 mm diameter).

Shaft	**Tolerance**	
	Upper Limit, [µm]	**Lower Limit**, [µm]
*c*11	−80	−170
*d*9	−40	−75
*d*11	−40	−130

Table 6.4: Shaft Tolerances Intervals.

Hole	**Tolerance**	
	Upper Limit, [µm]	**Lower Limit**, [µm]
*H*9	+90	0
*H*11	+36	0

Table 6.5: Hole Tolerances Intervals.

The bronze thermal behavior is not known at 50 K. The linear CTE ($18.4 \cdot 10^{-6}$ K^{-1} is accurate for room temperature (at which the measure has been taken). However, the linear CTE at room temperature of the aluminum provided by Dunn et al. [61] enables to roughly approximate the thermal contraction of the bronze at 50 K with respect to the contraction of the aluminum:

$$\textbf{Al 6061: } -4.073\,\text{mm}\,\text{m}^{-1} \rightarrow \textbf{C52480: } \sim \frac{\text{CTE}_{\text{C52480}}}{\text{CTE}_{\text{Al 6061}}}(-4.073)\ \text{mm}\,\text{m}^{-1} = -3.175\,\text{mm}\,\text{m}^{-1} \quad (6.2)$$

The bronze material should approximately contract less than the aluminum. Hence, the backlash of the bearings should be small at room temperature in order to avoid too large backlash at cryogenic temperatures. The tolerance chosen will therefore be *H*11 for the hole and *d*9 for the shaft. Figure 6.5 shows the geometry of this thermo-tolerance problem.

Therefore, the shafts' nominal diameter being 8 mm, the associated tolerance interval is $[7.925, 7.96]$ mm. For the holes, the associated tolerance interval is $[8, 8.036]$ mm. The maximum backlash possible equals 111 µm at room temperature.

At cryogenic temperatures, the shafts and holes are contracting and their dimensions are varying:

- **For the shafts** (in bronze):

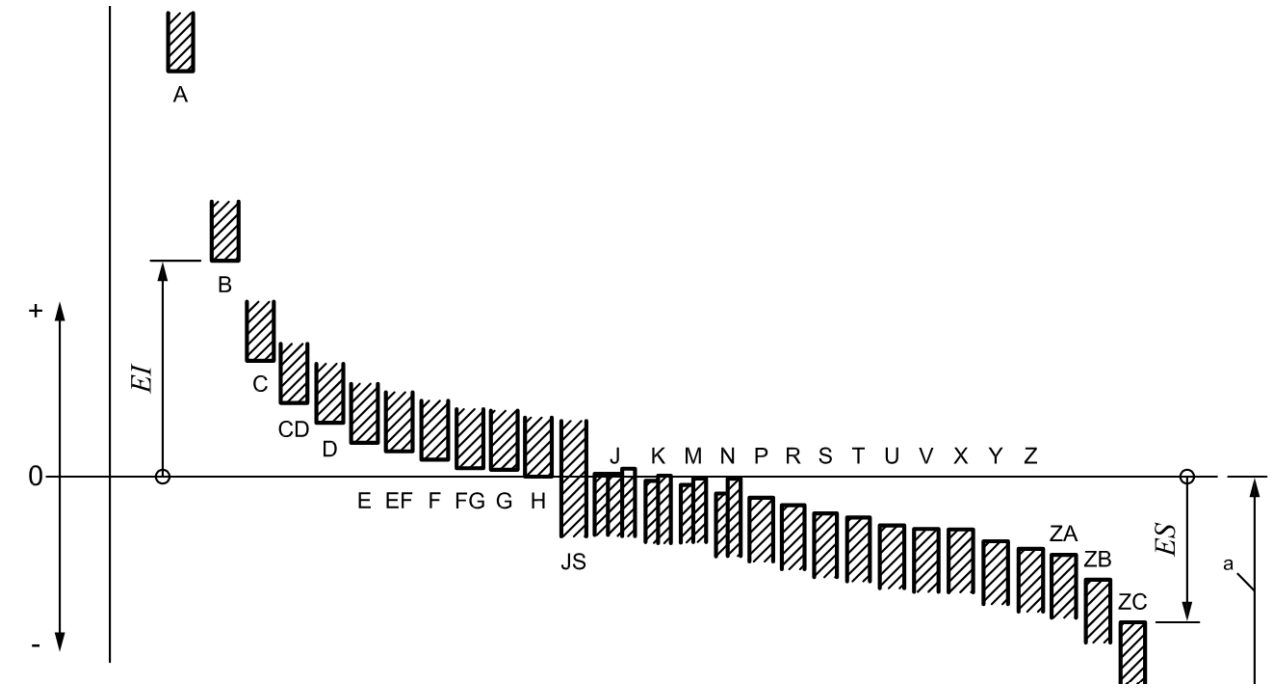

(a) Holes (internal features of size).

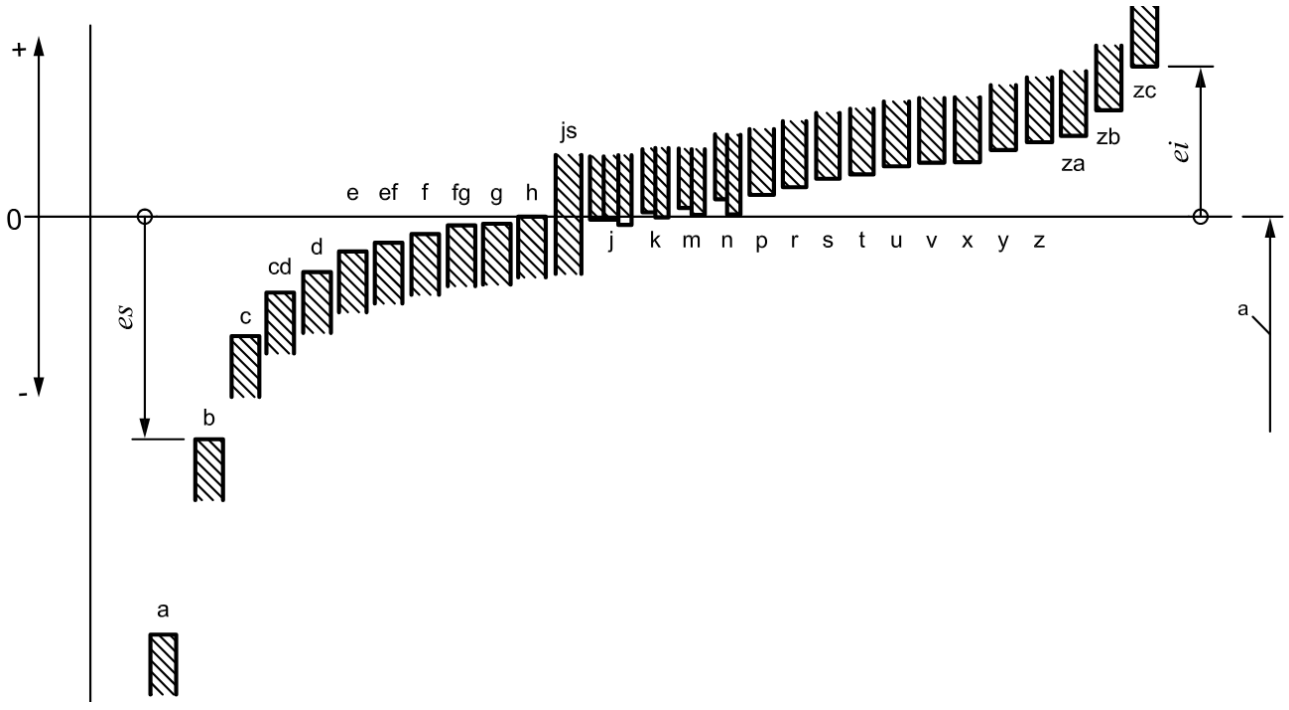

(b) Shaft (external features of size).

Figure 6.4: Schematic representation of the placement of tolerance interval with respect to the nominal diameter, adapted from [7].

- Its length at 50 K should contract by $30 \cdot 10^{-3} \cdot -3.175 = -95.25\,\mu m$.
- The associated tolerance interval equals $[7.899, 7.935]$ mm.

- **For the holes** (in aluminum):

- Its length at 50 K should contract by $30 \cdot 10^{-3} \cdot -4.073 = -122\,\mu m$.
- The associated tolerance interval equals $[8.122, 8.158]$ mm.

The maximum backlash possible equals 259 µm at cryogenic temperature.

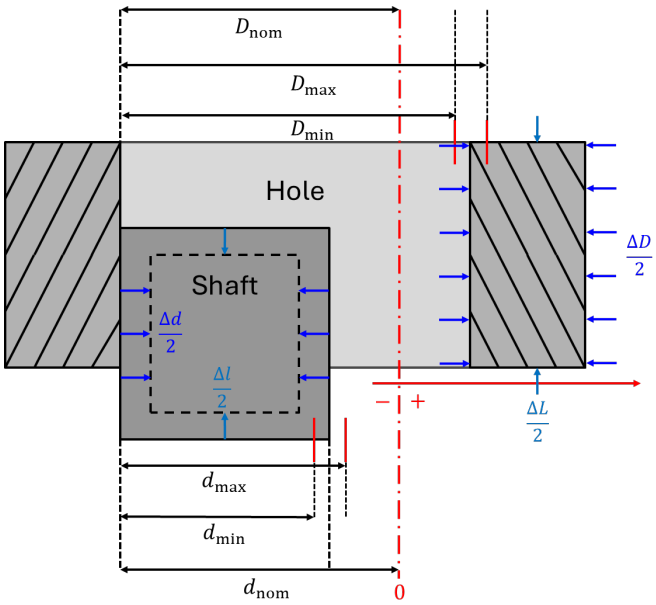

Figure 6.5: Thermal contraction problem in the tolerance geometry.

The backlash difference between room and cryogenic temperatures is significant. This could introduce some relaxation of the HDRM that could lead to a loss of tightness of the gasket. However, since the sealing is only important during the ground operations and the launch lock, this relaxation is not really a problem.

The overall end-to-end backlash of the mechanism may be estimated. The idea is to evaluate how much the point C moves without F starts moving. The link considered are the points C, B and A, with the contact point F. The knee and the lever are assumed isotropic, meaning that the components are considered to retract uniformly on their whole surface. The maximum backlash being 259 µm at 50 K, the point C moves without F starts moving by $2 \times 0.259 = 0.5$ mm.

Finally, the tolerance computation provided here are provided assuming that the bronze has an analogue behavior as the aluminum at 50 K described in Figure 6.1a. In addition, the materials are assumed uniformly constituted in such way that the CTE of each material is the same in every direction considered. In reality, the materials may more or less contract in a given direction due to crystalline defects or other impurity that could modify the thermo-mechanical behavior of the components. These assumptions are limiting the quality of the computation of this section and the backlash remains uncertain at this stage of the design.

6.3 Actuation

The design static forces being estimated for the vibration test sequence (driving mission phase), the actuation torque can be computed according the the ECSS Standards [11]. The mission phases considered for the release are the space-orbit release sequence and the release tests that will be performed during the AIT.

6.3.1 Actuation Force

The actuation torque required to release the knee from the cover lever is computed by considering the ECSS Standards, with the theoretical factors described in Table 3.1 in Section 3.3.

The spacecraft nor the payload are not spinning and the resistive inertial force I can be neglected. In addition, the current design does not include any springs and adhesion phenomena are considered avoided since no metal-to-metal contacts are considered and is not subjected to any magnetic effect nor hysteresis. Equation 3.6 is rearranged as follows, but for the actuation force formulation:

$$\begin{aligned} F_{\text{min}} &= 2 \cdot \left(1.1 \cdot \cancel{I} + 1.2 \cdot \cancel{S} + 1.5 \cdot \cancel{H_M} + 3.0 \cdot F_R + 3.0 \cdot \cancel{H_\gamma} + 3.0 \cdot \cancel{H_A} + 3.0 \cdot \cancel{H_D}\right) + 1.25 \cdot F_D + \cancel{F_L} \\ &= 2 \cdot (3.0 \cdot F_R) + 1.25 \cdot F_D \end{aligned} \tag{6.3}$$

where F_L is neglected since no deliverable output force is specified by CNES and H_A is also neglected since no additional effect are considered.

Inertia Force

The HDRM is geometrically small compared to the cover assembly. The inertia torque was completely negligible for the cover assembly (it has not significant effect on the actuation torque computed in Section 3.3). For the HDRM, the inertia resistive force is assumed negligible.

Regarding the acceleration profile, a maximal angular range of 29 deg should be covered to completely release the knee. Assuming also a sinusoidal acceleration profile and considered the HDRM should be released within $\Delta t = 30\,\text{s}$, the maximum acceleration is computed as follows:

$$\ddot{\theta}(t) = \frac{\Delta\theta}{2}\left(\frac{\pi}{\Delta t}\right)^2 \cos\left(\frac{\pi t}{\Delta t}\right) \Rightarrow \ddot{\theta}_{\text{max}} = \frac{\Delta\theta}{2}\left(\frac{\pi}{\Delta t}\right)^2 = 0.0028\,\text{s}^{-2} \tag{6.4}$$

Friction Force

The static loads to be applied by the actuator at point C equals 22 N as presented in Table 5.2 in Section 5.2. Since the worm-screw of the actuator is made of stainless-steel, the nut is also assumed to be in stainless-steel in order to avoid backlash problems at cryogenic temperatures. The friction between stainless-steel and aluminum is taken from Sandborn et al. [63] and assumed equal to 0.45. The friction force is computed as follows:

$$F_F = (\mu_s F_C) \cdot \frac{d}{2} = 39.6\,\text{mN} \tag{6.5}$$

where F_C is the static load at point C of the HDRM and d is the diameter (M08) of the bearing interface between the nut and the HDRM lever.

Actuation Force

From Equation 6.3, the actuation force required to be applied at the point C equals $F_{\text{min}} = 237.6\,\text{mN}$ to tightens the gasket during the enclosure.

6.3.2 Actuator Choice

The actuator choice will probably be a PhySpace stepper motor from Phytron Gmbh [39]. However, the worm screw and the nut, assumed in stainless steel until now, requires to be correctly designed. The position of this screw should be made to fit the average linear axis of the linear path (which is not perfectly

aligned with the horizontal axis. An angle of 2.5 deg should be considered to have the smallest errors with respect to the linear axis (-0.159 mm below and $+0.141$ mm). This will be one of the requirements for the integration of the future structure that should interface the baseplate, the HDRM and the cryostat. This remains a part of the future work to be achieved.

6.4 Conclusion

To conclude this conceptual part, the thermal behavior of the aluminum constituting the major pieces of the HDRM have been considered for the materials selection of the bearings and the washers. The tolerance design has then be considered to ensure the mechanism is not contracting too much at 50 K. Finally, the actuation force required for the HDRM have been computed according to the ECSS standards.

At this stage of the design, the current iteration is not including the design of the actuation part. This concerns the nut, the worm screw shaft, the gearbox if required and the stepper actuator. However, this chapter provides the main requirements for their integration to the design of the mechanism. In addition, the bearings' design is not complete since metal-to-metal problem between the bronze and the aluminum should be avoided. This could be investigated with the potential used of solid lubricant such as Vespel or other materials. Finally, due to uncertainties of the thermal properties of each component designed, the actual configuration may vary after further more detailed thermo-mechanic analysis.

Chapter 7

Design Analysis

This section aims to present the features of the final iteration of the conceptual design and its weaknesses. Indeed, at this stage of the design, the cover cryo-mechanism is not completely designed yet, and this section should present what should be achieved to complete it. A motion analysis is also presented to ensure the kinematics constraints (angular range wide enough to open the cover assembly without collision, linear path at actuation point) are satisfied. A preliminary finite element method (FEM) analysis is finally discussed to enforce the static performances computed previously.

7.1 HDRM Conceptual Design

7.1.1 CAD Model

The overall CAD model of the actual conceptual design is presented in Figure 7.1. The cover assembly is not completely displayed: only the door, the lever and the actuator with its shaft are presented, and the baseplate geometry because they are interfacing the HDRM design.

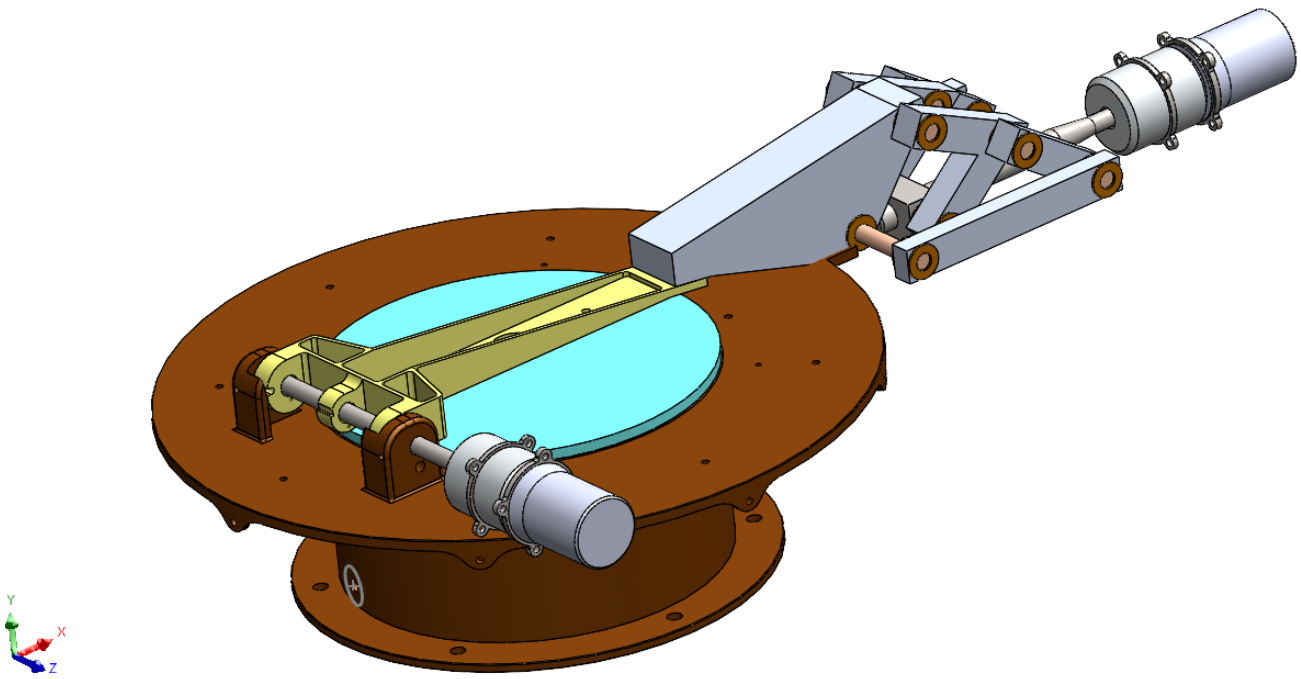

Figure 7.1: Overview of the actual DEA door cryo-mechanism design.

Figure 7.2 describes more specifically the different components constituting the HDRM design. The major pieces of the HDRM are the knee piece which is contacting the cover lever, the 2 levers and the 2 legs. The bronze bearings and the Vespel washers are also presented. The actuation part comprises the nut and the worm screw shaft (both in stainless steel), the gearbox and the stepper motor. The 2 fixed pieces are presented as a future interface for the structure part that should sustain the HDRM with the DEA. Indeed, the entire mechanism should remain fixed at some point to the cryostat and the baseplate.

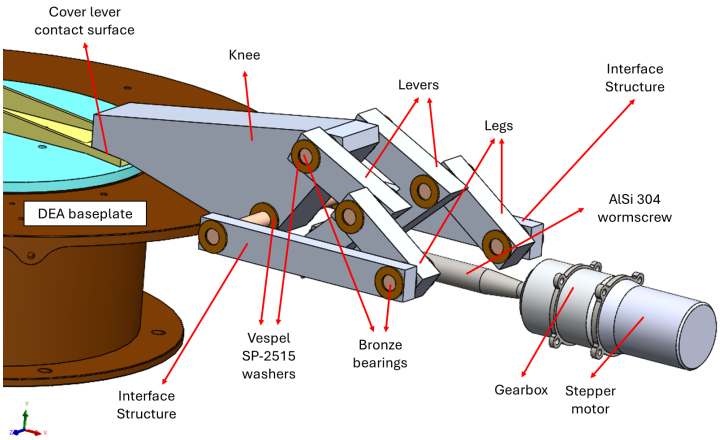

(a) Trimetric view of the HDRM design.

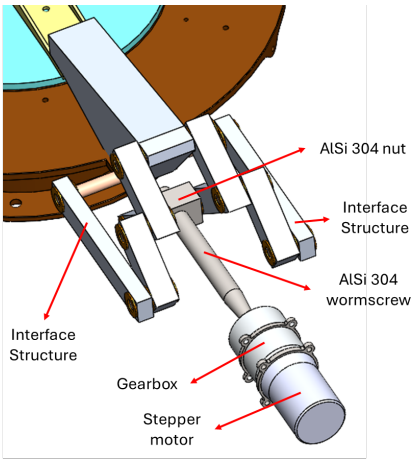

(b) Upperside view of the HDRM design.

Figure 7.2: Description of the actual conceptual HDRM design.

The duplication of the lever and the leg pieces is made to provide more resistance to the loads during the enclosure and the launch lock phases and it ensures the symmetry of the loads distribution. The knee could therefore no slip away from the lever.

7.1.2 Mass Budget

Table 7.1 presents the mass budget of the actual HDRM design. The gearbox mass is not evaluated and assumed integrated in the motor's mass. Margins of 20% are considered all new parts designed. The overall mass of the HDRM equals 1.32 kg. Considering that the cover assembly's mass equals 0.24 kg from the CAD model, the overall mass of the DEA door cryo-mechanism equals 1.56 kg. This is huge since the initial weight was evaluated around 1 kg including the baseplate and the baffle. The HDRM main mass contribution are the actuation assembly and the main HDRM pieces. While the actuator design should be achieved, the optimization of the mass of the HDRM pieces should be a part of the future work to be achieved.

7.1.3 Discussion

One can observe that actually this conceptual design is not complete and requires further more considerations. First, the structure integration to interface the DEA baseplate and the cryostat. This is probably the most significant part that requires analysis since the structure should be the lightest possible, interfacing the cryostat, the DEA and the HDRM without any restriction of its release motion. The structure should be compliant in vibration and not provide natural frequencies that could be critical during the launch and vibration tests phases.

Second, the articulation design is not completed since lubrication should be considered and the clamping of the bearings within the pins. Indeed, the bearings should stay within each articulation, even during the

Table 7.1: Mass budget of the actual HDRM conceptual design.

Parts	**Number**	**Materials**	**Volume**[a] [mm^3]	**Density** [kg/m^3]	**Mass** [kg]	**Margin** [%]	**Mass with** [kg]
Knee	1	Al-6061 T6	145598.66	2700	0.393	20	0.471
Lever	2	Al-6061 T6	45396.11	2700	0.122	20	0.162
Leg	2	Al-6061 T6	23864.07	2700	0.064	20	0.077
Motor[b]	1				0.211	20	0.253
Worm Screw	1	AlSi-304	13889.15	7930	0.111	20	0.133
Nut	1	AlSi-304	9398.94	7930	0.075	20	0.090
Long Bearing[c]	2	C-52480	6232.92	8770	0.055	20	0.066
Med Bearing	2	C-52480	3116.40	8770	0.027	20	0.032
Small Bearing	2	C-52480	2613.80	8770	0.023	20	0.028
Washers	26	SP-2515	3920.8	1420	0.006	20	0.007
TOTAL							1.319

[a] The volume expressed is the sum of the volume of each single components. The volume for the lever parts is twice the volume of a single lever piece.
[b] PhySpace 32-2 stepper motor from Phytron GmbH [39]. The gearbox is assumed integrated to this value.
[c] Each bearings is 8 mm nominal diameter. Long bearings are 62 mm long. Med bearings are 31 mm long. Small beagins are 26 mm long.

launch phase. A clamping method without restriction their rotation has not been yet considered.

Moreover, the actuation parts (worm screw shaft, nut, gearbox and stepper motor) require specific design analysis. Some requirements can be deduced from Section 6.3.2, such as the orientation angle with respect to the horizontal axis, or the minimal length of the shaft required. In addition, the mass of the HDRM pieces could be minimized. Clearly, regarding the mass budget in Table 7.1, the actual HDRM is heavier than expected, mostly due to the actuation group of components. Even if this last part's weight is reduced, the structure that should come around could raise even more the mass budget. This could be one of the major challenges for the future work on this conceptual design.

7.2 Preliminary Motion Analysis

The kinematic analysis aims to ensure the release of the knee is sufficient to enable the cover assembly to open without any collision. The position of the knee could vary from the parametric plane model to the *SolidWorks* CAD modeling since the piece had to be thick enough to handle the loads applied during the enclosure and the launch lock. The linear path is also investigated in order to check if the path does not vary too much. This could indeed be critical for the interface actuator-structure.

Figure 7.3 presents graphically the results of this preliminary motion analysis. The actuation time is not provided in this preliminary analysis since the actuation part of the HDRM needs to be designed. One can see that the angular range is sufficiently large enough to open safely the cover.

For the linear path variation, the maximal variation from the linear regression of the path equals:

- Above: 0.1147 mm;
- Below: 0.1479 mm.

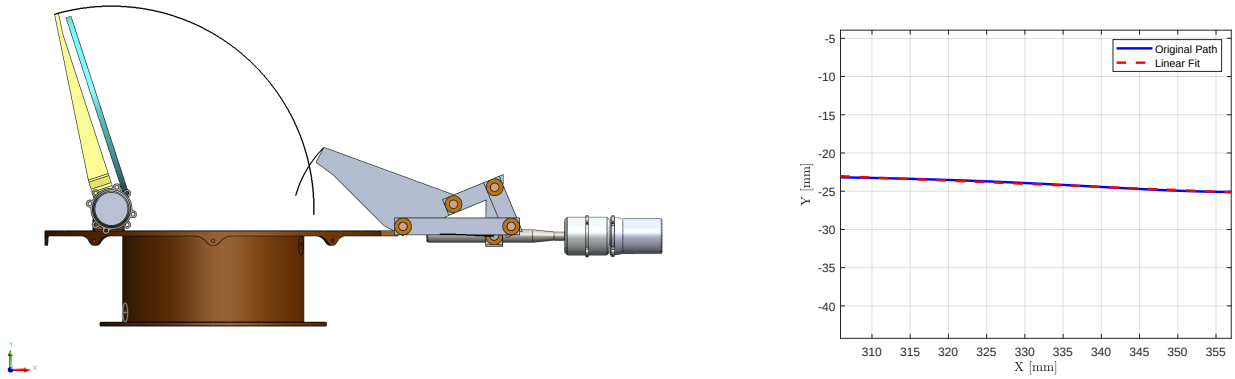

(a) CAD model overview.

(b) Linear path variation.

Figure 7.3: Overview of the conceptual design after the release motion simulation.

However, if the worm screw shaft is parallel to the horizontal axis, the vertical difference reaches 1.92 mm (between the lowest point and the highest point). The actuator shaft should be oriented by 2.36 deg downward to reach the linear path targeted. This accuracy is critical to avoid too large variations from the average linear path of the actuation point.

7.3 Preliminary Finite Element Analysis

7.3.1 Modeling

Figures 7.4 and 7.5 presents the FEM model set-up, shows the associated Von Mises stress, the resulting displacement and the equivalent strain results. The bearings are modeled using pins, and are numbered as shown in Figure 7.4. Since each pin has different parts, their name starts from *a* to *c* (for example, the pin 1 has a part *a* with the lever in front of the Figure, then a part *b* for the knee's part and then the part *c* for the lever behind it). Properties of the bronze that constitutes the bearings is not included to the analysis[1] The fixed parts have been slightly modified to enable to consider pin for the bearing of the point *O* of the HDRM. They are assumed fixed. The nut is also fixed, but along its central hole (where the worm screw should block any linear motion during the launch lock phase). The 2.5 kN load is considered applied at the contact surface of the knee and the cover lever.

7.3.2 Results Discussion

The Von Mises stress in deformed view is presented in Figure 7.4. One can see that the maximal value displayed is about 55.15 MPa. Since the yield tensile strength of the Aluminum 6061 T6 equals 276 MPa, the stress level is not high enough to reach the plastic deformation domain. One can note that the stress level is the highest on the upper lever parts and on the leg parts. This means that this configuration protects the actuation point from large stress level, and that the mechanism appears to fulfill its function of load deviation along the leg parts.

The displacement level of the mechanism is presented in Figure 7.5. The highest displacement occurs at the HDRM force contact area with 0.3 mm of displacement. The other pieces remain almost static except the upper part of the lever that is subjected to less than 0.1 mm. Since the highest load level occurs

[1] The bronze material C-52480 is not included in the default database of *SolidWorks*. If it could be included to the software in the professional version, the student version does not include this functionality. A General bronze have been considered then.

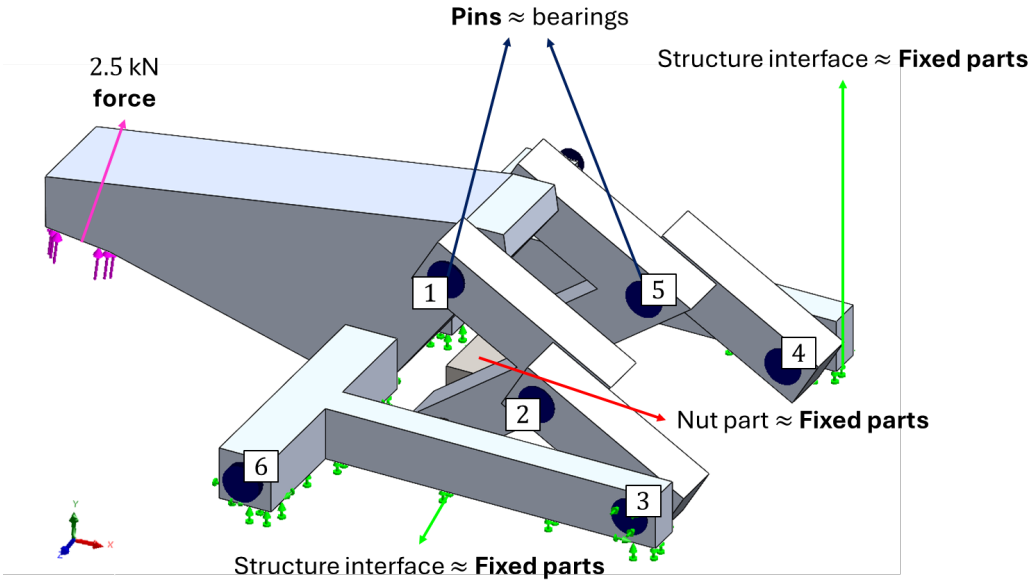

(a) FEM Preliminary Model.

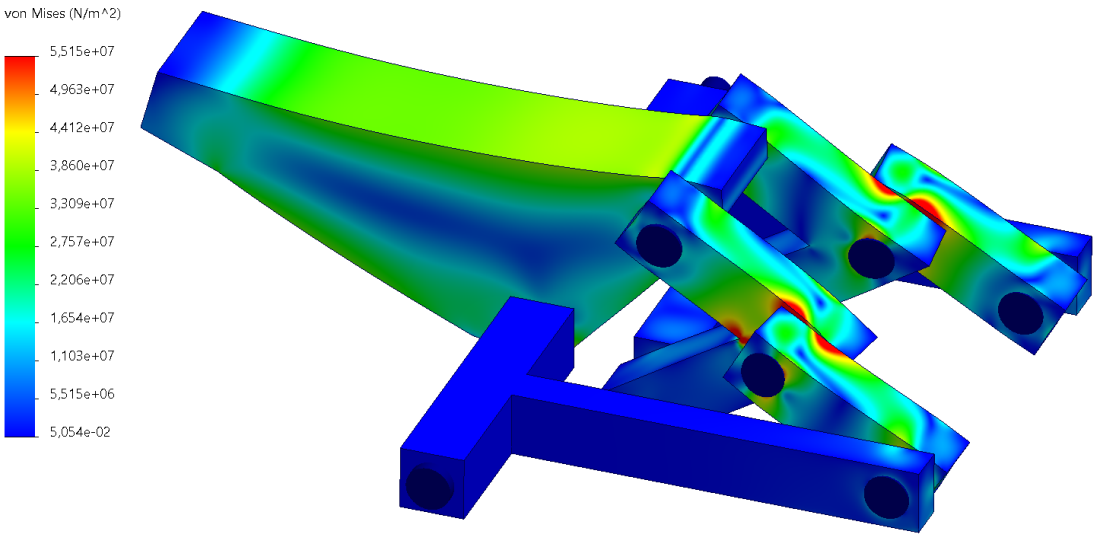

(b) Von Mises stress (deformed view).

Figure 7.4: Finite Element Method (FEM) preliminary model overview and Von Mises stress results.

during the enclosure phase, at room temperature, the backlash due to cryogenic temperature should not be taken in account here.

Regarding the strain level not, also in Figure 7.5, the highest strain levels are associated to the highest stress levels as expected. One can observe that the distortion of the different parts of the mechanism is low enough to confirm that the mechanism is capable of supporting this load magnitude.

Finally, Table 7.2 presents the loads within each pins of the mechanism. One can see that compared to Table 5.2, the order of magnitude of the loads is the same (4 kN for the pins $1 \rightarrow 5$ corresponding respectively to the points A, B, C, C and B; 6 kN for the pin 6 corresponding to the point O). The force

Table 7.2: Resulting connectors (pins) and nut forces.

	Shear Forces[a]			**Axial Forces**[b]
	Along x, [kN]	Along y, [kN]	Resultant, [kN]	Resultant, [kN]
Pin 1 (lever-knee connector)				
a	−3.7	+2.4	4.4	−1.0
b	+3.7	−2.4	4.4	+1.0
c	−3.7	+2.4	4.4	−1.0
Pin 2 (front lever-leg connector)				
a	+3.6	−2.1	4.1	+1.1
b	−3.6	+2.1	4.1	−1.1
Pin 3 (front leg-fixed connector)				
a	−3.6	+2.1	4.1	−1.1
b	+3.6	−2.1	4.1	+1.1
Pin 4 (back leg-fixed connector)				
a	+3.6	−2.1	4.1	−1.1
b	−3.6	+2.1	4.1	+1.1
Pin 5 (back lever-leg connector)				
a	−3.6	+2.1	4.1	+1.1
b	+3.6	−2.1	4.1	−1.1
Pin 6 (fixed-knee connector)				
a	+3.6	−4.9	6.1	0.0
b	−3.6	+4.9	6.1	0.0
c	+3.6	−4.9	6.1	0.0
Actuation point[c]				
a	+0.0	+0.2	0.2	+0.2
b	+0.0	+0.2	0.2	−0.2

[a] The shear forces have only x and y components.

[b] The axial loads are only applied along the z axis. See Figure 7.4 for the axis definition.

[c] The actuation point is at the nut pins, computed without the nut element and considering fixed hinges instead.

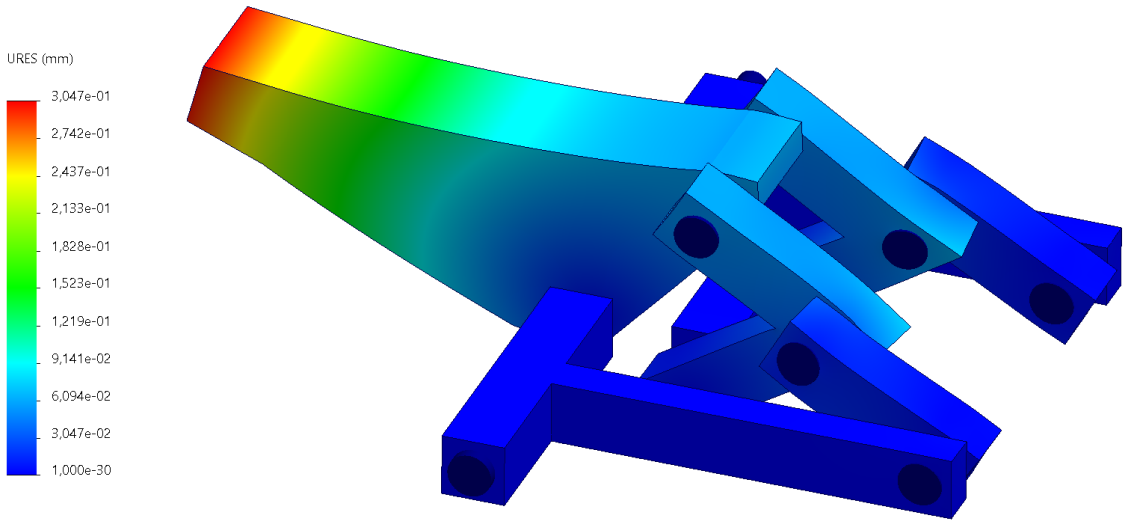

(a) Resulting displacements.

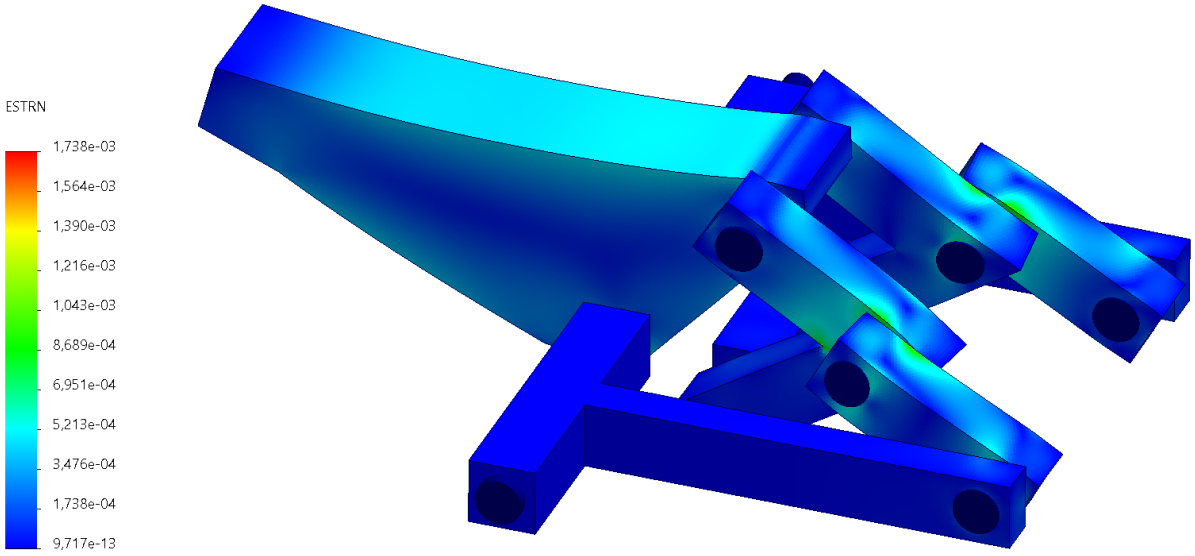

(b) Equivalent strain.

Figure 7.5: Resulting displacement and strain results of the FEM preliminary study.

applied to the nut bearings equals 2.8 N along the horizontal axis and equals 0.18 kN in the vertical axis, for each bearing. The axial forces cancels each other. This means that the stainless steel screw axis has to resist to 360 N vertically without transmit this to the actuator. This should be one of the requirements for the structure design that should be designed in a future work.

7.4 Conclusion

To conclude this design analysis section, the CAD model of the final conceptual design has been presented. The mass budget has been provided and a preliminary motion and FEM analysis have been performed.

The mass of the HDRM seems to be larger than expected initially (around 1.5 kg instead of 1 kg for the whole cover mechanism assembly). Since a structure interfacing the baseplate, the cryostat, the HDRM and its actuation parts should be designed, the mass will increase significantly. The optimization of the mass of the HDRM is therefore also critical to perform to mitigate the increase of mass with the integration of the structure. This however is a critical weakness of the HDRM solution to the enclosure and the launch lock problems.

The current design has a wide angular range to open and safely release the cover assembly. The structure must however orient the actuation axis of 2.36 deg downward with respect to the horizontal axis to have the smallest error of linear path compared to the average path. This adds complexity to the actual HDRM structure design.

The FEM preliminary analysis ensure the mechanism is able to resist to the internal loads applied at the enclosure. Indeed, the Von Mises stress remains always below the yield strength of the aluminum. In addition, the order of magnitude of the load computed analytically is the same as the ones computed in this FEM study. The actuation point is not exposed to high magnitude load. However, the screw axis should be able to resist to some vertical loads without transmitting loads to the actuator. This is also a requirements for the structure design of the HDRM.

In conclusion, the HDRM configuration fulfills the requirements. Indeed, the mechanism is designed to open and close autonomously. It provides sufficient force ratio to compress the gasket at the enclosure, and to remain static during the launch lock. This design is however not perfect nor complete since its mass could be optimized and the structure interface between its surrounding should be designed.

Chapter 8

Experimental Results

8.1 Seal Tests Philosophy

As mentioned in Section 2.3, and according to the CSL development plans of the DEA [1, 9], a sealing breadboard is designed to assess preliminary test sequences in order to validate O-ring materials candidate destined to be used for the sealing of the door. A set of standardized commercial DN40 gaskets of different materials is considered, from two different suppliers. Usually, the sealing breadboard test involves vibration testing and thermal tests under vacuum. The idea of this first sequence of test is to eliminate some candidate materials and validate the test sequence methodology. Further more tests should therefore be performed as later design work, with the DN160 O-ring joint typically.

The main objectives of these tests are:

- Check the conformity of commercial gaskets material information (if available);
- Check the possibility of using commercial gaskets;
- Check the survivability of different materials when exposed at cryogenic temperatures;
- Check the sealing capability before and after the cryogenic exposure;
- Validate the compression force measurement method.

8.1.1 Test Overview

First, the commercial gaskets are individually inspected to identify early the gaskets that would not be adapted for the intended use. Second, one gasket will be subjected to a full control loop involving the following sequence:

1. Compression force measurement: each gasket is compressed until a determined compression point to figure out the compression force reaction of the seal.
2. Leak test: each gasket is installed on a leak test device to check the initial leak rate.
3. Cryogenic exposure test: gaskets are clamped between clamps and dipped in a liquid dinitrogen (LN2) bath for 15 min. They are then left at ambient condition to heat back up.
4. Repetition of the compression force measurement.
5. Repetition of the leak test.

Between each test performed, an inspection and dimensional measures are performed. The gaskets are inspected to check for possible damages or abnormal features such as cuts, discolorations, cracks, etc. A first selection of material will be provided to select the gaskets that are best suited for further study.

8.1.2 Test Specimens

Table 8.1 presents the 6 different specimen materials used for the tests sequence described above that have been purchased from 2 different suppliers. Their nominal diameter (DN40) is standard.

Material	**Supplier**	**Thickness**, [mm]	**Quantity**
Ethylene-propylene-diene rubber (EPDM)	Pfeiffer	5.00	4
Fluorocarbon (FKM)	Pfeiffer	4.99	4
Chloroprene (CR)	Pfeiffer	5.03	4
Acrylonitrile-Butadiene (NBR)	Pfeiffer	4.99	4
Nitrile rubber (BUNA)	Lesker	5.20	4
Fluorocarbon FKM	Lesker	5.21	4

Table 8.1: Test specimens list considered for the tests sequence.

8.1.3 Inspection and Screening

The inspection process is performed starting with a visual check of the gasket. Upon reception from the suppliers, initial measures were proceeded and possible damage or defect were identified if any. This verification sequence is performed again between each test manipulation to track the possible condition that could lead to any failure modes. Photos are taken during each inspection process, and the thickness measured to four points along the gasket circumference to identify any local or global potential variations of thickness. Figure 8.1 shows the typical failure modes of gasket that could be encountered during the entire test sequence.

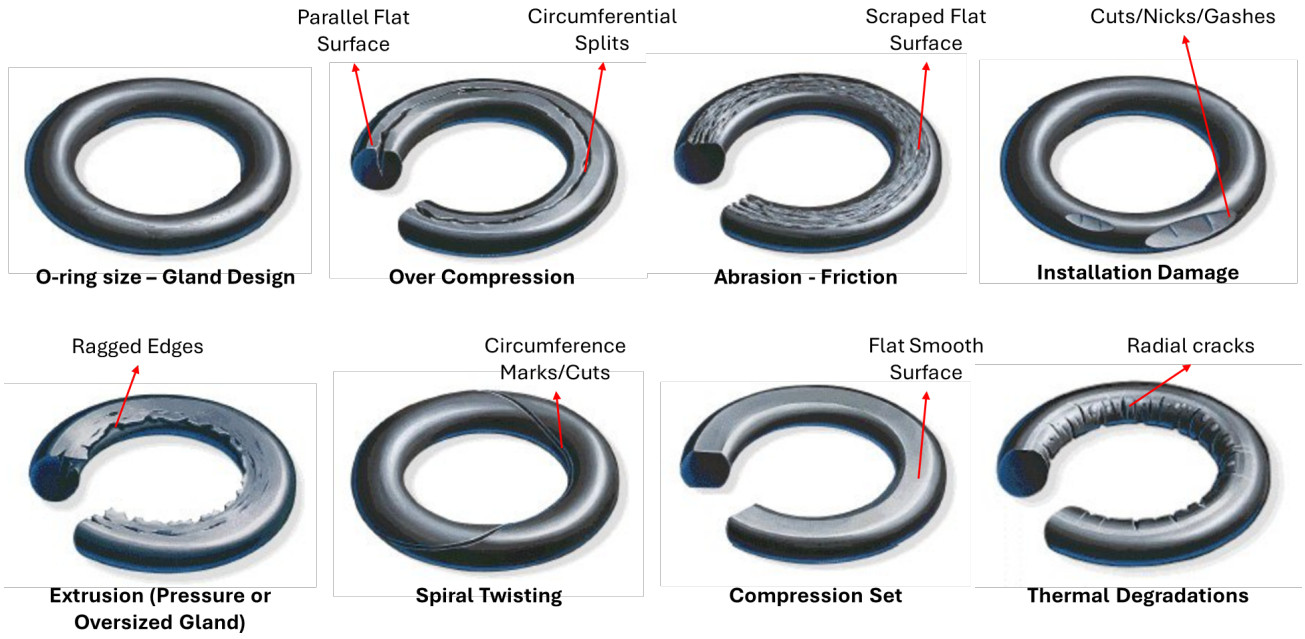

Figure 8.1: Typical relevant failure modes of O-ring joint, adapted from Marco Rubber & Plastics [8].

After the end of the screening process, Gaskets that are not compliant with the following pass/fail criteria are applied to all tested gaskets, are discarded:

- Visible appearance change, damage or other sign of any failure start.

- Leak tightness degraded to a point where 1 mbar of pressure or 10^{-7} mbar s^{-1} of leakage rate can not be reached.
- Compression set higher than 20%, which is the usual value assumed for most gaskets.

Gaskets that pass these screening criteria are selected and will be subjected to further more specific tests.

8.2 Joint Cryo-exposure Tests

8.2.1 Test Set-up Description

Figure 8.2 shows the simple principle of the cryogenic exposure test. A styrofoam box contains the LN2 bath in which each gasket sample will be submerged. The gasket equipped with an aluminum inner ring is clamped between two blank flanges and tightened using an aluminum clamp. Suspension wires permit to hold the samples and facilitate the extraction of the gaskets from the bath.

Once the LN2 is poured into the container, the gaskets are submerged for a 15 min duration. After that delay, the samples are left at ambient temperature to heat back up. They are finally dismounted and inspected to evaluate any potential visible degradation on its surface.

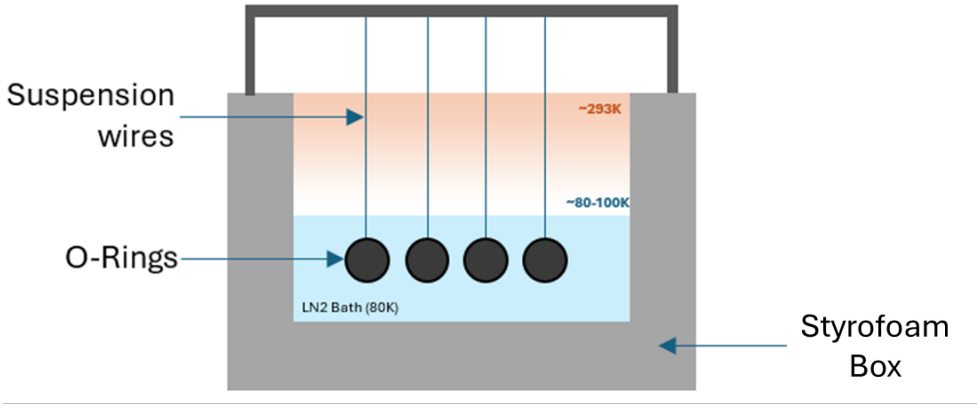

Figure 8.2: Cryogenic test principle overview, from Guilhem et al. [9].

8.2.2 Test Results

Figure 8.3 shows the actual set-up used to perform the test described. After the exposure and the slow warming up to room temperature, the gaskets tested did not present any visible differences. The Pfeiffer CR presented some cracks on its surfaces. However, after a few additional hours, the surface was uniform as before the cryogenic exposure.

8.2.3 Results Discussion

For cryogenics, the test was to immerge the joints directly into a liquid nitrogen bath. This is probably harsh compared to the real exposure it should ensure since the cooling is not progressive. It may causes some damage since the core of the o-ring joint has not yet been cooled that the outer section is cooled enough to retract. This may cause tiny cracks due to this difference of thermal behavior between the outer and the inner section of the joint. In addition, the exposure time is small compared to the real exposure performed during the AIT phase.

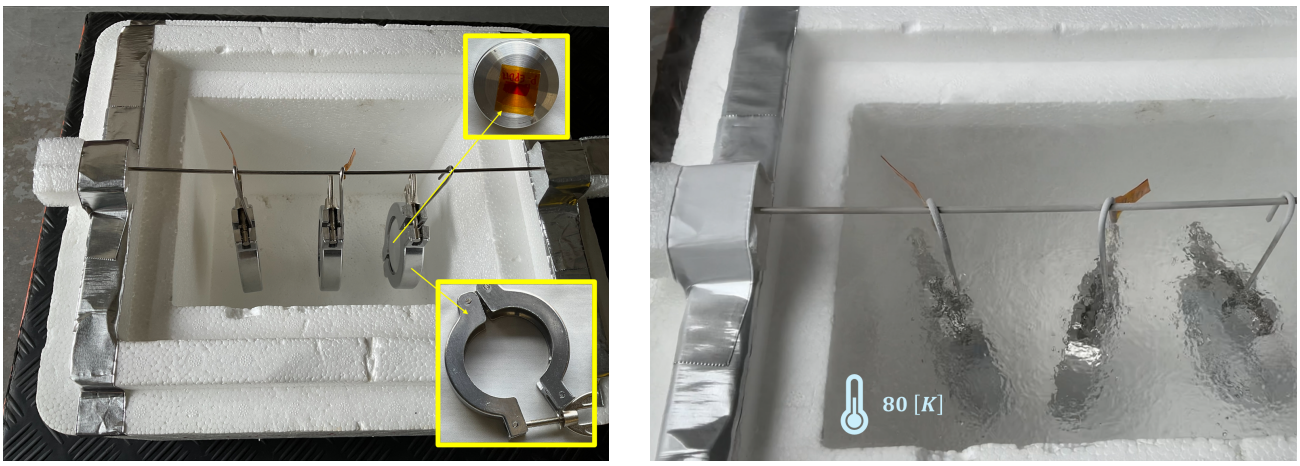

(a) Experimental set-up. (a) Cryogenic test.

Figure 8.3: Actual configuration of the cryogenic tests.

8.3 Joint Compression Tests

O-ring compression force is driven by numerous parameters such as the gasket thickness, the seal diameter and its constituting material. While the dimensions of the joint are always known up to a certain accuracy level, the material properties and especially the Shore hardness are not always available. Even if these data are provided, there are a high uncertainty about the compression force required to compress the gasket.

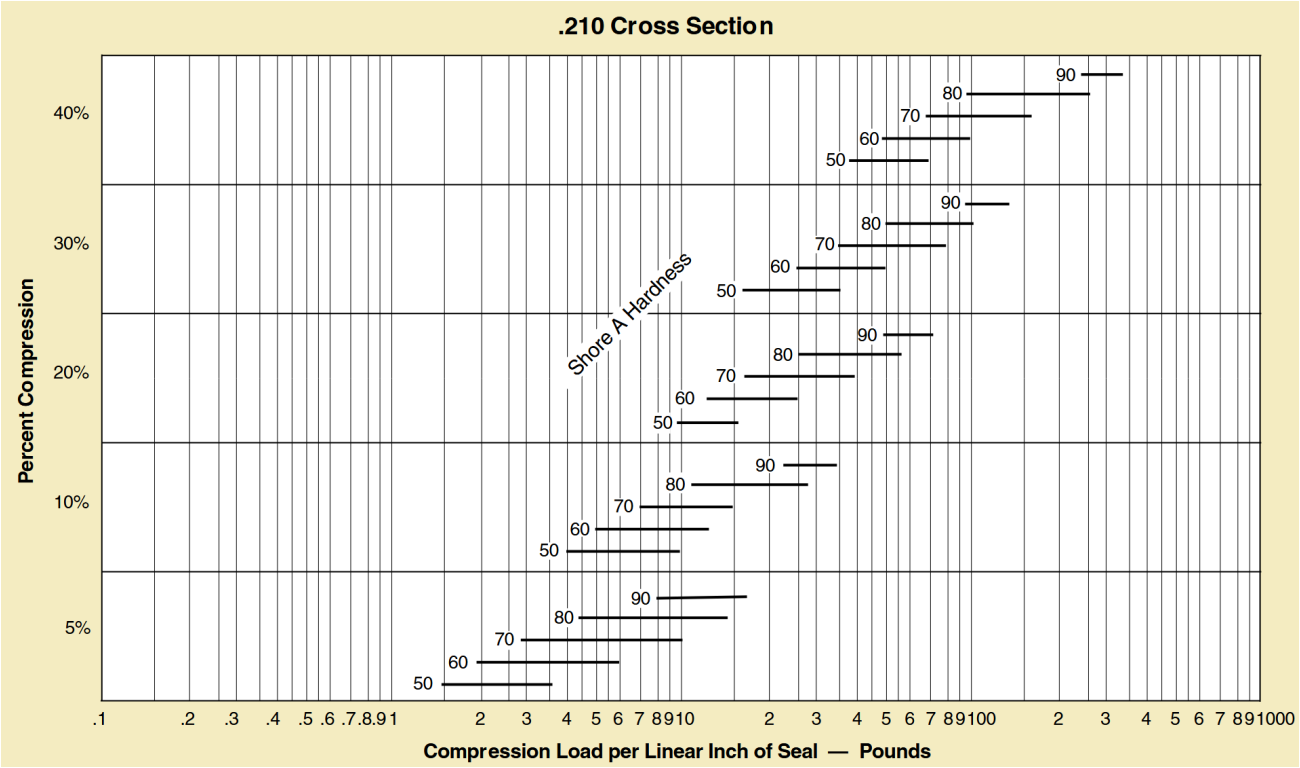

Figure 8.4: Compression load plot related to percent compression levels, taken from the Parker's O-ring Handbook [10].

Indeed, as shown in Figure 8.4, for a given Shore hardness level at a defined compression rate, there can be a large uncertainty on the compression load. Assuming for example the fluorocarbon (FKM) gasket

from Lesker, the specified Shore hardness is 75. With the graph only providing data for 70 and 80 Shore hardness, the computation done (after conversion to international system (SI) units) for both ranges gives the followings:

$$\begin{aligned} &70 \text{ Shore hardness: } 1.7 \rightarrow 7\,\mathrm{N\,mm^{-1}} \\ &80 \text{ Shore hardness: } 4.45 \rightarrow 9.6\,\mathrm{N\,mm^{-1}} \end{aligned} \tag{8.1}$$

For DN40 gaskets, the circumference length is estimated around $2\pi R = 125.66\,\mathrm{mm}$ and the compression force range results as:

$$\begin{aligned} &70 \text{ Shore hardness: } 220 \rightarrow 880\,\mathrm{N} \\ &80 \text{ Shore hardness: } 550 \rightarrow 1209\,\mathrm{N} \end{aligned} \tag{8.2}$$

Therefore, since the compression value are quite important for DN40 joints, the compression force is even larger for DN160. It is critical to evaluate accurately in order to choose a seal material that is not too hard to mitigate the compression force component, which is dominant by considering only $7\,\mathrm{N\,mm^{-1}}$ of compression load as assumed in Section 3.2.1.

8.3.1 Test Set-up Description

The test principle measures the compression force until the gasket is pressed to a known thickness. A 5 kN dynamometer is used to measure the compression force.

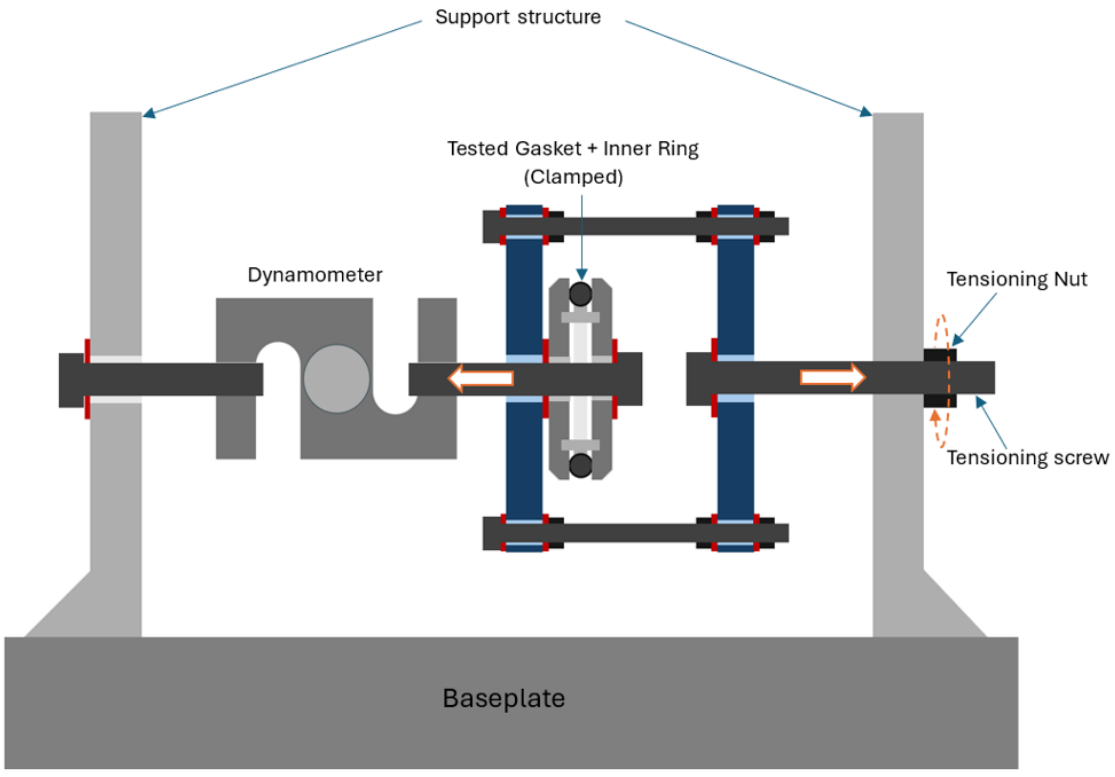

Figure 8.5: Overview of the first compression test configuration, from Guilhem et al. [9].

Figure 8.5 shows the first configuration chosen for the test. It has been adapted to a vertical version in order to facilitate the transition between two tests, and to gain in accuracy since it is aligned with the gravity direction. Figure 8.6 shows the adapted set-up. The gasket with its support ring is clamped

between two pierced blank stainless steel flanges. The assembly is pulled against an aluminum piece while the screw is set aside to increase the compression force. The consequence is that the dynamometer is loaded in traction and permit to evaluate the compression force level. Between each increase of level (force level step of 100 N considered), the distance between the flanges is measured using a caliper at 4 points along the gasket circumference to follow the compression rate of the gasket. The average measure of the distance is used to generate the results.

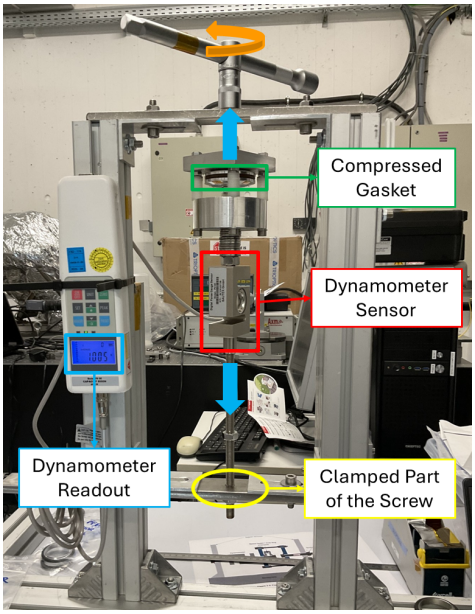

Figure 8.6: Compression test set-up used to perform the measures.

8.3.2 Test Results

Figures 8.7 presents the compression tests result before and after cryogenic exposure, for both the compression and decompression phases.
One can see that the Lesker BUNA and the Pfeiffer CR gaskets have not significantly be affected by the cryogenic exposure. The Pfeiffer EPDM, NBR and FKM have not a different behavior under 15% compression set. However, a variation is observed after. These gasket appears to be harder than before (for the NBR and the FKM). The opposite is observed for the EPDM. The Lesker FKM is also softer, but for the entire range of compression.

8.3.3 Results Discussion

Table 8.2 shows the compression force computed from the experimental measures, and provide more quantitative values in addition to the compression graph shown previously. The estimation of the compression force of DN160 gaskets is provided based on the DN40 experimental measures.

The cryogenic exposure have some effects on the gasket, excepted for the Pfeiffer CR and the Lesker BUNA for which the variation is not significant. Since the exposure may vary the behavior of almost each gasket, further experimental measures should be performed on DN160 gasket to confirm the tendency.

Finally, one can see that the order of magnitude of the compression force estimated in Section 3.2.1 is the same as the average of the different gaskets material considered through these tests. This confirms that the computations made earlier for the cover are probably close to the reality.

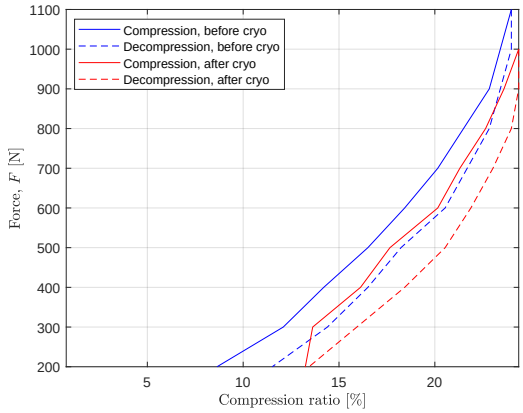

(a) Lesker FKM.

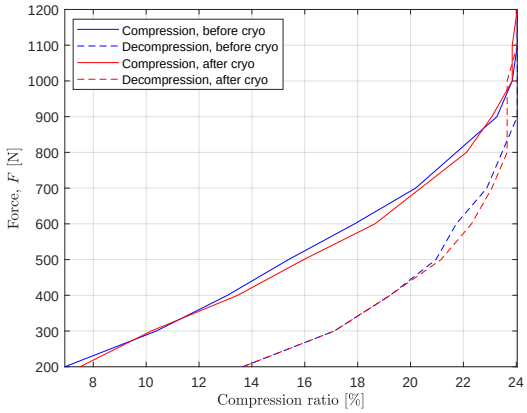

(b) Lesker BUNA.

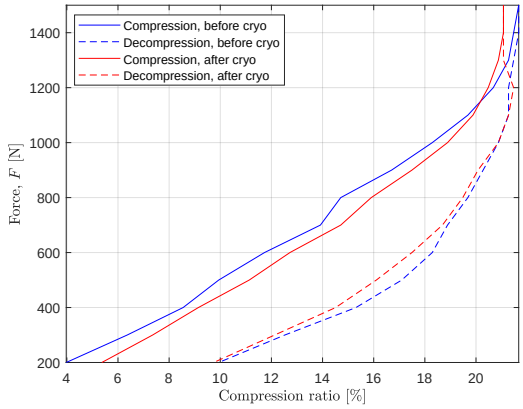

(c) Pfeiffer CR.

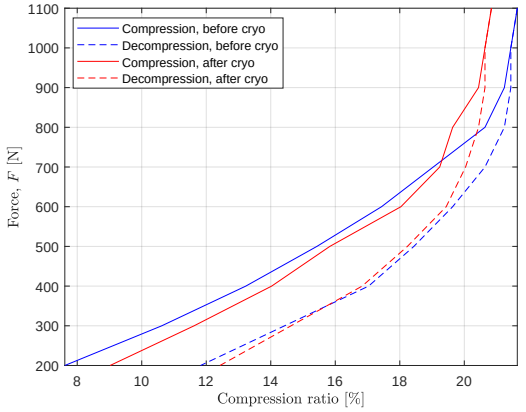

(d) Pfeiffer FKM.

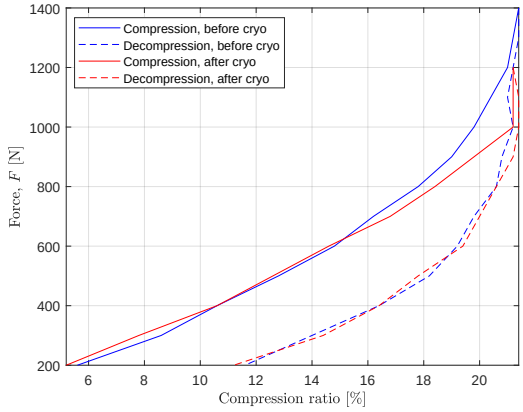

(e) Pfeiffer EPDM.

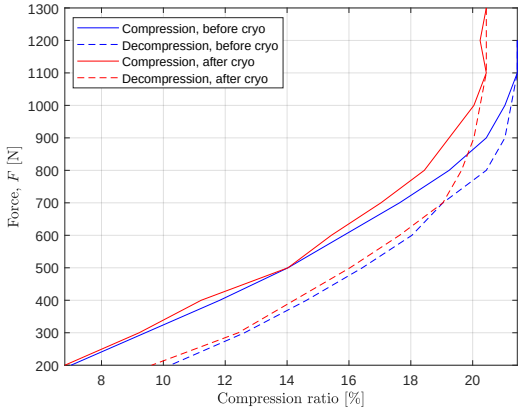

(f) Pfeiffer NBR.

Figure 8.7: Results of the compression tests on each sample gasket before and after cryogenic exposure.

8.4 Joint Leak Tests

8.4.1 Test Set-up Description

Figure 8.8 shows the configuration of the vacuum test, which consists in testing if the sample gasket permit to reach sufficient vacuum level and evaluate its leak tightness. The simple set-up includes the high-performance Pfeiffer ASM 340 leak detector. The device already includes an integrated dry backing

Table 8.2: DN40 compression force results before and after cryogenic exposure, and estimation for the DN160 gasket.

Material	**DN40 Compression Force**[a] [kN]		**Force per linear unit**[b] [N/mm]		**DN160 Compression Force**[b] [kN]	
	Before	After cryo	Before	After cryo	Before	After cryo
Pfeiffer EPDM	0.9	0.8	7.2	6.4	3.6	3.2
Pfeiffer FKM	0.8	0.8	6.4	6.4	3.2	3.2
Pfeiffer CR	1.1	1.1	8.7	8.7	4.4	4.4
Pfeiffer NBR	0.8	1.0	6.8	7.9	3.4	3.9
Lesker BUNA	0.7	0.7	5.6	5.6	2.8	2.8
Lesker FKM	0.7	0.6	5.6	4.8	2.8	2.4

[a] Force considered at 20% compression. Taken from the experimental measures.
[b] DN40 force considered at 20% compression divided by the disk perimeter of the gasket, considering a radius of 20 mm.
[c] Force considered at 20% compression. Estimated from the experimental measures, considering a radius of 80 mm.

pump and a turbo molecular pump. The typical sensitivity is $5 \cdot 10^{-13}$ mbar $\cdot$ L/s while using Helium for the leak detection (sniffing mode). Hydrogen is also possible for leak detection, but it has a lower sensitivity [64].

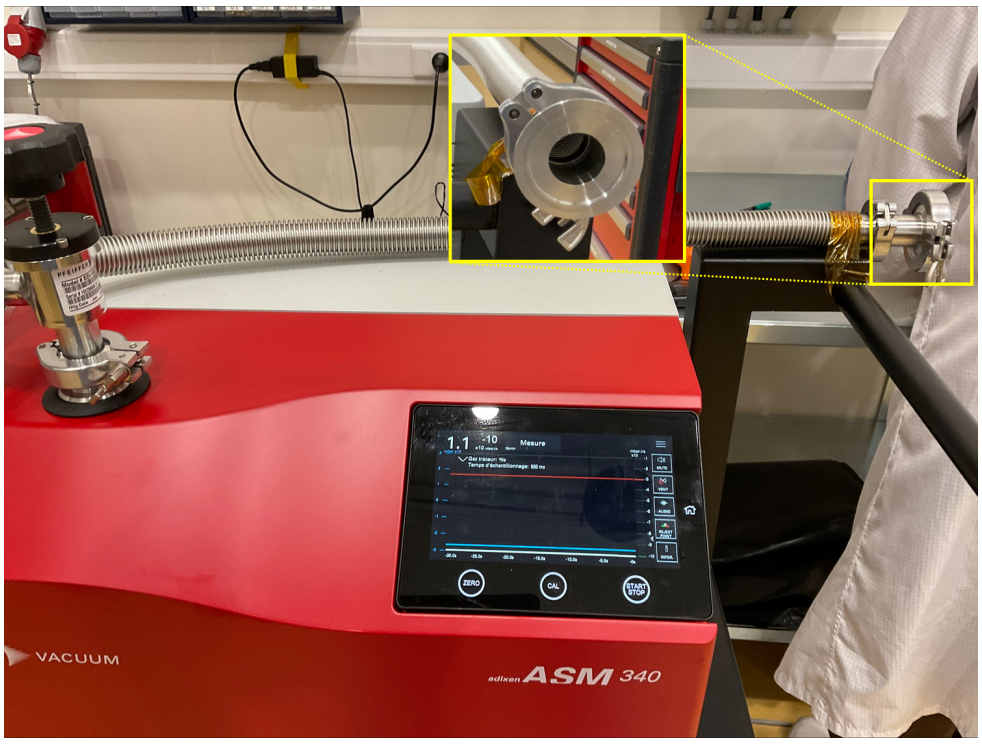

Figure 8.8: Overview of the leakage test configuration.

Each sample gasket is connected to a DN40 interface and the assembly is clamped. once started, the leak test device begins to pump out the clamped gasket until a sufficient vacuum level. The turbo-molecular pump is automatically started once the vacuum level permits it. The device provides directly the leak rate at the given time of the procedure. After 5 min, the leak rate is read from the device and the next gasket

is prepared after the pressurization of the actual one.

8.4.2 Test Results and Discussion

Table 8.3 provides the leak rate resulting from the leakage tests performed before and after the cryogenic exposure. One can observe that the leak rate are remaining in the same order of magnitude. This means that at this point, the gasket's materials considered have passed successfully the cryogenic exposure without any significant degradation of their tightness performances.

Material	**Leak Rate**, [mbar · L/s]	
	Before	After
Pfeiffer EPDM	$1.0 \cdot 10^{-10}$	$8.8 \cdot 10^{-11}$
Pfeiffer FKM	$9.7 \cdot 10^{-11}$	$8.5 \cdot 10^{-11}$
Pfeiffer CR	$9.3 \cdot 10^{-11}$	$6.1 \cdot 10^{-11}$
Pfeiffer NBR	$9.1 \cdot 10^{-11}$	$7.5 \cdot 10^{-11}$
Lesker BUNA	$9.4 \cdot 10^{-11}$	$7.9 \cdot 10^{-11}$
Lesker FKM	$9.7 \cdot 10^{-11}$	$8.2 \cdot 10^{-11}$

Table 8.3: Leakage rates after 5 min measured for each gasket, before and after cryogenic exposure.

8.5 Conclusion

To conclude this final section, the different test sequences performed have been described and their respective results discussed. The exposure to cryogenic temperature of the gaskets appeared to not affecting the visible surface of the samples. However, some compression force differences were observed for some of them, which were significant for the Lesker FKM gasket for example. The leak rate tests did not observe any significant variation in tightness performances of every sample tested.

In addition, the compression force evaluated on DN160 were reassessed again from the experimental measures. The order of magnitude of the compression force computed in Section 3.2.1 were retrieved. This means that the compression force, which is the dominant contribution to the HDRM force, is close to the equivalent experimental measures. This justifies the usefulness of the HDRM to decrease the actuation force required to its minimum value.

Chapter 9

Conclusions and perspectives

9.1 Conclusion

To conclude this conceptual design report, Chapter 1 presented the ATHENA mission, and the X-IFU instrument that hosts the dewar entrance assembly (DEA), and the door cryo-mechanism. The mission phases were presented with the requirements the mechanism must fulfill. Then, Chapter 2 introduces relevant similar design of cover mechanisms in space applications such as the Herschel observatory and the CLAES mission. Different families of actuators were discussed and compared. Since the cover has to be opened and closed without manual operations, the motorized actuator family was chosen to be the most relevant actuator for this application.

Once the context and the state-of-the-art were presented, Chapter 3 introduced the preliminary CAD model provided at the beginning of the design process. Some preliminary computations such as the HDRM force required and the loads in the bearings of the cover lever were developed through static computations. The bearings loads permitted to compute the actuation torque required to open the cover assembly using the ECSS standards. The HDRM force was the foundation of the HDRM conceptual design.

After that, Chapter 4 presented the parametric modeling process of the HDRM part. The Chebyshev four-bar linkage has been the first design choice for this conceptual design. The reason was that the mechanism had to balance a huge load at the cover lever contact, without transmitting that load along the actuator axis. And since its kinematic provided a good approximation of rotational motion to linear motion conversion, this family of linkage have been considered, as it was the case for Herschel also. The kinematic was derived analytically first, with the approach to detect linear path motion, no matter its orientation, and ensure the angular range of the HDRM permit to release the cover lever without any collision. The static then was computed considering the geometrical parameters provided by the preliminary design of the cover reassessed in the previous chapter. The enclosure was assumed as the design driver phase since the knee has to provide the force required to tighten the gasket with any help from pressure gradient due to vacuum within the cryostat. The validation then was performed for both the kinematics and the statics using *SolidWorks*, considering four configurations, such as the Herschel configuration and the classical Chebyshev four-bar linkage. While the kinematics was really accurate compared to the numerical equivalent path computed, the statics was less accurate for half of the validation model. This is explained by the fact that the numerical model is not plane and assumes punctual links while it is not the case in reality. This was the main motivation to perform experimental measures of the force ratio on a given test configuration. However, due to some delay, the experimental configuration did not arrive on time. The drawings are provided in the appendices.

Once the parametric model have been derived and validated (almost for the statics), Chapter 5 dis-

cussed the optimization process of the HDRM. Different classical *MATLAB* optimization solvers such as `fmincon`, `GlobalSearch` or `SurrogateOpt`. Since the actual problem was highly non-linear (due to the numerous kinematic and dimensional constraints), these classical optimization algorithms were not well-suited to converge to a global optimum. Instead, the pseudo-random algorithm Monte Carlo has been considered, with the Halton sequence generation. The idea of this sequence generation was to generate low discrepancy sets of random parameters of the HDRM, distributed uniformly within the parametric boundaries fixed by the dimensional constraints. The force ratio and the available size for the shaft of the actuator were the performance metrics used to discriminate the different configurations provided by the optimization process. Table 9.1 recalls the parameters of the optimized configuration found by this process. Its associated force ratio were evaluated to 0.009 [−] and since the linear path was almost horizontal, the available place for the actuator and its potential gearbox were assured. The drawback of this optimum was that the loads computed at the articulations were high (6.1 kN for the peak load).

	L_{OD}	L_{OA}	L_{AB}	L_{BD}	L_{BC}	L_{OF}	η	γ	ψ
Opti	51	26	21	20	23	46	120	293	$1 \rightarrow 0$

Table 9.1: Optimized configuration parameters: lengths in mm, angles in deg.

Later, Chapter 6 presented the derivation for the conceptual design of the HDRM, from the optimized configuration found by the optimization process. First, the material of the bearings and the washers have been discussed. Indeed, the main pieces of the HDRM are constituted of aluminum 6061-T6 alloy to avoid mismatch with the DEA surroundings (the cryostat is made of the same aluminum). The bearings should be constituted of a different material to avoid metal-to-metal contacts and minimize the friction at the articulation. Due to the high load at the bearings, the Vespel SP-2515, which was the most promising material for the bearings due to its light weight, its friction properties and its thermal properties (close to the aluminum), appeared to deform excessively (based on Hertz contact stress theory). The bronze has been considered instead and the C-52480 phosphor bronze have been chosen because it has the closest coefficient of thermal expansion compared to the aluminum one. However, the bearings loads necessitated to increase the length (up to 30 mm) of the bearings to decrease the stress provided during the enclosure. Second, the tolerance (ISO286-1) has been considered to handle the thermal contraction of the HDRM at 50 K. The maximum contraction is evaluated at 0.26 mm. Third, the actuation force required at the actuation point of the HDRM have been computed considering the ECSS standards and is evaluated to 39.6 mN. The arm-lever provided by the HDRM is significant but also required to minimize as much as possible the size of the actuator. The electrical consumption is therefore critical since it dissipates heat that could degrade the performances of the cryostat and damage it.

Then, Chapter 7 presents the final conceptual design of the HDRM. The updated preliminary CAD model was presented, and the design described. The mass budget of the HDRM conceptual design is also provided. The overall mass of the door cryo-mechanism, including the cover and the baseplate is evaluated with margins to 1.5 kg instead of 1 kg estimated at the beginning of the design. A motion analysis performed with *SolidWorks* is provided after, ensuring that the HDRM angular range is large enough to safely open the door without collisions. This also verifies the linearity of the point C motion path, for which the error is more or less than ± 0.1 mm from the linear average curve. The actuation shaft has however to be oriented of 2.3 deg to reach this level of performances. Finally, a preliminary FEM analysis is presented using the *SolidWorks Simulation* software. The idea of this analysis was to reassess first the static loads computed analytically. The order of magnitude remains the same, which confirms the analytical computations. Then, the idea was also to qualitatively assess that the HDRM pieces should not be exposed to stress above the yield strength of the aluminum, which would mean that the pieces of the mechanism would deform plastically. The Von Mises stress computed is one order of magnitude below the yield strength of the aluminum, which means the HDRM pieces remain in the elastic domain of deformation.

Finally, independently from the previous chapters, Chapter 8 presented the experimental tests performed on different DN40 gaskets from Pfeiffer and Lesker. The idea was first to confirm experimentally the order of magnitude of the compression force evaluated in Chapter 3, as it was the dominant contributor to the HDRM force required to maintain the seal. Second, it was to evaluate if cryo-exposure of different materials could vary the compression and the leak properties of these gasket. In order to do that, the compression tests, the cryo-exposure tests and the leak test sequences were presented. While the cryo-exposure inspection of the gasket did not spot any failure nor definitive variations, the compression force appeared to slightly vary for some materials. The leak test did not finish with any significant variation of tightness performances. Finally, the compression force evaluated at the early stage of this conceptual design was 3.5 kN (lower for some samples, higher for others). This was the same order of magnitude than the preliminary consideration made in Chapter 3. This confirms that the HDRM force required is around 2.5 kN at least, and reinforces the necessity of the HDRM to decrease it through an adapted arm-lever to mitigate the actuation force required.

9.2 Perspectives

The actual DEA door mechanism design, and more specially the conceptual design of HDRM developed through this report presents some weaknesses and lacks that are critical to fix and fulfill for the next design iterations. The cover has not been the main part covered within this report. It only considered the relevant parts of the cover that have been used for the HDRM design, and other critical part. This part of the design however requires to be more detailed. The shape of the cover as well as the beryllium windows integration should be investigated. The interface between the cover dome and the lever requires to be designed. Also, passive anti-adhesion device to avoid cryogenic adhesion of the gasket to the cover surface should be investigated, since it was completely neglected through this report. This could be performed in parallel to DN160 experimental tests to enforce the thermal behavior of the materials considered within the experimental tests presented in this report.

In addition, the HDRM mass is actually not optimized. The optimization of the mass of the HDRM pieces could be performed to decrease the mass of the mechanism. Furthermore, the integration of a structure that interfaces the HDRM, the DEA through the baseplate, the cryostat and the actuator assembly should be considered. Position of the actuator should be carefully determined to ensure that the linear path will have the smallest error possible as provided by the current design. The vibration analysis should be performed to ensure the structure is not adding natural frequencies that could be critical during the launch. The mass of this structure should also be minimized. Moreover, the actuator parts, such as the nut, the screw worm shaft, the gearbox and the stepper motor should be designed in more details. Particularly, heat dissipation should be evaluated and minimized. This would lead to some optimization of acceleration profile that could minimize these dissipation as much as possible.

Finally, due to the complexity of the current design and to its weaknesses (high bearing loads, structure required, not light weighted), the investigation of alternative design could be interesting. Space mechanisms should be kept as simple as possible. Since the DEA door cryo-mechanism is a single point of failure of the whole instrument, trade-offs with alternative concepts could enforce the current conceptual design or discriminate it for another one more suitable.

To sum up the future perspectives considered:

- Detailed design of the cover assembly (gasket adhesion problem, interface between the cover of the lever, beryllium windows, shape of the cover, etc.);
- Optimization of the HDRM pieces mass, and design of the structure interfacing the HDRM with its surroundings;
- Design the HDRM actuator assembly (gearbox ratio, acceleration profile optimized to minimize heat dissipation, shaft and nut design);
- Investigation of alternative mechanism to the HDRM concept presented.

Appendices

Experimental Static Validation

This section of the appendices presents the drawings concerning the prototype designed for the statics validations and the beam calibration results in prevision of the experimental computation of the force ratio of the configuration.

Beam Calibration

The measure of the force delivered by the HDRM requires to have to measure device for know the force applied as input to the HDRM and the force measures at the output. Since the CSL owns only one dynamometer, an alternative way to measure the force have been considered using a cantilever beam.

Mathematical Modeling

The principle is based on the deflection of a simple cantilever beam due to the application of the load along its surface. The behavior of the beam should be therefore calibrated in order to be able to relate accurately the force measure to the real force applied by the HDRM.

The mathematical derivation of the deflection of a cantilever beam is expressed as follows [62]:

$$\begin{aligned} y(x) &= -\frac{F \cdot x^2}{6EI}(x_f - x) \ \textbf{if } x \leq x_f \\ &= -\frac{F \cdot x^2}{6EI}(x - x_f) \ \textbf{if } x > x_f \end{aligned} \tag{9.1}$$

where $E = 68.9\,\text{GPa}$ is the Young's modulus of the aluminum constituting the beam, x is the position of the deflection measure, x_f is the position of the force applied and $I = \frac{a^4}{12}$ is its second moment of area.

The load measure principle is based on this Equation, rearranging the term to isolate the force from the other parameters (since the deflection if measures). This could give an order of magnitude of the force that deflects the beam, and then deduce the force ratio experimentally.

Test Set-up Description

Figure 9.1 shows the calibration set-up built. The aluminum beam has a square section of $a = 2\,\text{cm}$ wide and measure 30 cm. Loads of 100 and 200 N are considered successively. It is applied 1 cm from the tip of the beam. Masses of 10 and 20 kg are used as loads while hanging at the x_f point.

Tests Results

Figure 9.2 shows the deflection results for both loads computed analytically, numerically and measured experimentally. One can observe that the three results are really close to each other, which means that the numerical and the analytical models are correlated to the reality.

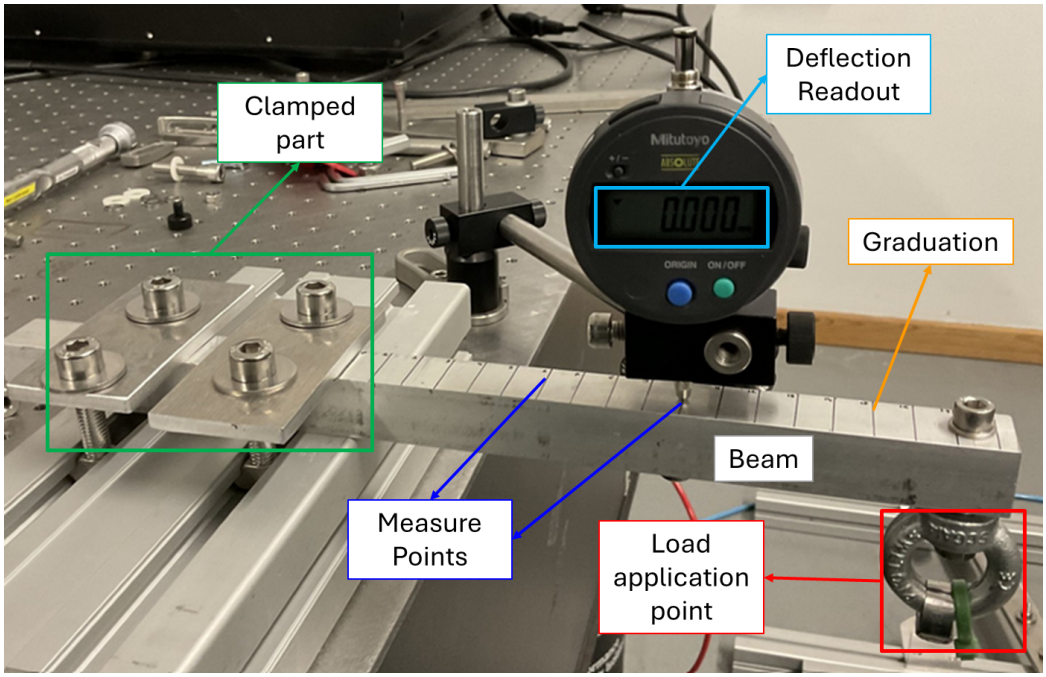

(a) Test set-up description.

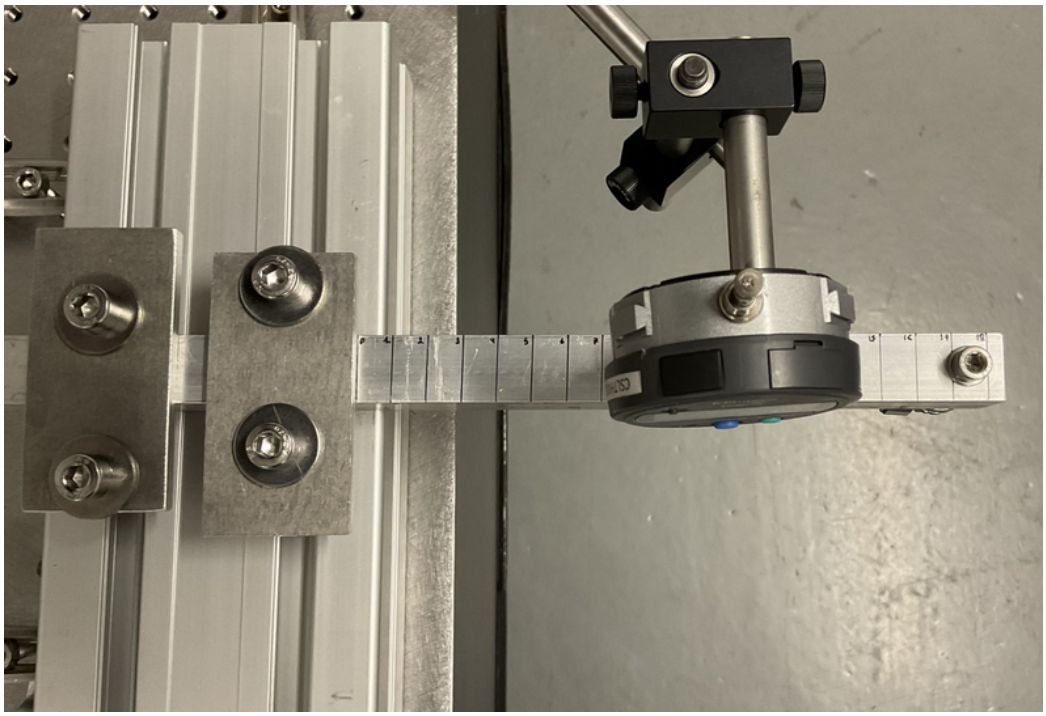

(b) Test set-up (upper view).

Figure 9.1: Calibration text set-up overview.

Prototype Drawings

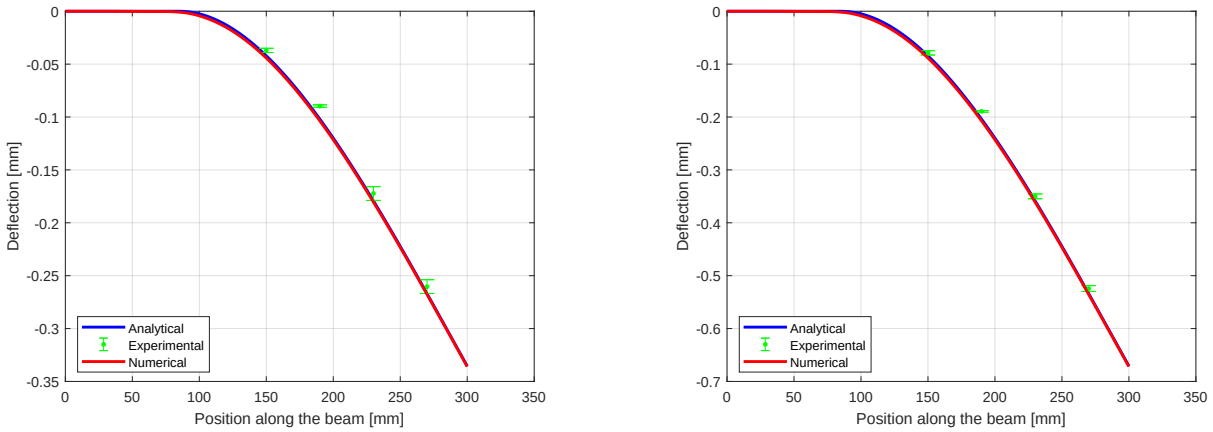

(a) Beam deflection under 0.1 kN load.

(b) Beam deflection under 0.2 kN load.

Figure 9.2: Comparison of beam deflection under different loads.

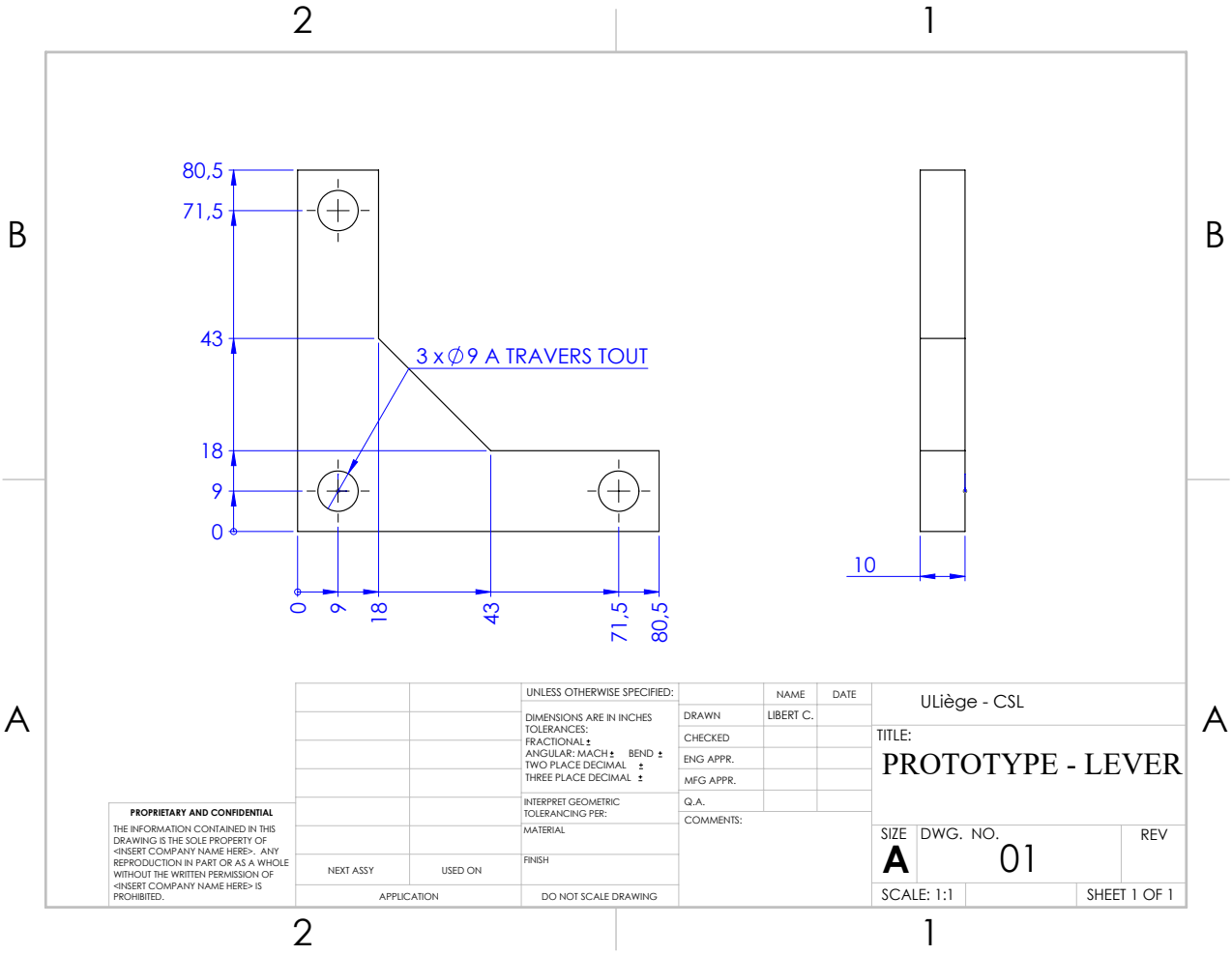

SolidWorks drawing of the lever parts.

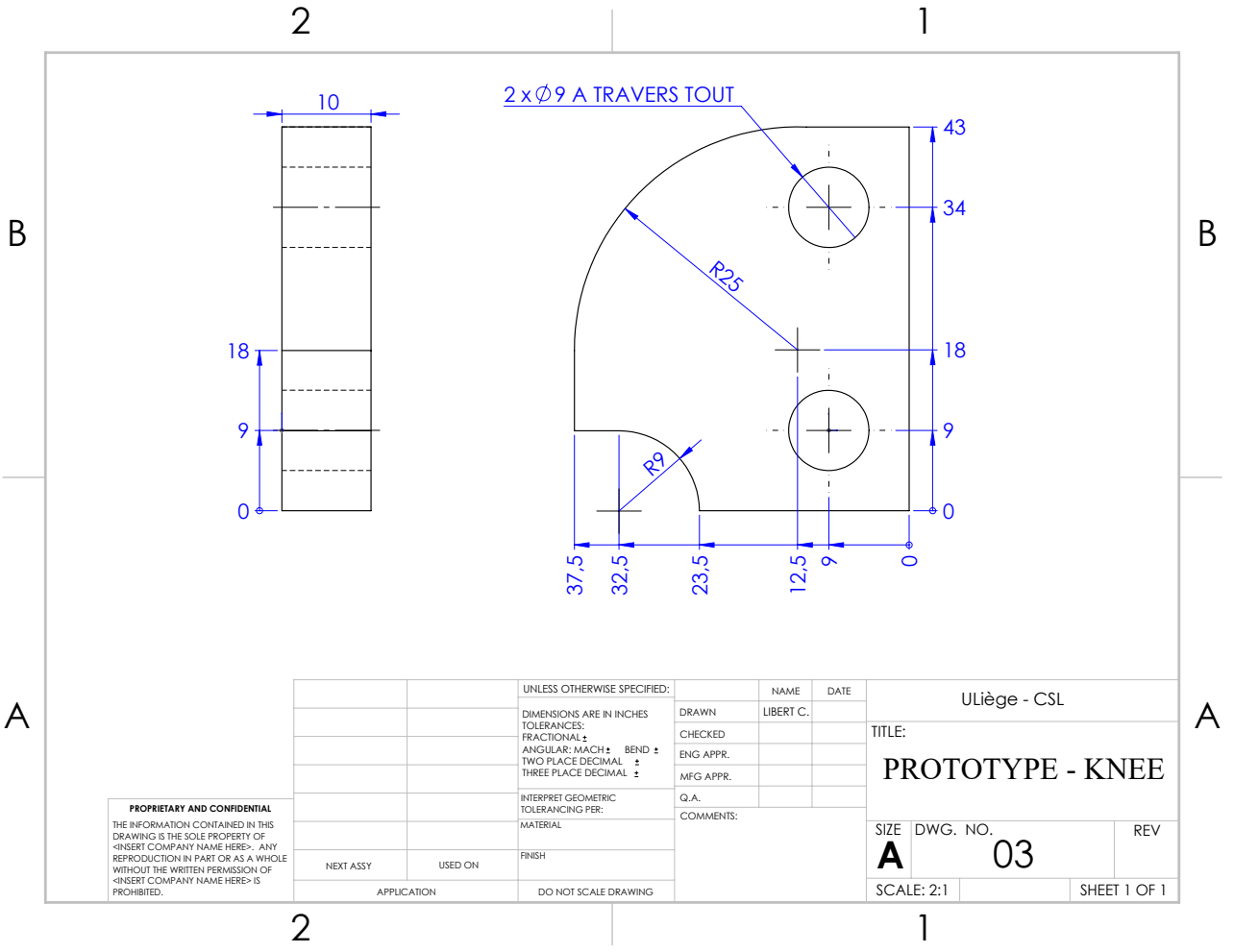

SolidWorks drawing of the knee part.

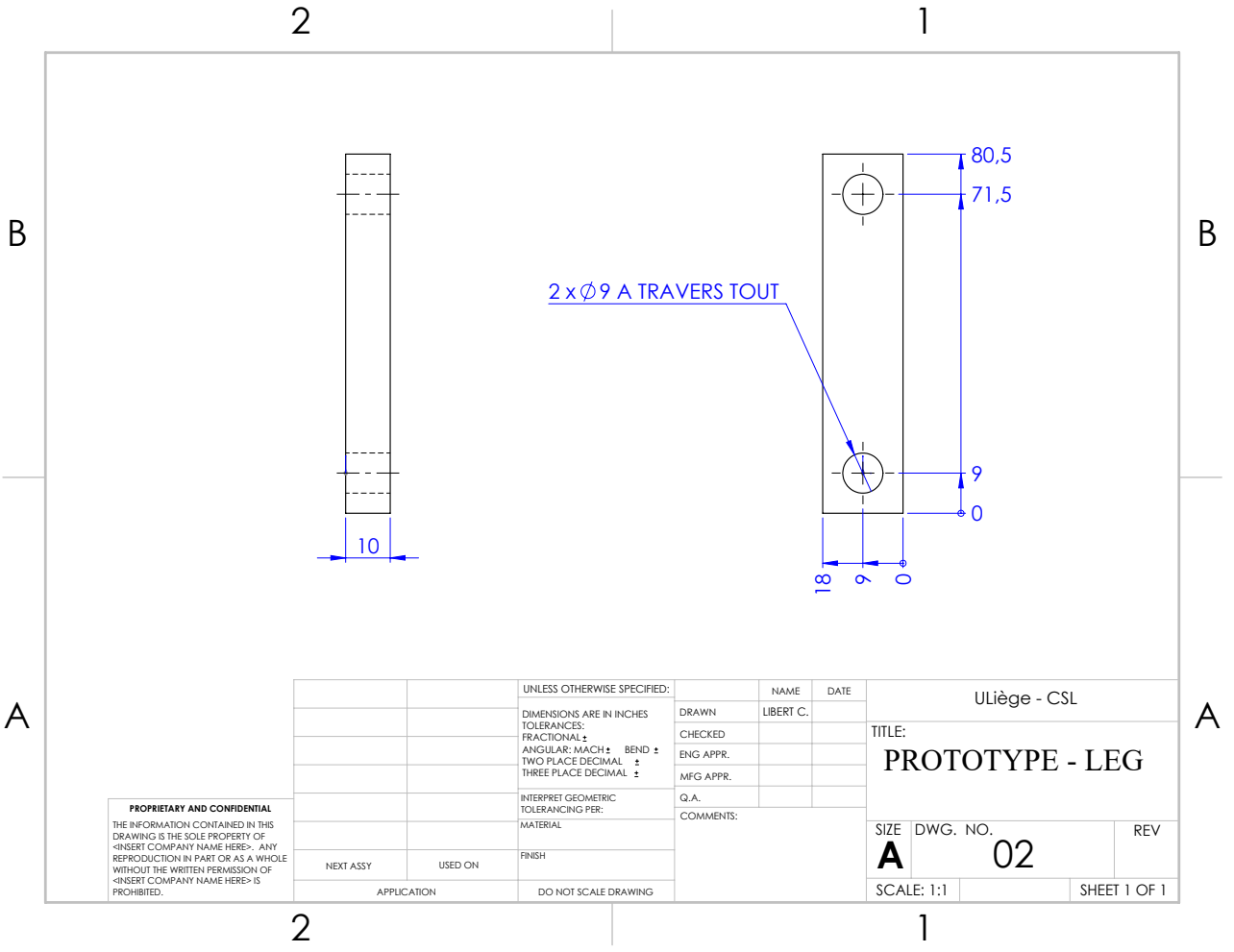

SolidWorks drawing of the leg parts.

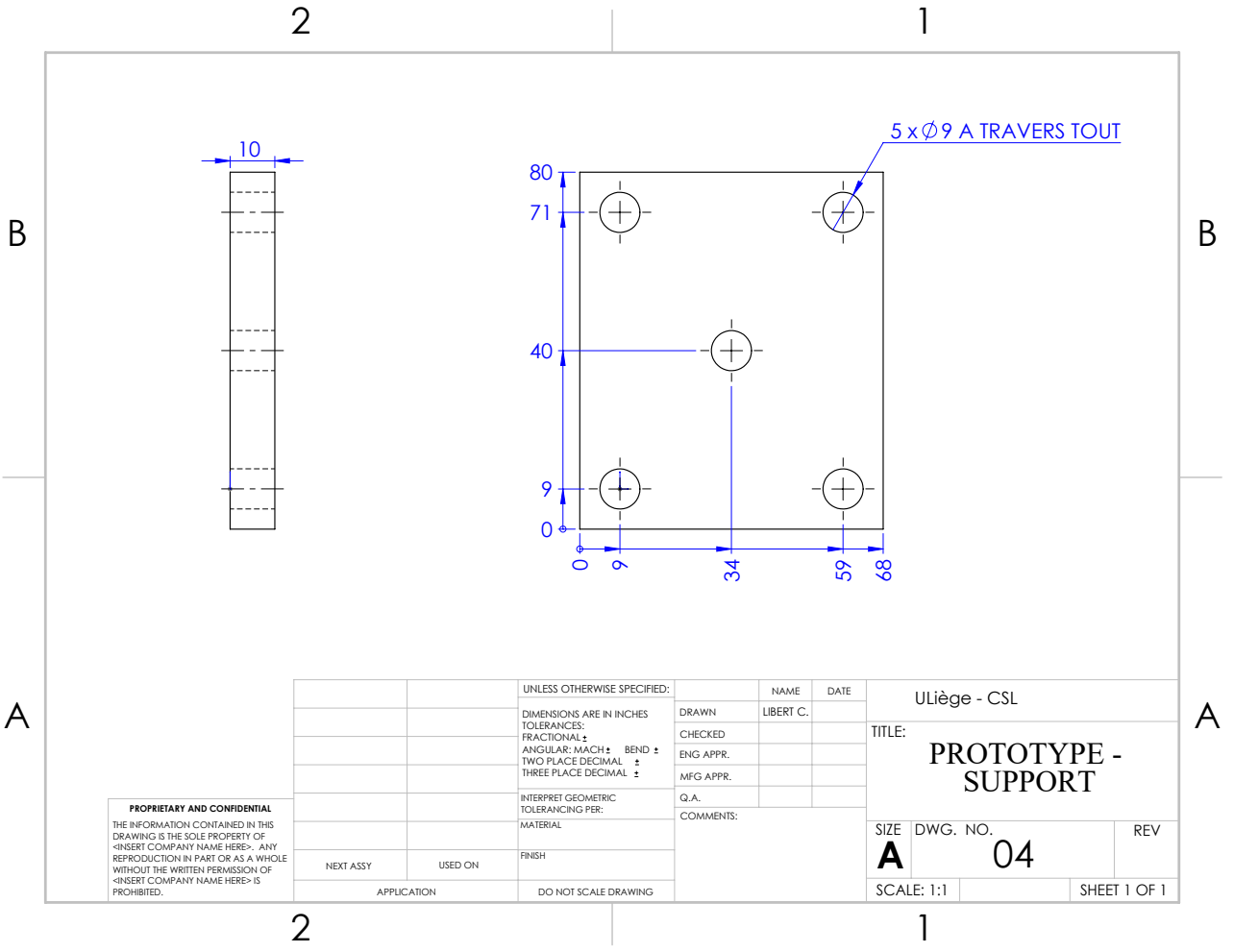

SolidWorks drawing of the support parts.

Bibliography

[1] Lionel Jacques, Tanguy Thibert : Athena X-IFU - Dewar Entrance Assembly: Development Plan. Technical Report: PL-CSL-XFU-24009, Centre Spatial de Liege (CSL), Liege, Belgium, June 2024.

[2] Paul Janu, Manfred Falkner, Ludwig Supper, Rudolf Schermann, Christian Laa et Gerhard Traxler : Cryostat cover mechanism for the herschel satellite: Design and qualification test results. *In Proceedings of the 11th European Space Mechanisms and Tribology Symposium (ESMATS)*, Vienna, Austria, 2005. Austrian Aerospace GmbH, European Space Agency/ESTEC.

[3] Andrea Galbiati, Alessandro Bursi, Floriano Venditti et Geert Smet : Separation nut life testing for launch locking devices. *In Proceedings of the 18th European Space Mechanisms and Tribology Symposium*, Munich, Germany, 2019. ESA.

[4] D. M. Stubbs : Development of the claes instrument aperture door system. *NASA, John F. Kennedy Space Center, The 24th Aerospace Mechanisms Symposium*, 1990.

[5] Arthur P. Boresi et Richard J. Schmidt : *Advanced Mechanics of Materials*. John Wiley & Sons, 6 édition, 2002.

[6] J. E. Shigley, C. R. Mischke, R. G. Budynas et K. Nisbett : *Mechanical Engineering Design*. McGraw-Hill Education, New York, 9th édition, 2011.

[7] International Organization for Standardization : ISO 286-1:2010 - Geometrical product specifications (GPS) – ISO code system for tolerances on linear sizes – Part 1: Basis of tolerances, deviations and fits. `https://www.iso.org/obp/ui/#iso:std:iso:286:-1:ed-2:v1:en`, 2010. Accessed: 2025-06-05.

[8] Marco Rubber and Plastics : O-ring failure & troubleshooting guide, 2025. Accessed: 2025-05-23.

[9] G. Terrasa : Seal test and characterisation plan. Rapport technique, Centre Spatial de Liege, Avenue du Pre-Aily, B 4031 Angleur, Belgium, May 2025. Verified by L. Jacques, Released by T. Thibert.

[10] Parker Hannifin Corporation : *Parker O-Ring Handbook*. Parker Hannifin Corporation, Lexington, KY, 2025. Accessed: 2025-05-23.

[11] Space engineering – Mechanisms. Rapport technique ECSS-E-ST-33-01C Rev.2, European Cooperation for Space Standardization (ECSS), March 2019. 1 March 2019.

[12] DuPont Specialty Products USA, LLC : *DuPont Vespel S-Line Design Handbook*, 2022. Document H-53668-2 (09/22).

[13] J.R. Davis, éditeur. *ASM Specialty Handbook: Copper and Copper Alloys*. ASM International, Materials Park, OH, 2001.

[14] European Space Agency : Cosmic Vision: Space Science for Europe 2015-2025. ESA Brochure BR-247, European Space Agency, Noordwijk, The Netherlands, October 2005.

[15] K. Nandra et Al. : The Hot and Energetic Universe: A White Paper presenting the science theme motivating the Athena+ mission, 2013.

[16] Jansen, F. and Lumb, D. and Altieri, B. and Clavel, J. and Ehle, M. and Erd, C. and Gabriel, C. and Guainazzi, M. and Gondoin, P. and Much, R. and Munoz, R. and Santos, M. and Schartel, N. and Texier, D. and Vacanti, G. : XMM-Newton observatory - I. The spacecraft and operations. *Astronomy & Astrophysics*, 365:L1–L6, January 2001.

[17] Wenzel, W. : The Chandra X-ray Observatory: Five Years of Observations. *COSPAR Information Bulletin*, 162:5–7, May 2005.

[18] NASA : Astro-H (Hitomi) Trajectory Details. `https://nssdc.gsfc.nasa.gov/nmc/spacecraft/displayTrajectory.action?id=2016-012A`, February 2016. NASA National Space Science Data Center (NSSDC).

[19] Didier et Al. Barret : The Athena X-ray Integral Field Unit (X-IFU). *In* Jan-Willem A. den Herder, Tadayuki Takahashi et Marshall Bautz, éditeurs : *Space Telescopes and Instrumentation 2016: Ultraviolet to Gamma Ray*, volume 9905 de *Society of Photo-Optical Instrumentation Engineers (SPIE) Conference Series*, juillet 2016.

[20] Tanguy Thibert, Lionel Jacques, Guilhem Terrasa, Etienne Lallemand, Gregor Rauw et Christian Kintziger : Aperture cylinder on athena x-ifu: development status. *In Space Telescopes and Instrumentation 2022: Ultraviolet to Gamma Ray*. SPIE, 31 August 2022.

[21] Marco Barbera et Al. : ATHENA X-IFU thermal filters development status toward the end of the instrument phase-A. *In* Jan-Willem A. den Herder, Shouleh Nikzad et Kazuhiro Nakazawa, éditeurs : *Space Telescopes and Instrumentation 2018: Ultraviolet to Gamma Ray*, volume 10699. International Society for Optics and Photonics, SPIE, 2018.

[22] Goran L. Pilbratt : Herschel Space Observatory mission overview. *In* John C. Mather, éditeur : *IR Space Telescopes and Instruments*, volume 4850, pages 586 – 597. International Society for Optics and Photonics, SPIE, 2003.

[23] Eaton Corporation : Non-explosive actuators: Separation nuts, pin pullers, and frangible nut actuators, 2018. Accessed May 14, 2025.

[24] Aidan E. Roche et John B. Kumer : Cryogenic Limb Array Etalon Spectrometer (CLAES): Experiment Overview. *In* Ramsey K. Melugin et Warren G. Pierce, éditeurs : *Cryogenic Optical Systems and Instruments III*, volume 0973, pages 324 – 334. International Society for Optics and Photonics, SPIE, 1988.

[25] General Magnaplate Corporation : Magnaplate hcr: "synergistic" surface enhancement technology maximizes corrosion resistance and hardness of aluminum and aluminum alloys. `https://www.magnaplate.com/pdfs/brochures/magnaplate_hcr.pdf`, 2025. Accessed: 2025-05-28.

[26] James L. Fanson, Giovanni G. Fazio, James R. Houck, Tim Kelly, George H. Rieke, Domenick J. Tenerelli et Milt Whitten : Space Infrared Telescope Facility (SIRTF). *In* Pierre Y. Bely et James B. Breckinridge, éditeurs : *Space Telescopes and Instruments V*, volume 3356, pages 478 – 491. International Society for Optics and Photonics, SPIE, 1998.

[27] Stephen M. Volz, Russell Schweickart, Kermit Gause et Robert Pederson : Sirtf cryostat requirements and development. *Cryogenics*, 39(12):975–983, 1999.

[28] Martin F. Kessler : Infrared Space Observatory (ISO): mission and spacecraft. *In* Marija S. Scholl, éditeur : *Infrared Spaceborne Remote Sensing*, volume 2019, pages 9 – 14. International Society for Optics and Photonics, SPIE, 1993.

[29] David B. Carte, Niraj K. Inamdar, Michael P. Jones et Rebecca A. Masterson : Design and test of a deployable radiation cover for the regolith x-ray imaging spectrometer. *The 42nd Aerospace Mechanism Symposium*, 2014.

[30] Thomas W. Duerig, K. N. Melton, D. Stockel et C. M. Wayman : *Engineering Aspects of Shape Memory Alloys*. Butterworth-Heinemann, London and Boston, 1990.

[31] Peter L. Conley, éditeur. *Space Vehicle Mechanisms: Elements of Successful Design*. John Wiley & Sons, New York, 1998. Includes contributions from over 30 experts in the field.

[32] John D. Busch, William E. Purdy et A. David Johnson : Development of a non-explosive release device for aerospace applications. *In Proceedings of the 26th Aerospace Mechanisms Symposium*, page Not specified, Greenbelt, MD, 1992. NASA. NASA Conference Publication 3147.

[33] Tini frangibolt actuator to support and release loads - ebad.

[34] Malcolm Macdonald et Viorel Badescu, éditeurs. *The International Handbook of Space Technology*. Springer, 2014.

[35] Dominiek Reynaerts et Hendrik Van Brussel : Design aspects of shape memory actuators. *Mechatronics*, 8(6):635–656, 1998.

[36] S. A. Stern and D. C. Slater and J. Scherrer and J. Stone and M. Versteeg and M. F. A'hearn and J. L. Bertaux and P. D. Feldman and M. C. Festou and Joel Wm. Parker and O. H. W. Siegmund : Alice: The Rosetta Ultraviolet Imaging Spectrograph. *Space Science Reviews*, 128(1):507–527, February 2007.

[37] Adrian M. Glauser, Ulrich Langer, Alex Zehnder et Manuel Güdel : A contamination control cover for the Mid Infrared Instrument of the James Webb Space Telescope. *In* Eli Atad-Ettedgui et Dietrich Lemke, éditeurs : *Advanced Optical and Mechanical Technologies in Telescopes and Instrumentation*, volume 7018, page 70184L. International Society for Optics and Photonics, SPIE, 2008.

[38] Tharek Mohtar, Alessandro Bursi, Andrea Galbiati et Marco Spinelli : Actuated cover door with emergency opening function for space telescopes. *In Proceedings of the 19th European Space Mechanisms and Tribology Symposium (ESMATS)*, 2021.

[39] Phytron GmbH : physpace™ stepper motor series for space applications: Standard and customised solutions, September 2019. Edition 2019.

[40] M. H. Lucy, R. D. Buehrle et J. P. Woolley : Comparison of separation shock for explosive and nonexplosive release actuators on a small spacecraft panel. Rapport technique NASA-TM-110257, NASA Langley Research Center, 1996. Accessed: 2025-05-22.

[41] Jason Priebe : *The utilization of High Output Paraffin actuators in aerospace applications*. 1995.

[42] Scott Tibbitts : High-output paraffin linear motors: utilization in adaptive systems. *In* Mark A. Ealey, éditeur : *Active and Adaptive Optical Components*, volume 1543, pages 388 – 399. International Society for Optics and Photonics, SPIE, 1992.

[43] M. F. Ashby : *Materials Selection in Mechanical Design*. Elsevier, Oxford, 4th édition, 2011.

[44] J. L. Meriam, L. G. Kraige et J. N. Bolton : *Engineering Mechanics: Dynamics*. John Wiley & Sons, Hoboken, NJ, 9th édition, 2018.

[45] Robert L. Norton : *Design of Machinery: An introduction to the synthesis and analysis of mechanisms and machines*. McGraw-Hill Education, 2020.

[46] MathWorks : *circcirc (MATLAB Mapping Toolbox)*. The MathWorks, Inc., 2024. `https://nl.mathworks.com/help/map/ref/circcirc.html`.

[47] MathWorks : *Global Optimization Toolbox Solver Characteristics*. The MathWorks, Inc., Natick, Massachusetts, United States, 2025. `https://nl.mathworks.com/help/gads/improving-optimization-by-choosing-another-solver.html`.

[48] The MathWorks, Inc. : *fmincon - Find minimum of constrained nonlinear multivariable function*. The MathWorks, Inc., Natick, MA, 2025. Accessed: May 6, 2025.

[49] Zsolt Ugray, Leon Lasdon, John Plummer, Fred Glover, James Kelly et Rafael Marti : Scatter search and local nlp solvers: A multistart framework for global optimization. *SSRN Electronic Journal*, 5 2006.

[50] Virginia Torczon et Siam J Optim : On the convergence of pattern search algorithms. *SIAM Journal on Optimization*, 7:1–25, 1997.

[51] The MathWorks, Inc. : *patternsearch - Find minimum of function using pattern search*. The MathWorks, Inc., Natick, MA, 2025. Accessed: May 6, 2025.

[52] The MathWorks, Inc. : *Table for Choosing a Solver*. The MathWorks, Inc., Natick, MA, 2025. Accessed: May 6, 2025.

[53] A. J. Booker, J. E. Dennis, P. D. Frank, D. B. Serafini, V. Torczon et M. W. Trosset : A rigorous framework for optimization of expensive functions by surrogates. *Structural Optimization*, 17:1–13, 1999.

[54] H. M. Gutmann : A radial basis function method for global optimization. *Journal of Global Optimization*, 19:201–227, 3 2001.

[55] The MathWorks, Inc. : *surrogateopt - Solve bound-constrained global optimization problems using surrogate optimization*. The MathWorks, Inc., Natick, MA, 2025. Accessed: May 6, 2025.

[56] Harald Niederreiter : *Random Number Generation and Quasi-Monte Carlo Methods*. Society for Industrial and Applied Mathematics, Philadelphia, Pennsylvania, 1992.

[57] Søren Asmussen et Peter W. Glynn : *Stochastic Simulation: Algorithms and Analysis*, volume 57 de *Stochastic Modelling and Applied Probability*. Springer, 2007.

[58] J. H. Halton : On the efficiency of certain quasi-random sequences of points in evaluating multi-dimensional integrals. *Numerische Mathematik*, 2:84–90, 1960.

[59] Paul Bratley et Bennett L. Fox : Algorithm 659: Implementing sobol's quasirandom sequence generator. *ACM Transactions on Mathematical Software*, 14(1):88–100, 1988.

[60] V. Arp et Al. : Thermal expansion of some engineering materials from 20 to 293 k. *Cryogenics*, 2(4):230–235, 1962.

[61] Barrie D. Dunn : Materials and processes. *Materials and Processes*, 2016.

[62] Robert C. Juvinall et Kurt M. Marshek : *Fundamentals of Machine Component Design, EMEA Edition*. John Wiley Sons Ltd, 7 édition, 2021.

[63] Brett Sanborn, Bo Song et Erik E. Nishida : Development of a new method to investigate the dynamic friction behavior of interfaces using a kolsky tension bar. *Experimental Mechanics*, 58(3):335–342, 2018. Published online 02 November 2017.

[64] Pfeiffer Vacuum GmbH : *Vacuum Technology Handbook*. Pfeiffer Vacuum GmbH, Asslar, Germany, 2020. Available online: `https://elmi-tec.com.br/data/novo_ctlg_pfeiffer_ingles.pdf`.